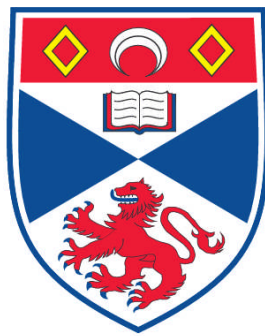


**THE INVESTIGATION OF QUASI-SEPARATRIX LAYERS IN  
SOLAR MAGNETIC FIELDS**

**Anna Lisa Restante**

**A Thesis Submitted for the Degree of PhD  
at the  
University of St. Andrews**



**2011**

**Full metadata for this item is available in  
Research@StAndrews:FullText  
at:**

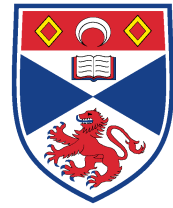
**<http://research-repository.st-andrews.ac.uk/>**

**Please use this identifier to cite or link to this item:**

**<http://hdl.handle.net/10023/2106>**

**This item is protected by original copyright**

**This item is licensed under a  
Creative Commons License**



University  
of  
St Andrews

# The Investigation of Quasi-Separatrix Layers in Solar Magnetic Fields

Anna Lisa Restante

Thesis submitted for the degree of Doctor of Philosophy of the  
University of St Andrews and the Observatoire de Paris

20th June 2011

# Declaration

I, Anna Lisa Restante, hereby certify that this thesis, which is approximately 32000 words in length, has been written by me, that it is the record of work carried out by me and that it has not been submitted in any previous application for a higher degree.

**Date:** 19/05/2011    **Signature of candidate:**

I was admitted as a research student in October 2007 and as a candidate for the degree of Doctor of Philosophy in October 2007; the higher study for which this is a record was carried out in the University of St Andrews between 2007 and 2010.

**Date:** 19/05/2011    **Signature of candidate:**

I hereby certify that the candidate has fulfilled the conditions of the Resolution and Regulations appropriate for the degree of Doctor of Philosophy in the University of St Andrews and that the candidate is qualified to submit this thesis in application for that degree.

**Date:** 19/05/2011    **Signature of supervisor:**

In submitting this thesis to the University of St Andrews I understand that I am giving permission for it to be made available for use in accordance with the regulations of the University Library for the time being in force, subject to any copyright vested in the work not being affected thereby. I also understand that the title and the abstract will be published, and that a copy of the work may be made and supplied to any bona fide library or research worker, that my thesis will be electronically accessible for personal or research use unless exempt by award of an embargo as requested below, and that the library has the right to migrate my thesis into new electronic forms as required to ensure continued access to the thesis. We have obtained any third-party copyright permissions that may be required in order to allow such access and migration, or have requested the appropriate embargo below.

**Date:** 19/05/2011    **Signature of candidate:**

The following is an agreed request by candidate and supervisor regarding the electronic publication of this thesis:

Access to Printed copy and electronic publication of thesis through the University of St Andrews.

**Date:** 19/05/2011    **Signature of candidate:**

**Signature of supervisor:**



## Acknowledgements/Remerciements

It is a pleasure to thank those who made this thesis possible. I would like to show my gratitude to my supervisors C. Parnell and G. Aulanier for their guidance and encouragement throughout this work, and E. Priest for his support especially during the bureaucratic process. This thesis would not have been possible without the financial support from SOLAIRE European Research Training Network.

During those years I have met a lot of people outside and inside the work sphere that contributed to make this adventure possible and enjoyable. I would like to thank my colleagues who have made me feel welcome in foreign countries and for our many fruitful conversations. To my old and new friends thanks you for being just the way you are and thank you to being even closer to me when there have been km between us.

And last but not least, I am grateful to my family. To my parents, my sister and my Matthieu for being there for me during my happy moments and especially during my difficult ones.

# Abstract

The structure of the magnetic field is often an important factor in many energetic processes in the solar corona. To determine the topology of the magnetic field features such as null points, separatrix surfaces, and separators must be found. It has been found that these features may be preferred sites for the formation of current sheets associated with the accumulation of free magnetic energy. Over the last decade, it also became clear that the geometrical analogs of the separatrices, the so-called quasi separatrix layers, have similar properties. This thesis has the aim of investigating these properties and to find correlations between these quantities. Our goal is to determine the relation between the geometrical features associated with the QSLs and with current structures, sites of reconnection and topological features.

With these aims we conduct three different studies. First, we investigate a non linear force free magnetic field extrapolation from observed magnetogram data taken during a solar flare eruption concentrating our attention on two snapshots, one before the event and one after. We determine the QSLs and related structures and by considering carefully how these change between the two snapshots we are able to propose a possible scenario for how the flare occurred. In our second project we consider potential source distributions. We take different potential point source models: two four sources models already presented in the literature and a random distribution of fifteen sources. From these potential models we conduct a detailed analysis of the relationship between topological features and QSLs. It is found that the maxima of the  $Q$ -factor in the photosphere are located near and above the position of the subphotospheric null points (extending part way along their spines) and that their narrow QSLs are associated with the curves defined by the photospheric endpoints of all fan field lines that start from subphotospheric sources. Our last study investigates two different flux rope emergence simulations. In particular, we take one case with and one without an overlying magnetic field. Here, we can identify the QSLs, current, and sites of reconnection and determine the relation between them. From this work we found that not all high- $Q$  regions are associated with current and/or reconnection and vice-versa. We also investigated the geometry of the field lines associated with high- $Q$  regions to determine which geometrical behaviour of the magnetic field they are associated with. Those that are associated with reconnection also coincide with topological features such as separators.

# Résumé

La structure du champ magnétique occupe une place importante dans de nombreux processus énergétiques de la couronne solaire. Pour déterminer la topologie du champ magnétique, il est nécessaire de calculer des éléments comme les points nuls, les séparatrices et les séparateurs. Il a été montré que ces régions peuvent être des sites privilégiés pour la formation de couches de courant associées à une accumulation d'énergie magnétique libre. Durant la dernière décennie, il est également apparu que les analogues géométriques des séparatrices, les quasi-séparatrices (QSLs), possédaient des propriétés similaires. Cette thèse a pour but d'étudier ces propriétés et d'établir des corrélations entre ces quantités. Notre objectif est de déterminer la relation entre les éléments géométriques associés aux QSLs et les structures de courant électrique, sites de reconnexion et éléments topologiques.

Dans ce contexte, nous avons mené trois études distinctes. Dans un premier temps, nous étudions le cas d'un champ magnétique extrapolé dans l'approximation du champ sans force non-linéaire à partir des données observationnelles d'un magnétogramme effectué lors d'un flare d'éruption solaire, en concentrant notre attention sur deux enregistrements avant et après l'événement. Nous déterminons les QSLs et les structures associées, et en analysant soigneusement leur changement d'un enregistrement à l'autre nous pouvons proposer un scénario possible de la création du flare. Dans notre second projet, nous nous intéressons aux distributions de sources de champ magnétique potentiel. Nous utilisons différents modèles de sources: deux modèles à quatre sources déjà répertoriés dans la littérature et une distribution aléatoire de quinze sources. À partir de ces modèles en champ potentiel nous réalisons une analyse détaillée de la relation entre les éléments topologiques et les QSLs. Nous montrons que les maxima du facteur d'élongation-écrasement  $Q$  dans la photosphère sont situés à proximité et au-dessus de la position des points nuls subphotosphériques, s'étendant partiellement le long des épines des points nuls, et que les QSLs fines sont associés aux courbes définies par les points d'ancrage photosphériques des lignes de champ de la surface séparatrice en éventail émanant des sources subphotosphériques. Notre dernière étude porte sur deux simulations MHD différentes d'émergence de tubes de flux torsadés. En particulier, nous prenons un cas avec et un autre sans champ magnétique coronal environant. Nous pouvons identifier les QSLs, les courants électriques et les sites de reconnexion et pouvons également déterminer la relation existant entre eux. Nous avons trouvé que les régions de  $Q$  élevé ne sont pas toutes associées à des courants et / ou de la reconnexion et réciproquement. Nous avons également étudié la géométrie des lignes de champ associées aux régions de  $Q$  élevé afin de déterminer avec quel comportement géométrique du champ magnétique elles sont associées. Celles qui sont associées à la reconnexion coïncident également avec les éléments topologiques comme les séparateurs.

# Contents

<b>1</b>	<b>Introduction</b>	<b>1</b>
1.1	The structure of the Sun . . . . .	1
1.2	Solar phenomena . . . . .	9
1.3	Magnetohydrodynamics . . . . .	15
1.3.1	Fundamental equations . . . . .	15
1.3.2	Induction equation . . . . .	17
1.3.3	Magnetic field lines . . . . .	18
1.3.4	Magnetic topology . . . . .	19
1.4	Reconnection . . . . .	21
1.4.1	Magnetic annihilation . . . . .	22
1.4.2	Sweet-Parker mechanism . . . . .	24
1.4.3	Petschek's model . . . . .	25
1.4.4	Reconnection in 3D . . . . .	26
1.4.5	Quasi-separator reconnection . . . . .	30
<b>2</b>	<b>Investigation of QSLs in a solar flare</b>	<b>34</b>
2.1	Coronal magnetic field approximations . . . . .	34
2.2	Magnetic field extrapolation . . . . .	36
2.3	12-13 December 2006 event . . . . .	42
<b>3</b>	<b>Comparison of the magnetic skeleton and QSLs in source models</b>	<b>53</b>
3.1	Source models . . . . .	54
3.2	Models involving four sources . . . . .	56
3.2.1	Studied configurations . . . . .	56
3.2.2	Fan and spine separatrices emanating from the sources . . . . .	59
3.2.3	Relation between spines and QSL footprints . . . . .	60
3.3	Multi sources . . . . .	64
3.3.1	Strong spine-related QSLs in complex configurations . . . . .	64
3.3.2	Identification of non-spine related QSLs . . . . .	66
3.3.3	The role of fan field lines . . . . .	68
3.3.4	Comparison with the 4 source models and interpretation . . . . .	70

3.3.5	Connections between branches and null-halos . . . . .	73
3.4	Conclusion . . . . .	74
<b>4</b>	<b>Investigation of QSLs in 3D MHD simulations of an emerging twisted flux tube</b>	<b>77</b>
4.1	Non-magnetised coronal atmosphere . . . . .	79
4.1.1	Model . . . . .	79
4.1.2	Comparison between current and $Q$ -factor . . . . .	83
4.2	Magnetised coronal atmosphere . . . . .	92
4.2.1	Vertical cut . . . . .	106
<b>5</b>	<b>Conclusion</b>	<b>119</b>
5.1	Future work . . . . .	121
	<b>Bibliography</b>	<b>123</b>

# Chapter 1

## Introduction

Since Galileo burnt his eyes observing the Sun, our star, it has stopped being perfect. The year was, 1612 and Galileo had just pointed his new version of the Dutch tool called a “telescope” towards the sky. He found that our star was not the perfect smooth sphere that it was supposed to be, but instead it was active and full of “imperfections” that we are still trying to understand.

The Sun is not a special star: it is classified as a star of average size, temperature, age ( $\sim 4.6$  billion years old), and brightness. It is just one of about  $10^{11}$  stars in our own galaxy, the Milky Way, and there are probably at least  $10^{11}$  galaxies in the Universe. However it is the star at the centre of our solar system, and its vicinity (149.60 million km) gives the Sun the unique position of being the most studied star on the Earth. Despite that we still do not know all the characteristics of the Sun.

### 1.1 The structure of the Sun

The Sun is a nearly perfect sphere and, like all the other stars, is a massive shining sphere of hot gas composed essentially of Hydrogen (90%) and Helium ( $\lesssim 10\%$ ). The gas on the Sun is ionised, in other words, the Sun is formed of plasma. It has a diameter of 1.4 million kilometers, about 109 times the diameter of Earth, but this is a slightly misleading statement because the Sun has no true “surface”. There is nothing hard, or definite, about the solar disk that we see. The matter that makes up the apparent surface is so rarefied that we would consider it to be almost a vacuum here on Earth (the density of the photosphere, which we refer to as the solar surface, is around 1% of the Earth atmosphere). Through the solar atmosphere the density drops exponentially with increasing distance from the Sun’s centre (Zirker, 2002). Nevertheless, it has a well-defined interior structure (Figure 1.1), described below. The Sun’s radius is measured from its centre to the edge of the photosphere. This is simply the layer above which the gases are too cool or too thin to radiate a

significant amount of light, and is therefore the surface that is visible to the naked eye.

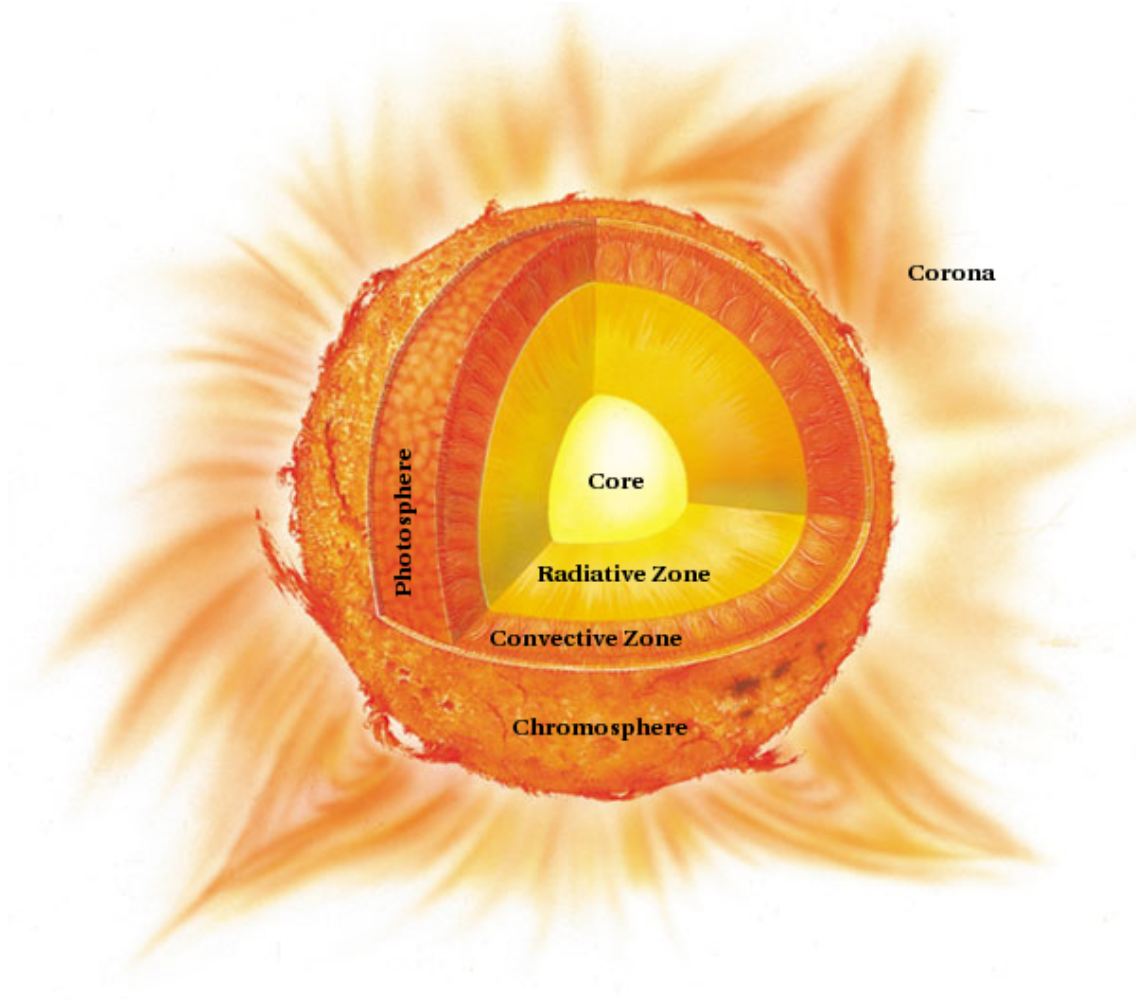


Figure 1.1: Structure of the Sun. (Figure adapted from [www.oup.co.uk](http://www.oup.co.uk))

### **The solar interior**

The solar interior is not directly observable, and the Sun itself is opaque to electromagnetic radiation. However to measure, visualise and study the star's interior we can combine theoretical models with helioseismology, which uses pressure waves (infrasound) traversing the Sun's inner structure to determine characteristics about the solar interior. Using these studies we can divide the solar interior into three main regions.

**The core** has a tremendously high temperature, pressure and density. It incorporates about 2% of the Sun’s volume, but contains almost half the Sun’s mass. Its maximum temperature is over 15 million Kelvin, its pressure is around  $10^{16} \text{ N m}^{-2}$  (Asimov, 1977) and it has a density of the order of  $1.6 \times 10^5 \text{ kg m}^{-3}$  (i.e.  $10^{32} \text{ particles m}^{-3}$ ). At these conditions, nuclear fusion readily occurs, turning four hydrogen nuclei into a single helium nucleus plus a lot of energy. This “hydrogen burning” releases gamma rays (high-energy photons) and neutrinos (particles with no charge and almost no mass). The fusion of helium to form other heavier elements and the fusion of these, also produce energy, but the high quantity of hydrogen makes this extra contribution of energy negligible. The photons emitted from the core have short wavelength, and are called high-energy gamma rays. These photons follow a long, torturous route as they work their way to the surface of the Sun colliding with electrons to form longer wavelength and less energetic X-ray photons.

**The radiative zone** is the next layer out from the core and it extends from  $0.2 R_{\odot}$  up to  $0.7 R_{\odot}$ . The temperature ranges from 15 million K to one million K. It can take gamma ray photons from the core millions of years to pass through the radiative zone. Deep in the radiative zone, the photons collide with plasma particles and change direction in random ways (Figure 1.6). Each photon may travel only a few millimetres before it suffers another collision and is sent off in a different direction. Nevertheless, the photons continue to work their way toward the surface with a zig-zag path toward regions of lower temperature and pressure.

**The convective zone (or convection zone)** forms the outer shell of the solar interior. It extends up to the solar surface ( $1 R_{\odot}$ ). The convective zone makes up about 66% of the Sun’s volume but it contains only slightly more than 2% of its mass. At the top of this zone, the density is only  $0.02 \text{ kg m}^{-3}$ , and the temperature is about 6000 K. The atoms in this layer of the Sun have some electrons because the temperature is not hot enough to strip them all away like they are in the core. Atoms with electrons are able to absorb and emit radiation, making this region opaque, like a thick fog. These atoms effectively block the outward flow of radiative energy and the energy absorbed by the atoms makes them enormously hot. At that point the convection currents take over and carry the Sun’s energy to the photosphere on seething rivers of hot gases. Although it may have taken the photons a million years to reach the convection zone, the energy they deliver rises through the entire convection zone in about three months. All the energy emitted at the surface of the Sun is transported there by convection ([solarsystem.nasa.gov](http://solarsystem.nasa.gov)). Thermal columns carry plasma to the surface (photosphere) of the Sun. As soon as the hot

material that has risen cools off at the surface, it plunges back downwards to the base of the convective zone, where it is reheated again from the radiative zone below. Convective overshoots are thought to occur at the base of the convective zone, moving turbulent down flows into the outer layers of the radiative zone enhancing the heating at the base.

The thermal columns in the convection zone are evident on the surface of the Sun, in the form of the solar granulation and supergranulation (Figure 1.2, Section 1.2).

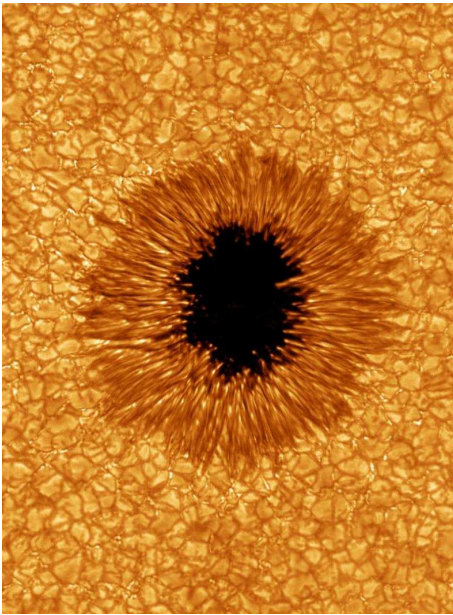


Figure 1.2: Sunspot 1084 with a resolution of 65 km. This is a photograph of a sunspot and solar granulation on the visible surface (photosphere) of the Sun. It is the first photograph from the Californian Big Bear Solar Observatory (BBSO) made on July 2010. The Sunspot is a less hot region on the surface of the Sun, about 3000 K compared to nearly 6000 K in the rest of the photosphere. This difference of temperature modified our perception, thus what is hotter is also brighter.

## Solar atmosphere

The visible solar atmosphere consists of three regions: the photosphere; the chromosphere; and the solar corona. Most of the visible (white) light comes from the photosphere: this is the part of the Sun we actually see. The chromosphere and corona also emit white light which can be seen when the light from the photosphere is blocked out, as occurs during a solar eclipse.

Like the solar interior, the solar atmosphere is so hot that the gas is primarily in a plasma state: electrons are no longer bound to atomic nuclei, and the gas is made up of charged particles (mostly protons and electrons). In this charged state, the solar atmosphere is greatly influenced by the strong solar magnetic fields that thread through it. These magnetic fields, and the outer solar atmosphere (the corona), extend out into interplanetary space as part of the solar wind.

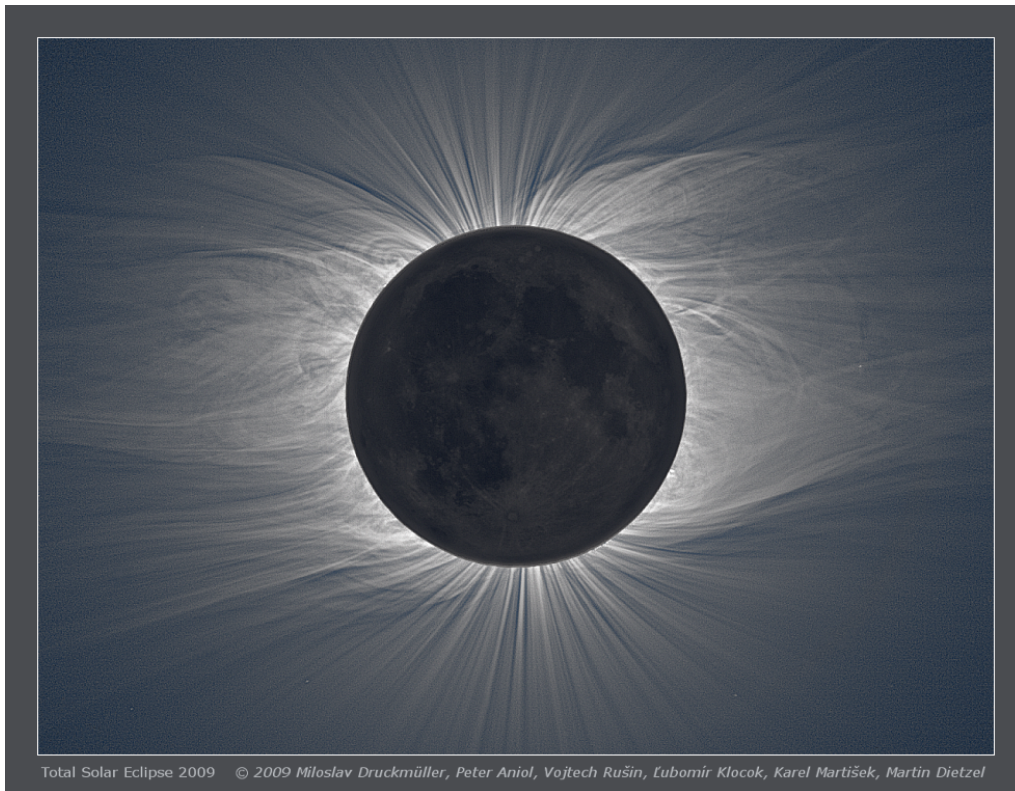


Figure 1.3: Total solar eclipse of July 22, 2009 on Enewetak Atoll in Marshall Islands (Picture from [www.zam.fme.vutbr.cz](http://www.zam.fme.vutbr.cz)).

**The photosphere**, literally “sphere of light”. This, the visible surface of the Sun, is the layer below which the Sun becomes opaque to visible light. Above the photosphere visible sunlight is free to propagate into space, and its energy escapes the Sun entirely. At the bottom of the photosphere, the temperature is about 6400 K, while it is around 4400 K at the top. The average density of the photosphere is less than  $10^{-3} \text{ kg m}^{-3}$  (about 0.1% of the density of air at sea level on earth). This may seem to be an extremely low density, but there are around  $10^{23}$  particles  $\text{m}^{-3}$ . Decreasing density contributes to the transparency. The Sun’s atmosphere changes from being opaque to being transparent over a distance of only a few hundred kilometers. This is remarkable given the size of the Sun, and represents such a rapid change that we often think of it as a true boundary.

The photosphere is formed of an inhomogeneous cellular brightness pattern discovered by Herschel (1801), which are the tops of granulation cells and few dark spots (sunspots, Figure 1.2).

**The chromosphere** (meaning “colour sphere”) is visible during solar eclipses (when the moon blocks the photosphere, Figure 1.3). The chromosphere is about 2500 km thick. The density of the gases decreases over almost seven orders of magnitude as one moves away from its boundary with the photosphere, from a high of  $2.0 \times 10^{-4} \text{ kg m}^{-3}$  to a low of  $1.0 \times 10^{-11} \text{ kg m}^{-3}$  where it merges into the solar transition region ([alienworlds.glam.ac.uk](http://alienworlds.glam.ac.uk)). These gases are transparent to most visible radiation, because hydrogen atoms are in an excited state and emit radiation near the red part of the visible spectrum. This reddish layer is a region of rising temperatures. From the bottom to the top of the chromosphere, the average temperature goes from 4400 K to about 10000 K and in some places even 20000 K. This rise was not anticipated by scientists when they first measured it since they expected the temperature to continue dropping off as it has until now as you move further away from the core.

**The transition region** is a relatively thin and very irregular layer of the Sun’s atmosphere that separates the hot corona from the much cooler chromosphere. It is visible from space using telescopes that can sense ultraviolet. It is important because it is the site of several unrelated but important transitions in the physics of the solar atmosphere. While the chromosphere and corona have a relatively continuous structure, the transition region appears to be a discontinuity in the temperature-density structure of the outer solar atmosphere. Considered in terms of an average spherically symmetric model, the temperature jumps from the order of  $2.5 \times 10^4 \text{ K}$  to  $10^6 \text{ K}$  in only a few thousand kilometers (Mariska, 1986). This height change is so small relative to a gravitational scale height that the pressure remains roughly constant, which

implies a density decrease of a factor of 40 over the same height range.

**The corona** is the outer layer of the Sun’s atmosphere. The corona extends for millions of kilometres but, usually, we cannot see it because of the brightness of the photosphere. However, during a total solar eclipse (Figure 1.3), one can see the corona shining against the dark sky. The corona consists of such structures as loops and streams of ionised gas. The structures evolve outward from the solar surface, and magnetic fields that emerge from inside the Sun shape them.

The corona is very hot. In the part of the corona nearest to the solar surface, the temperature is about 1 million to 6 million Kelvin, and the number density is about  $10^{11}$  to  $10^{12}$  particles  $\text{m}^{-3}$ . The temperature reaches tens of millions of degrees when a flare occurs. Such high temperatures mean that the bulk of the radiation from the corona is emitted at ultraviolet and X-ray wavelengths. Magnetic fields on the Sun seem to play an important part in heating the gas to such a high temperature. However, the exact way that this happens is not well understood.

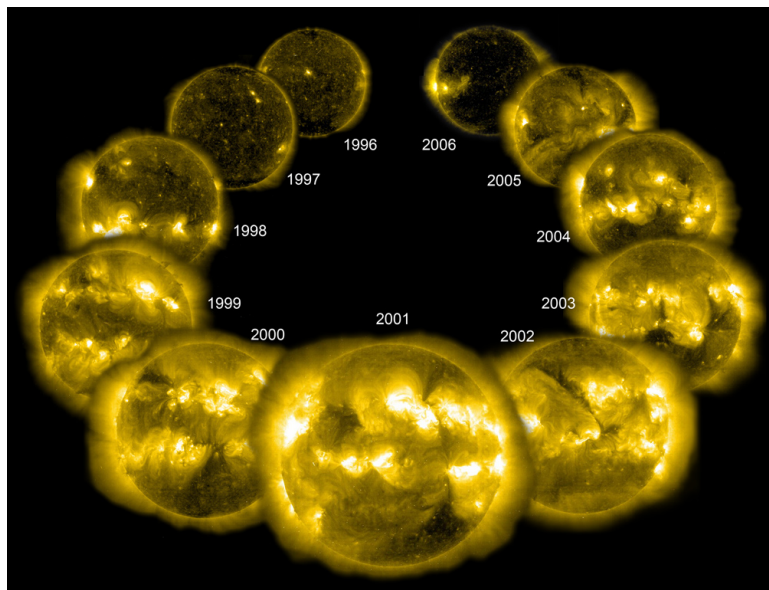


Figure 1.4: This is a composite picture showing how the corona varies during the Sun’s solar cycle (which takes 11 years). The images of the corona are taken by the SOHO satellite which is currently orbiting the Sun.

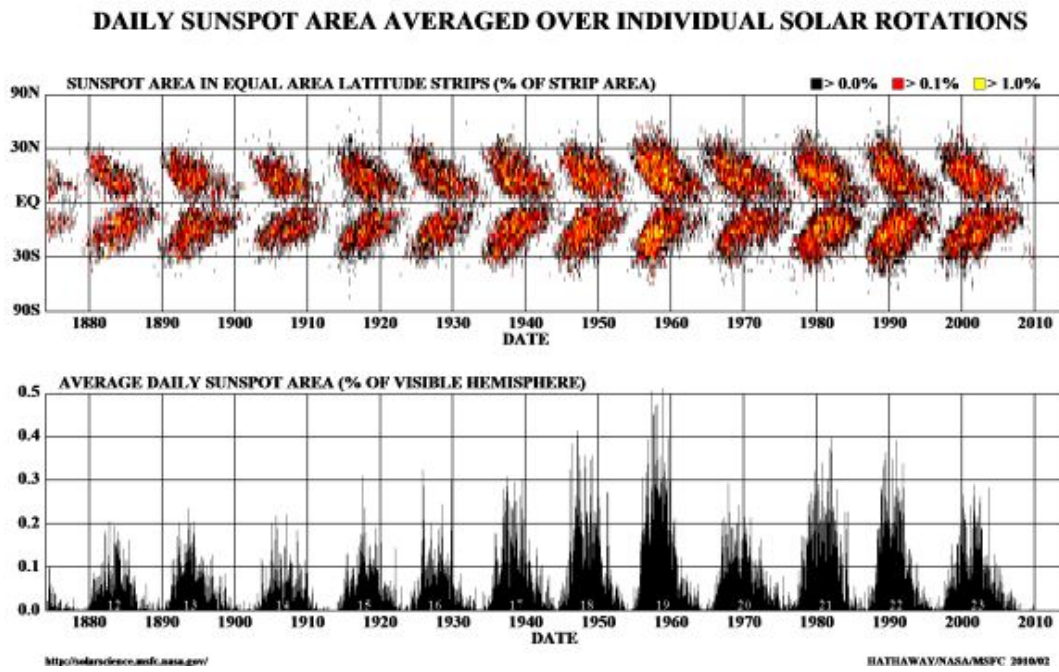


Figure 1.5: (a) The progression of sunspots from high latitudes to the equator over the solar cycle produces the famous butterfly diagram (b) This figure summarises sunspot number observations since 1874. Figure from [solarscience.msfc.nasa.gov](http://solarscience.msfc.nasa.gov/).

## 1.2 Solar phenomena

So far we have mentioned sunspots, but there are many other phenomena that occur on the Sun. Here, we discuss these in more detail. Solar events are not the same in intensity, duration and number over time (Figure 1.5), instead in many cases their behaviour is correlated to the number of sunspots which follows an 11 years cycle discovered by Schwabe (1843) (he started his observations in 1826).

The solar cycle oscillates between solar maximum when many solar phenomena are at their most active and solar minimum when these events are less frequent. In the Figure 1.4, we can see example images of the corona during a recent solar cycle between 1996 and 2007. There is a lot of activity in the picture taken in 2001 (solar maximum) whereas in the pictures taken in 1996 and 2006 the Sun looks dormant (solar minima). These phenomena involve and occur throughout different layers of the Sun (Figure 1.6).

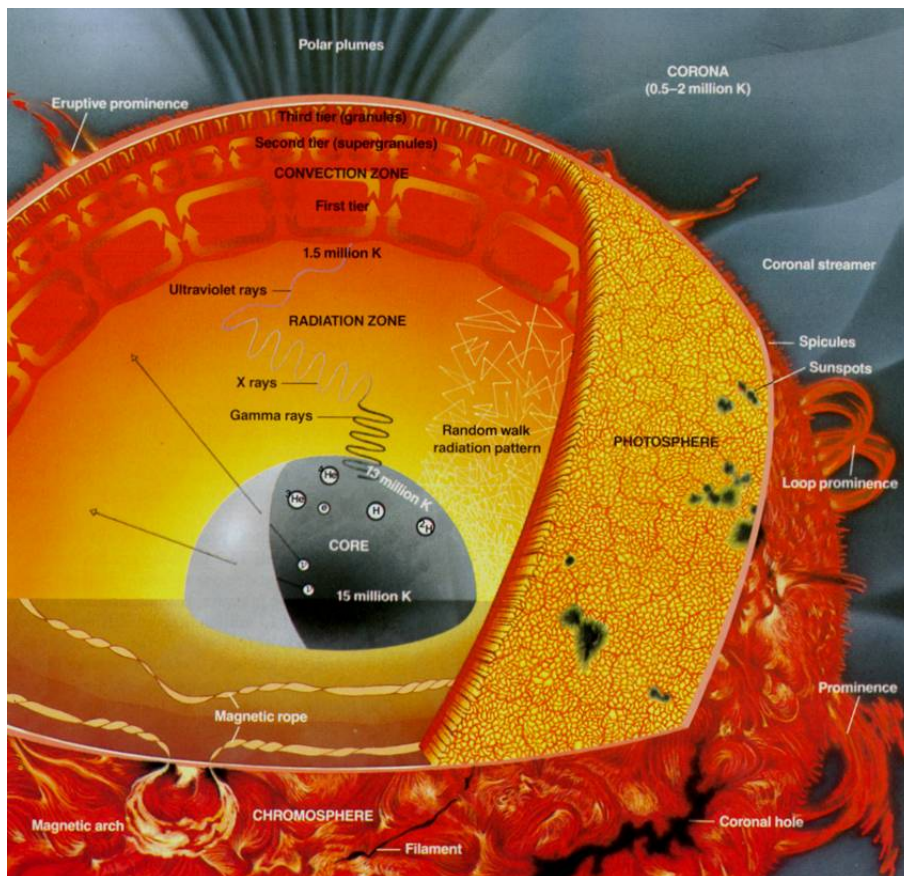


Figure 1.6: Overview of the Sun showing many different phenomena occurring in the different regions of the Sun. Figure from Dhillon (2009).

**Sunspots** are the easiest feature to detect on the solar photosphere. In fact, some sunspot groups grow so large that they are visible with the naked eye (suitably protected of course) from Earth. The earliest surviving record of sunspot observation dates from 364 BC, based on comments by Chinese astronomer Gan De in a star catalogue (Rogers, 2007). As far as we know, the first reasonably accurate description of sunspots was published by Galileo in 1613, who realised that sunspots were part of the surface of the Sun. However, the first physical explanation was given by Hale (1908), who found that sunspots are locations of extremely strong magnetic field. They are apparent as dark spots, with a central dark umbra and a lighter surrounding penumbra, both of which are silhouetted against the brighter photosphere. They occur due to high concentrations of magnetic field (up to several thousand Gauss) which inhibit heat flow to the surface from the convective zone below. In reality sunspots are not dark at all. The minimum temperature in the largest umbra is around 4200 K. A very small sunspot without any penumbra is called a pore.

The number of sunspots on the Sun’s surface rises and falls between a maximum and a minimum over an 11-year cycle (Figure 1.5). The idea of computing sunspot numbers was originated by Rudolf Wolf in 1849 in Zurich, Switzerland and, thus, the procedure he initiated bears his name (or place). At solar maximum there may be as many as 200 spots on the Sun’s surface whereas at solar minimum there may be almost zero. The next sunspot maximum is predicted to take place in 2017.

At the start of the sunspot cycle, a few spots are visible at high latitudes. As the cycle progresses, the numbers increase and the latitude at which new spot emerge drift towards the equator. When the latitudes of new sunspots are plotted against time, the classic “butterfly” diagram (Figure 1.5 a) of the solar cycle is seen. A new cycle starts when sunspots begin to appear at high latitudes once more.

**Faculae** are bright areas that are only seen near the limb where the apparent photospheric intensity decreases due to “limb darkening”. Faculae have been known about since telescopes were first pointed at the Sun, but their origin has never been clearly revealed. Scientist thought that they were due to strong magnetic fields (Hale, 1922). Thanks to simulations, based on recent high-resolution images that show these brightening in unprecedented detail, Keller et al. (2004) has shown that faculae originate from a thin layer within granules just below largely transparent magnetic flux concentrations.

**Granules**, as already mentioned, are “small” cells covering the entire photosphere. This is the convective activity of the Sun expressed at the surface. The bright cells or granules are on average about 1100 km across and they are separated

from each other by dark lanes which are about 200 km wide (Kennewell and McDonald, 2010). Individual granules are only short lived. Their average lifetime is around 10 minutes, with a range from about 8 to 15 minutes. Granules are the tops of convection cells where hot fluid (gas and plasma) rises up from the interior convective zone. This material spreads out across the surface, cools, and then sinks downward along the dark lanes.

Solar granules cover the entire photospheric surface, except where there are sunspots. In sunspot regions convection is inhibited thus there are no visible granules (convection cells). There are approximately 4 million granules that cover the solar surface at any one time.

**Supergranulation** is a much larger version of granulation, where large groups of granules seem to move together. The supergranular velocity field was discovered by Hart (1954, 1956). The supergranulation cell is defined by its horizontal flow pattern with a typical velocity of  $500 \text{ m s}^{-1}$  (Kueveler, 1983). The fluid motions from both granules and supergranules can carry magnetic field bundles which thread through the photosphere.

**Filaments and Prominences** Filaments are dark, thread-like features seen in H-alpha on the disk of the Sun. These are dense clouds of material that are somewhat cooler ( $T \simeq 8000\text{K}$ ) than the surrounding chromosphere. Prominence are dense clouds of material suspended above the surface of the Sun by loops of magnetic field. They are observed in the red light of hydrogen projecting out above the limb, or edge, of the Sun. Prominences and filaments are actually the same things just viewed from different angles. Prominences can remain in a quiet or quiescent state for days or weeks. However, as the magnetic loops that support them slowly change, prominences can erupt and rise off of the Sun over the course of a few minutes or hours. They were first observed in the two 1970 rocket flights (Giacconi, 1922) which also detected coronal holes.

**Spicules** are small jet-like eruptions seen throughout the chromospheric network. They appear as short dark streaks in H-alpha images. They last about a few minutes, but in the process eject material off from the surface and outward into the hot corona at speeds of 20 to  $30 \text{ km s}^{-1}$  (solarscience.msfc.nasa.gov).

**Solar flares** are tremendous explosions in the atmosphere of the Sun. In a matter of just a few minutes they heat material to many millions of degrees and release an equivalent of a billion hydrogen bombs worth of energy. Most solar flares occur in or around sunspots, usually along the dividing line (neutral line) between areas of oppositely directed magnetic fields. The key to understanding and predicting solar flares is the structure of the magnetic field around sunspots.

If this structure becomes twisted and sheared then the magnetic field becomes stressed storing increased amounts of energy which may be released explosively.

During the occurrence of a solar flare, plasma is heated to tens of millions Kelvin, while electrons, protons and heavier ions can sometimes be accelerated to near the speed of light. The largest flares are known as X-class flares and the significant amount of energy commonly associated with solar flares can take many days to build up, but only a few minutes to release. Flares involve the conversion of magnetic energy into many forms: electro-magnetic (Gamma rays and X-rays), energetic particles (protons and electrons), and mass flows and thermal energy. Flares are characterised by their brightness in soft X-rays (X-Ray flux).

Solar flares were first recorded in 1859. Their activity can vary from several per day to only a few a month, depending mostly upon the overall activity of the Sun as a whole. They cannot typically be detected by the naked eye from the surface of the earth. Solar flares produce electromagnetic radiation across the electromagnetic spectrum at all wavelengths from long-wave radio to the shortest wavelength gamma rays and are often observed using filters to isolate the light emitted by hydrogen atoms in the red region of the solar spectrum (the H-alpha spectral line).

Despite the huge variety of parameters there are some criteria, which made it possible to divide the flares into two morphological classes (Vrnak et al., 2007).

1. Dynamical (eruptive, two-ribbon)

This type of flare is related to CMEs. In eruptive events magnetic field lines are opened by CMEs and reconnect on a time scale of hours which provides a prolonged energy release, characteristic for this type of flares. But it must be mentioned that CMEs can also be accompanied by short duration flares. After the flare event there is a completely new magnetic structure.

2. Confined

Flares of this type, are confined in a finite coronal volume. While in the first case we have a massive restructuring of the magnetic field lines, in this case the global magnetic structure remains the same. Simple loop flares belong to this group (Khan et al., 2004).

**Coronal Mass Ejections (or CMEs)** are huge eruptions of material from the Sun's corona into interplanetary space over the course of several hours. Most of the ejected material comes from the low corona, although cooler, denser

material, probably of chromospheric origin, can also be ejected (Webb, 2000). CMEs are energetic solar explosions and result in the ejection of up to 100 billion kilograms of multi-million-degree plasma at speeds ranging from 10 to 2,000 km s<sup>-1</sup>. They often look like bubbles and, when seen close to the Sun, can appear bigger than the Sun itself (Figure 1.7), though their density is extremely low.

CMEs originate in regions where the magnetic field is closed and they result from the catastrophic disruption of large-scale coronal magnetic structures, such as coronal streamers. CMEs can occur at any time during the solar cycle, but increase in frequency from about 0.5 per day during minimum years to about 2.5 per day around solar maximum. Fast CMEs, those which outpace the ambient solar wind, give rise to large geomagnetic storms when they encounter the Earth's magnetosphere. Such storms, which can disrupt power grids, damage satellite systems, and threaten the safety of astronauts, can result from the passage either of the CME itself or of the shock created by the fast CME's interaction with the slower-moving solar wind.

Although the Sun's corona has been observed during total eclipses of the Sun for thousands of years, the existence of coronal mass ejections was unrecognised until the space age when telescopes in which the Sun is artificially eclipsed revealed the extended corona. During a natural eclipse of the Sun the corona is only visible for a few minutes at most, too short a period of time to notice any changes in coronal features, however, with new measurements the corona can be observed for hours and days.

**Coronal loops** are associated with the closed magnetic field lines that connect magnetic regions on the solar surface. The two ends of a loop, known as footpoints, lie in regions of the photosphere of opposite magnetic polarity to each other. Coronal loops populate both active and quiet regions of the solar atmosphere. Large faint ones, last days or weeks, are more typical of the quiet corona, when solar activity is low. The majority of solar loops are found around sunspots and in active regions and are common around the time of solar maximum. Some of these loops, however, are associated with solar flares and are visible for much shorter periods. These loops contain denser material than their surroundings.

**Helmet streamers** are large cap-like coronal structures with long pointed peaks that usually overly sunspots and active regions. Prominences are often found lying at the base of these structures. Helmet streamers are formed by a network of magnetic loops that connect the sunspots in active regions and help suspend the prominence material above the solar surface. The closed magnetic field lines trap the electrically charged coronal gases to form these relatively dense

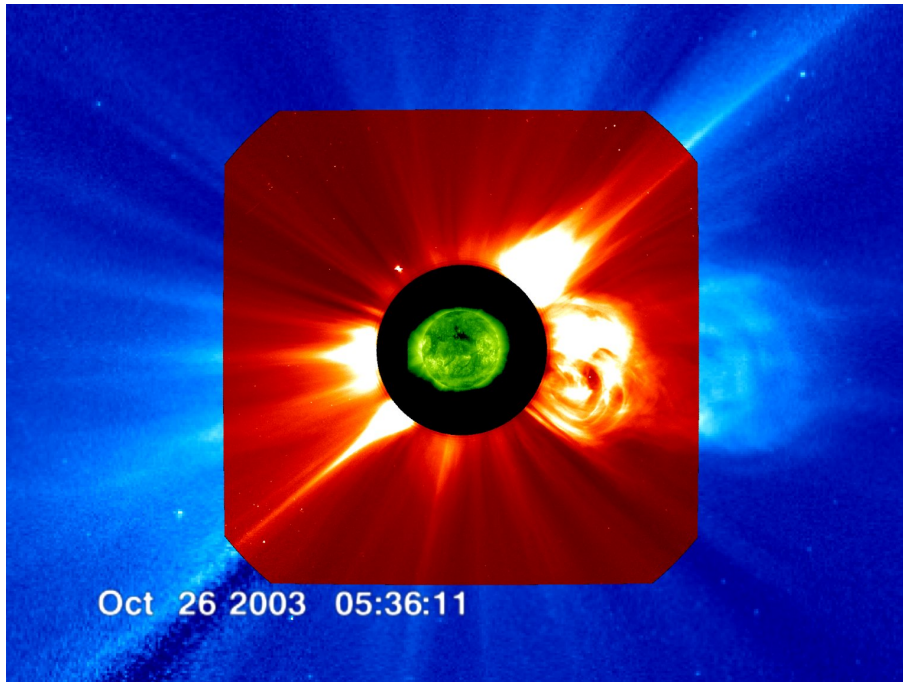


Figure 1.7: This picture is a combination of SOHO/EIT at 195 Angstroms as well as the LASCO/C2 and C3 cameras taken on Halloween 2003. At this scale we can see the flashes from solar flares in SOHO/EIT (green) and the subsequent coronal mass ejections in SOHO/LASCO/C2 (red) and SOHO/LASCO/C3 (blue). Figure from [www.nasaimages.org](http://www.nasaimages.org).

structures. The pointed peaks are formed by the action of the solar wind blowing away from the Sun in the spaces between the streamers.

**Polar plumes** are long thin streamers that project outwards from the Sun's north and south poles. Bright areas generally occur at the footpoints of these features that are associated with small magnetic regions on the solar surface. These structures are associated with the “open” magnetic field lines at the Sun's poles. The plumes are formed by the action of the solar wind in much the same way as the peaks on the helmet streamers.

**Coronal holes** are regions where the corona is dark. Coronal holes are associated with “open” magnetic field lines and are often found at the Sun's poles. The high-speed solar wind is known to originate in coronal holes.

**Solar wind** is a continuous outflow of plasma from Sun. The first theoretical treatment for a continuously blowing solar wind was given by Parker (1958), who extended the theoretical work of Chapman and Zirin (1957). They showed

that the solar corona is extending out into interplanetary space and Parker presented isothermal solutions that demonstrated that there must be a solar wind since the corona cannot be in static equilibrium and must be continuously expanding outwards.

The solar wind can roughly be divided into a slow wind and a fast wind. The slow wind comes from streamer belts, areas of closed magnetic field lines in the Sun, and has speeds of around  $250 - 400 \text{ km s}^{-1}$ , and has a density of around  $11 \times 10^6 \text{ m}^{-3}$  at  $1 \text{ AU} \simeq 1.5 \times 10^8 \text{ km}$ . The high speed solar wind flows from coronal holes at around  $400 - 800 \text{ km s}^{-1}$  (Cranmer, 2002) and has a density of around  $3 \times 10^6 \text{ m}^{-3}$  at  $1 \text{ AU} \simeq 1.5 \times 10^8 \text{ km}$ . While the large polar coronal holes disappear during the ascending phase of the solar cycle, smaller and shorter lived coronal holes can appear during solar maximum at all latitudes, including equatorial regions. However, only a few of these coronal holes are sufficiently large or persistent to significantly affect the solar wind properties. Therefore the solar wind during the maximum times is generally dominated by the slow solar wind which is emitted from the many streamer belts that may exist all over the solar surface during solar maximum.

In this thesis, we focus on the structure of the low solar corona, as determined by the strong magnetic force which is the principal force at play there. To model the magnetic field and the plasma on the large scales of interest here requires the use of the equations of magnetohydrodynamics, which are presented in the following section.

## 1.3 Magnetohydrodynamics

### 1.3.1 Fundamental equations

As already discussed, the solar atmosphere is composed of plasma. On large length scales, large enough to safely ignore the effect of individual particles, a plasma may be considered as a non-relativistic single fluid in thermodynamic equilibrium with charge-neutrality and we can use the equations of magnetohydrodynamics to describe its physical behaviour. Magnetohydrodynamics (MHD) combines elements from fluid dynamics and electromagnetism to describe the motion of a magnetic fluid. The basic equations of MHD in international units are given below (Priest, 1982, Priest and Forbes, 2000).

Conservation of mass:

$$\frac{\partial \rho}{\partial t} + \nabla \cdot (\rho \mathbf{v}) = 0 \tag{1.1}$$

Equation of motion:

$$\rho \frac{D\mathbf{v}}{Dt} = -\nabla p + \mathbf{j} \times \mathbf{B} + \rho \mathbf{g} + \underbrace{\rho \nu (\nabla^2 \mathbf{v} + \frac{1}{3} \nabla (\nabla \cdot \mathbf{v}))}_{\text{viscous term}} \quad (1.2)$$

Energy equation:

$$\frac{\rho^\gamma}{\gamma - 1} \frac{D}{Dt} \left( \frac{p}{\rho^\gamma} \right) = -\mathcal{L} \quad (1.3)$$

Ideal gas law:

$$p = \frac{R}{\hat{\mu}} \rho T \quad (1.4)$$

Solenoidal condition:

$$\nabla \cdot \mathbf{B} = 0 \quad (1.5)$$

Faraday's law:

$$\frac{\partial \mathbf{B}}{\partial t} = -\nabla \times \mathbf{E} \quad (1.6)$$

Ampère's law:

$$\nabla \times \mathbf{B} = \mu \mathbf{j} \quad (1.7)$$

Ohm's law:

$$\mathbf{E} + \mathbf{v} \times \mathbf{B} = \frac{\mathbf{j}}{\sigma} \quad (1.8)$$

Here,  $\rho$  is density,  $t$  is time,  $\mathbf{v}$  is fluid velocity,  $p$  is pressure,  $\mathbf{j}$  is electric current density,  $\mathbf{B}$  is magnetic induction (usually referred to as magnetic field),  $T$  is temperature,  $\sigma$  is the electrical conductivity and  $\mathbf{E}$  is electric field. In the Equation of motion 1.2,  $\mathbf{g}$  is gravitational acceleration,  $\nu$  is the coefficient of kinematic viscosity that is usually calculated with the formula from Spitzer (1962). Equation 1.2 is an approximation to the correct and much more complex expression given by Braginskii (1965) that includes other terms like the thermal force. In the Energy equation 1.3,  $\gamma$  is the ratio of specific heats (usually  $\gamma = \frac{5}{3}$  for an ideal monoatomic gas) and  $\mathcal{L}$  is the energy loss function (Priest, 1982)

$$\mathcal{L} = \nabla \cdot \mathbf{q} + L_r - \frac{j^2}{\sigma} - H,$$

where  $\mathbf{q}$  is the heat flux due to particle conduction;  $L_r$  is the net radiation;  $\frac{j^2}{\sigma}$  is the ohmic dissipation and  $H$  represents the sum of all other heating sources like the nuclear energy generation in the interior, viscous dissipation and others. In the ideal gas law (Equation 1.4)  $R$  is the universal gas constant ( $R = 8.314510 \text{ JK}^{-1} \text{ mol}^{-1}$ ),  $\hat{\mu}$

is the mean atomic weight (average mass per particle in units of mass of a proton) and in the Ampère’s law (Equation 1.7)  $\mu$  is the magnetic permeability ( $4\pi \times 10^{-7} \text{Hm}^{-1}$ ).

In the solar corona all of conditions mentioned before are generally valid, over large enough length-scales. Hereafter we are going to make more assumptions, since in this thesis we are specifically interested in a physical description of the corona. First of all we are going to consider a fully ionised quasi-neutral plasma (ions and electrons are equally distributed so that  $\hat{\mu} = 0.5$ ) second an inviscid plasma so we can ignore viscous forces in the equation of motion (Equation 1.2).

Under these conditions we can simplify the Equation 1.2 and Equation 1.4 and summarise them as follows.

Equation of motion:

$$\rho \left( \frac{\partial \mathbf{v}}{\partial t} + (\mathbf{v} \cdot \nabla) \mathbf{v} \right) = -\nabla p + \mathbf{j} \times \mathbf{B} + \rho \mathbf{g} \quad (1.9)$$

Ideal gas law:

$$p = 2\rho RT \quad (1.10)$$

### 1.3.2 Induction equation

In solar MHD, we generally work with the primary variables,  $\mathbf{B}$  and  $\mathbf{v}$  eliminating the electric field,  $\mathbf{E}$  and the electric current density,  $\mathbf{j}$ . To eliminate  $\mathbf{E}$ , we combine Ohm’s law (Equation 1.8) and the Ampère law (Equation 1.7) to get

$$\mathbf{E} = -\mathbf{v} \times \mathbf{B} + \frac{1}{\mu\sigma} \nabla \times \mathbf{B}. \quad (1.11)$$

If we then substitute Equation 1.11 into Faraday’s law (Equation 1.6) this becomes

$$\frac{\partial \mathbf{B}}{\partial t} = \nabla \times (\mathbf{v} \times \mathbf{B}) - \nabla \times (\eta \nabla \times \mathbf{B}), \quad (1.12)$$

where the diffusivity,

$$\eta = \frac{1}{\mu\sigma}. \quad (1.13)$$

Assuming  $\eta$  is constant and using the solenoidal condition (Equation 1.5) we get the *induction equation*:

$$\frac{\partial \mathbf{B}}{\partial t} = \nabla \times (\mathbf{v} \times \mathbf{B}) + \eta \nabla^2 \mathbf{B}. \quad (1.14)$$

### Magnetic Reynolds number (and the Lundquist number)

From the induction equation (Equation 1.14) we define an important dimensionless parameter,  $R_m$ , the *Magnetic Reynolds number*, as the ratio of the two terms on the right side of the induction equation (Equation 1.14). The first of these is known as the advection term and second is the diffusion term.

$$\begin{aligned}
 R_m &= \frac{|\nabla \times (\mathbf{v} \times \mathbf{B})|}{|\eta \nabla^2 \mathbf{B}|}, \\
 &\approx \frac{v_0 B / l_0}{\eta B l_0^2}, \\
 &\approx \frac{l_0 v_0}{\eta} = \frac{l_0^2}{\eta t_0}.
 \end{aligned} \tag{1.15}$$

If  $R_m$  is large (resp. small), we can neglect the magnetic diffusion term (resp. the advection term). On the Sun,  $R_m$  is normally very large because  $l_0$  and  $v_0$  are typically large. However there are several important exceptions, for example, where length scales become small (e.g. in current sheets, during magnetic reconnection and during solar flares). When we have a typical velocity equal to the Alfvén velocity ( $v_0 = v_A$ ) the Magnetic Reynolds number can be called also Lundquist number (denoted by  $S$ ).

When magnetic diffusion is negligible, the plasma behaves in what is known as an ideal manner and its behaviour is governed by an important property discovered by Alfvén (1943).

**Theorem 1.3.1.** Frozen-in-Flux Theorem (Alfvén’s Theorem)

*In a perfectly conducting fluid ( $R_m \rightarrow \infty$ ), magnetic field lines move with the fluid: the field lines are “frozen” into the plasma.*

Motions along the field lines do not change them, but motions traverse to the field carry the field with them. This can also be generalised to any closed contour moving with the fluid. This means that the flux initially confined by a closed curve remains the same in time even if the curve is moved and deformed. The behaviour of the magnetic field in this case is governed by:

$$\frac{\partial \mathbf{B}}{\partial t} = \nabla \times (\mathbf{v} \times \mathbf{B}).$$

### 1.3.3 Magnetic field lines

A magnetic field line, sometimes called a line of magnetic force, is a space-curve  $\mathbf{r}(\ell)$  which is everywhere tangent to the local magnetic field vector ( $\mathbf{B}$ ).

This description can be rewritten as the differential equation

$$\frac{\partial \mathbf{r}}{\partial \ell} = \frac{\mathbf{B}(\mathbf{r}(\ell))}{|\mathbf{B}(\mathbf{r}(\ell))|}, \quad (1.16)$$

where the parameter  $\ell$  is the arc-length forward along the field line from  $\mathbf{r}(0)$ . A field line is a curve, and therefore has zero volume. A *flux tube* may be constructed by bundling together a group of field lines, so that both the cross-sectional area of the tube and the field contained may vary along the length of the tube, but the magnetic flux is always constant.

### 1.3.4 Magnetic topology

For a continuous magnetic field,  $\mathbf{B}$ , the field line Equation 1.16 is singular only where the magnetic field vector vanishes. In a general field,  $\mathbf{B}$  will vanish only at isolated points called *null-points* which constitute key topological features of a magnetic field. In many cases the structure of the field can be characterised entirely in terms of the so-called magnetic skeleton formed by sources, null points, separatrix surfaces, spines and separators (Cowley, 1973, Priest et al., 1997).

Points where the magnetic field vanishes (i.e.  $B_x = B_y = B_z = 0$ ), called *null-points*, play a crucial role in defining these boundary elements (Fukao et al., 1975, Greene, 1988). Their nearby linear structure has been studied in detail by Parnell et al. (1996). Figure 1.8 illustrates this basic structure in three dimensions.

In the region around the null the magnetic field can be approximated, locally, using a Taylor expansion. If in particular we consider just the linear term, we can rewrite the magnetic field in the form:

$$\mathbf{B} = \mathbf{M} \cdot \mathbf{r}, \quad (1.17)$$

where  $\mathbf{M}$  is the Jacobian matrix:

$$\mathbf{M} = \begin{pmatrix} \partial B_x / \partial x & \partial B_x / \partial y & \partial B_x / \partial z \\ \partial B_y / \partial x & \partial B_y / \partial y & \partial B_y / \partial z \\ \partial B_z / \partial x & \partial B_z / \partial y & \partial B_z / \partial z \end{pmatrix}. \quad (1.18)$$

In non-degenerate cases, three eigenvalues can be associated with this matrix. One eigenvalue (which we will denote  $\lambda_1$ ) will be of the opposite sign to the other two ( $\lambda_2$  and  $\lambda_3$ ) due to the solenoidal constraint (Equation 1.5) which implies that

$\sum_{i=1}^3 \lambda_i = 0$ . If  $\lambda_2$  and  $\lambda_3$  are positive, then the null is said to be “positive” whereas if they are negative, the null is “negative” (Priest and Titov, 1996, Beveridge et al.,

2002). Cases where one or more eigenvalue real parts vanish cannot be classified as either positive or negative. Such cases are not generic (they will not survive a small but arbitrary perturbation of the field) but do occur in cases of symmetry, such as two-dimensional models. An X-type null is one where one eigenvalue vanishes, namely  $\lambda_2$ , and the other two have equal magnitude and opposite sign:  $\lambda_1 = -\lambda_3$ . This is a standard hyperbolic fixed point of two-dimensional vector fields, however, as alluded to, they do not generally occur as such in three-dimensional fields. If the real parts of two eigenvalues vanish then so must the third, since they must sum to zero, barring a higher-order null (all three eigenvalues are identically zero) this must be an O-type null with two purely complex eigenvalues (Longcope et al., 2005).

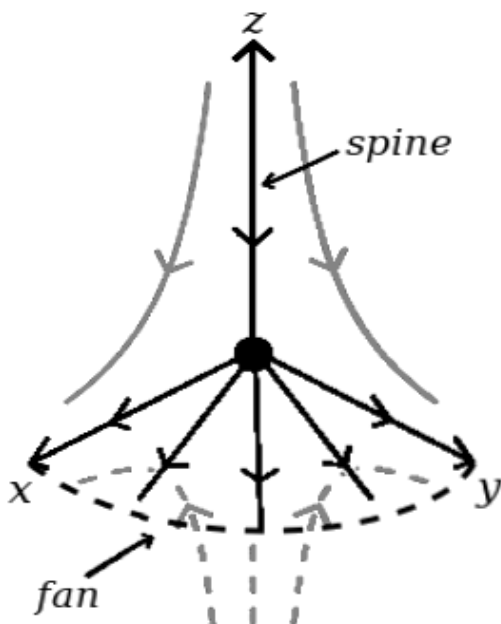


Figure 1.8: The structure of the magnetic field around a 3D null point. The null here is positive, so the spine, which lie on the  $z$ -axis, is directed towards the null point. The field lines tangent to the fan surface are directed away from the null point and lie radially in the  $x$ - $y$ -plane.

The eigenvector associated with  $\lambda_1$  defines a “spine” line, which, if the null point is positive (as in the Figure 1.8), then the field lines around this line are directed towards the null. If the null is negative, the field lines are directed away from the null along the spine.

The other two eigenvectors define a plane of field lines known as a “fan” plane or fan surface (Priest and Titov, 1996). If the null is negative (i.e.  $\lambda_2$  and  $\lambda_3$  are negative), these field lines converge on the null; if the null is positive, the fan field lines diverge from it. Far from the null, the field lines lying in the fan plane form a surface known as a separatrix surface.

A *separator* is defined as a field line that lies along the intersection of two distinct separatrix surfaces and hence is a line that joins two oppositely signed null points (Greene, 1988, Lau and Finn, 1990, Priest and Titov, 1996, Galsgaard and Nordlund, 1997, Close et al., 2005) and is thought to be a favourable site for current sheet

formation in response to changes to the boundary conditions (Lau and Finn, 1990, Longcope, 1996, Bungey et al., 1996). The separatrix surfaces separate the magnetic field into topological distinct domains: simply connected regions of different field line connectivity, called flux *domains* (Longcope, 2001). This topological description is a natural extension in 3D of the 2D model. The separator may be thought of as the generalisation in 3D of a 2D X-point (Figure 1.9).

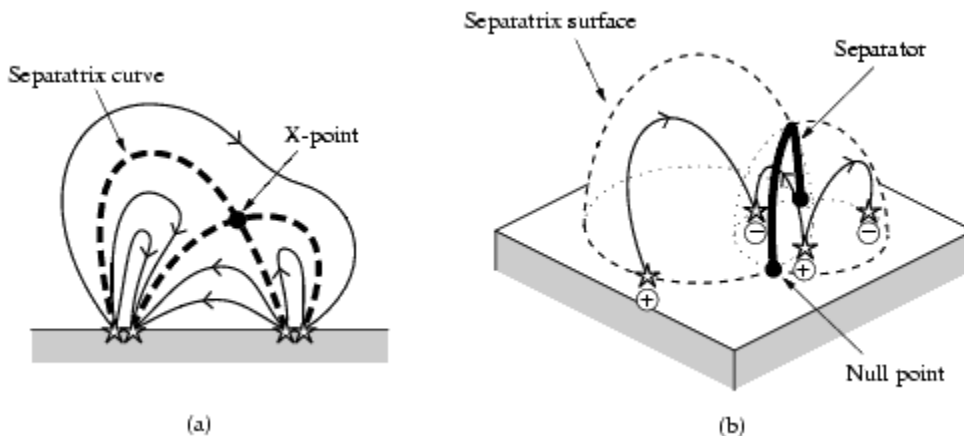


Figure 1.9: Topological skeletons (a) in 2D and (b) in 3D (From Priest et al., 2005a).

These concepts concerning magnetic field topology pervade plasma physics from the solar interior, to the magnetosphere, to the outer heliosphere. They are equally useful under static or dynamic conditions, in plasma of high or low  $\beta$  (which is the ratio of gas pressure to magnetic pressure, with or without non-thermal populations) provided only that non-ideal electric fields remain negligible or if these are localised. Even cases where this condition does not hold, such as ones involving magnetic reconnection, are studied using field topology, but restricted to the regions outside the reconnection region. Indeed, the simple characterisation of reconnection as “breaking” and “rejoining” magnetic field lines is a construction using field topology. This chapter presents an introduction to the analysis of magnetic field topology and reconnection. While the topic is general and applicable in most areas of space physics.

## 1.4 Reconnection

Magnetic reconnection is a phenomenon which is of particular importance in solar system plasmas and in plasma physics in general. In the solar corona, it can result in the rapid conversion of the magnetic energy stored in current sheets embedded

in the coronal magnetic field, an effect which is thought to give rise to solar flares. Small-scale reconnection may play a role in heating the corona, and, thereby, driving the outflow of the solar wind. In the Earth’s magnetosphere, magnetic reconnection in the magnetotail is thought to be the precursor for auroral sub-storms.

In 2D, magnetic reconnection takes place at null points with flux transfer across the separatrices. Sweet (1958) and Parker (1957) presented a 2D model for slow reconnection—too slow for solar flares. Then Petschek (1964) proposed the first model for fast reconnection. Later, Priest and Forbes (1986) discovered a wider family of almost-uniform solutions, including Petschek’s mechanism and Biskamp’s numerical experiments as special cases (Biskamp, 1986).

It is now a well established part of reconnection theory that, when the magnetic diffusivity is enhanced at the reconnection point, Petschek’s mechanism and the other Almost-Uniform reconnection regimes can indeed occur, and that an enhancement of diffusivity is a common effect in practice (Priest and Forbes, 1986).

In 3D, unfortunately, where the current accumulates, and then reconnection take place is not completely understood. In 3D several different regimes of reconnection have been proposed, including slip-running reconnection or quasi-separatrix layer (QSL) reconnection in the absence of a null point (Démoulin et al., 1996, Aulanier et al., 2006), separator reconnection at a field line that joins two null points (Parnell et al., 2010), and three kinds of reconnection at a null point, namely, torsional spine reconnection, torsional fan reconnection and spine-fan reconnection (Priest and Pontin, 2009). In our project we concentrate our investigation on the locations of QSL at which reconnection can occur.

### 1.4.1 Magnetic annihilation

Magnetic annihilation is an important ingredient of magnetic reconnection, referring to the carrying in and cancelling of oppositely directed straight field lines. In this situation a current sheet is created along the stagnation-point and naturally tends to diffuse outwards, and so a steady state may be set up if magnetic flux is carried in at the same rate it is diffusing. Following the Watson and Craig (1998) assumptions, if the system we are considering is two-dimensional, then the magnetic field  $\mathbf{B}$  may be expressed in the form  $\mathbf{B} = \nabla \times \psi(x,y)\hat{e}_z$ . We can combine Equations 1.1, 1.5, 1.8, 1.2, by taking the curl of the momentum equation and neglecting the gravitation term, to give

$$\nabla \times (\rho(\mathbf{v} \cdot \nabla)\mathbf{v}) = -[\nabla^2\psi, \psi]_z \quad (1.19)$$

$$\mathbf{v} \cdot \nabla\psi = E_z + \eta\nabla^2\psi \quad (1.20)$$

$$\nabla \cdot (\rho\mathbf{v}) = 0 \quad (1.21)$$

where  $[f,g] = \partial_x f \partial_y g - \partial_y f \partial_x g$ . If we consider a constant density, incompressible plasma, then we may make further simplifications by setting the plasma density

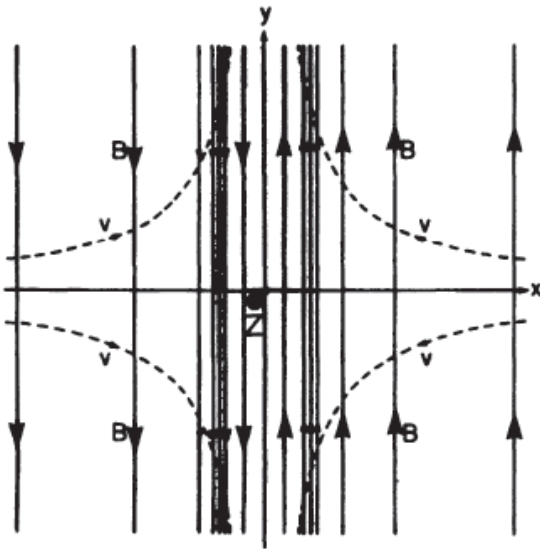


Figure 1.10: Oppositely directed field lines (solid lines) are carried in from the left and right by a stagnation flow with streamlines shown as dashed lines, assuming  $\phi = -\alpha xy$ . When the field lines enter the current sheet or diffusion region, centred on  $x = 0$ , they are no longer frozen to the plasma. In the diffusion region they are annihilated, the plasma flow out along the sheet prevents a pile-up of matter near the neutral line. Figure from Lakhina (2000).

$\rho = 1$  and writing  $\mathbf{v} = \nabla \times \phi(x,y)\hat{e}_z$ . The governing equations, written in terms of the new variables  $\phi$  and  $\psi$ , now reduce to

$$[\nabla^2 \phi, \phi] = [\nabla^2 \psi, \psi] \quad (1.22)$$

$$[\psi, \phi] = E_z + \eta \nabla^2 \psi \quad (1.23)$$

The relative simplicity of this system makes it possible to construct exact models for magnetic annihilation and reconnection.

Magnetic annihilation is an important ingredient of magnetic reconnection, referring to the carrying in and cancelling of oppositely directed straight field lines. The annihilation of antiparallel magnetic fields in incompressible plasmas (e.g. Sonnerup and Priest, 1975) can be described by Equations 1.22 and 1.23 by assuming that the flux function  $\psi(x,y)$  is a function of only one variable, i.e.,  $\psi = \psi(x)$  (Craig and Henton, 1995). Substituting this form for  $\psi$  into Equations 1.22 and 1.23 shows that  $[\nabla^2 \phi, \phi] = 0$  is a function of  $x$  only. These constraints admit three possible forms for the stream function, namely,

$$\phi = -\alpha xy, \quad \phi = -\alpha \sin(kx)y, \quad \phi = -\alpha \sinh(kx)y \quad (1.24)$$

The three resulting solutions for  $\psi$  all represent the steady-state annihilation of magnetic field in the vicinity of a flow stagnation point located at the origin (Figure 1.10).

We have shown only the steady-state annihilation solution, but there exist more general planar solutions based on fully two-dimensional current structures. We do

not report these in this thesis, but more details on these solutions can be found in Watson and Craig (1998).

### 1.4.2 Sweet-Parker mechanism

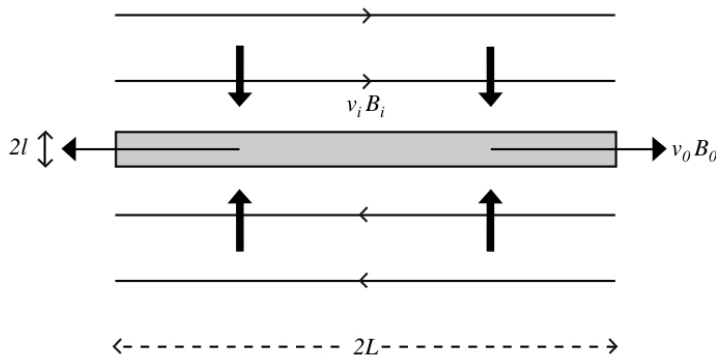


Figure 1.11: Sweet Parker mechanism. Sketch of the field lines (thin lines) and flow configuration (thick arrows). The current sheet (or diffusion region), drawn in grey, has a small width  $2l$  set by the scale of diffusion over its whole length  $2L$  which is taken as the scale size of the system. Figure from Priest (2010)

The Sweet-Parker mechanism is a two-dimensional reconnection process that dissipates magnetic energy (Sweet, 1958, Parker, 1957). The main features of the field and flow configurations for this model are shown in Figure 1.11. Sweet-Parker reconnection was the first model for steady magnetic reconnection.

For a steady state, the magnetic field of strength  $B_i$  is carried in at the same speed ( $v_i$ ) as it is being diffused outwards, so we can equate the rate at which the flux is carried into the current sheet on either side, to the rate of flux being transported through the diffusion region, so that

$$v_i = \frac{\eta}{l}. \quad (1.25)$$

If the density is incompressible, then the conservation of mass (Equation 1.1) requires that

$$\nabla \cdot \mathbf{v} = 0 \quad \text{or} \quad v_i L = v_0 l, \quad (1.26)$$

where  $v_0$  is the outflow speed. If the plasma is accelerated along the sheet by a Lorentz ( $\mathbf{j} \times \mathbf{B}$ ) force, the outflow speed is the Alfvén speed

$$v_0 = v_{Ai} = \frac{B_i}{\sqrt{\mu\rho}}. \quad (1.27)$$

Combining the Equations 1.25, 1.26 and 1.27, we obtain

$$v_i = \frac{v_{Ai}}{R_{mi}^{1/2}}, \quad (1.28)$$

in terms of the magnetic Reynolds number, or Lundquist number in this case, ( $R_{mi} = S = Lv_{Ai}/\eta$ ).

The reconnection rate can be described in dimensionless form by the inflow Alfvén Mach number, which is defined as

$$M_i = v_i/v_{Ai} = R_{mi}^{-1/2}, \quad (1.29)$$

with the inflow magnetic Reynolds number,  $R_{mi}$ . Including the effects of the pressure gradient makes this expression more complex; however, the same dependence on  $R_{mi}$  remains. For this reason, Sweet-Parker reconnection cannot explain energy release in solar flares, because the high magnetic Reynolds number of the corona means that the reconnection rate will always be too low for flares.

### 1.4.3 Petschek’s model

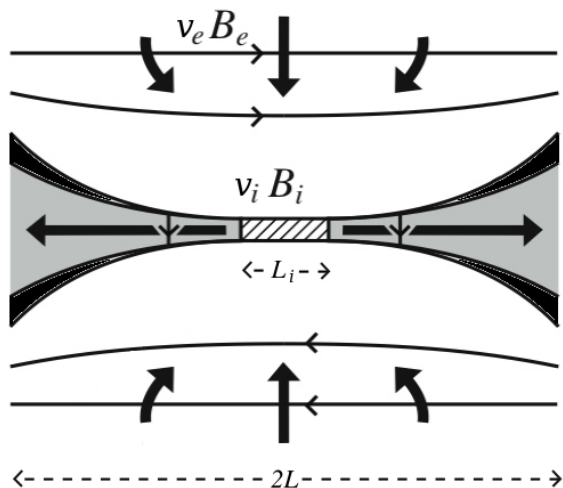


Figure 1.12: Petschek’s model. Sketch of the field lines (thin lines) and flow configuration (thick arrows). A small central diffusion region (hatched box) of length  $L_i$  surrounds the neutral line and the outflow propagate in regions (in grey) confined between two slow-mode shocks (in black). (Figure adapted from Priest (2010))

In Petschek’s model the field and flow configurations have an X-point caused by shocks (Figure 1.12). Petschek (1964) realised that a slow-mode shock provides another way (as well as a diffusion region) of converting magnetic energy into heat and kinetic energy. Two standing Alfvén shocks deflect and accelerate the incoming plasma in two exit jets wedged between the shocks. The diffusion region in this model can be seen as a miniature of the Sweet-Parker system. The reason for the small reconnection rate in the Sweet-Parker mechanism is due to the fact that the length of the diffusion region is equal to the system length  $L$  which is very large compared to its width  $l$ . Petschek (1964) suggested that if the antiparallel fields meet only over a short length  $L_i$ , rather than all along the system  $2L$  (Figure 1.12),

then the diffusion region may be thinner, and the reconnection can take place faster than in Sweet-Parker. This is known as *fast reconnection*.

In the Petschek analysis the magnetic field in the inflow region decreases from a uniform value ( $B_e$ ) at large distances to a value  $B_i$  at the entrance to the diffusion region given by

$$B_i = B_e \left( 1 - \frac{4M_e}{\pi} \log \frac{L_e}{L} \right). \quad (1.30)$$

Petschek suggested that the mechanism chokes itself off when  $B_i = \frac{1}{2}B_e$  in Equation 1.30, which gives a maximum reconnection rate ( $M_e^*$ ) of

$$M_e^* \approx \frac{\pi}{8 \log R_{me}}. \quad (1.31)$$

Since the maximum reconnection rate depends inversely on the logarithm of the magnetic Reynolds number, rather than its square root, it is much larger than that predicted by the Sweet-Parker model. Indeed, the rate was sufficiently large to explain the release of energy in solar flares.

#### 1.4.4 Reconnection in 3D

In 2D we have introduced the most important, but not the only, models of reconnection. These models are forms of 2D X-point reconnection since, in two dimensions, reconnection can occur only at an X-point (Figure 1.9). Generalising 2D X-point reconnection into 3D reconnection is non-trivial. One main difference is that generally in 3D, it is not possible to follow the evolution of pairs of field lines, it is only possible to follow pairs of flux surfaces. This is because, in 3D, reconnection does not occur at a single point involving just two pairs of field lines at any instant, as in 2D, but it occurs throughout a finite diffusion volume and at any instant involves a multitude of field lines.

A more general way to realise if the reconnection is occurring is to analyse the parallel component of the electric field, since such a component is a necessary and sufficient condition for reconnection in 3D (Hesse, 1988, Hesse and Schindler, 1988). In 3D, the rate of reconnection in a single isolated diffusion region is equal to the maximum of the integrated electric field parallel to the magnetic field (Hesse and Birn, 1993, Hornig, 2003). For all field lines that remain outside of the diffusion region for their entire length, their integrated parallel electric field will be zero. However, for all other field lines, the portion on their length that threads the diffusion region will contribute to the integral. So finding an enhanced  $\mathbf{E}_{\parallel}$  in numerical simulations ( $\int \mathbf{E}_{\parallel} dl \neq 0$ ) or deriving its existence from observed data (e.g. Fletcher and Hudson, 2002, Qui et al., 2002) is a good indicator that magnetic reconnection is taking place. In the particular case when  $\eta$  is constant, the parallel electric field

is simply related to the parallel electric current by a factor  $\eta$ . So the reconnection rate  $r_{rec}$  is given by:

$$r_{rec} = \max_{f \in \mathfrak{D}} \left[ \int_f E_{\parallel} dl \right] = \max_{f \in \mathfrak{D}} \left[ \eta \int_f j_{\parallel} dl \right], \quad (1.32)$$

where  $E_{\parallel}$  and  $j_{\parallel}$  are the components of the electric field and electric current parallel to the field line, respectively, and  $l$  is the distance along the field line considered  $f$  for all field lines belonging to a single diffusion region  $\mathfrak{D}$ .

It has been shown by Parnell et al. (2010) that it is not just the value of peak parallel electric field in the diffusion region that determines the rate of reconnection, but it is a combination of the size of the diffusion region and strength of the parallel electric field that matters in order to give an high integrated value of  $E_{\parallel}$ . Thus provided the diffusion volume is large enough (or if there are multiple diffusion regions as found in Haynes et al. (2007) and Parnell et al. (2008)), then it is not a problem to reconnect a large amount of flux in a very short interval time.

In 3D, it is possible for reconnection to occur at 3D null points (Priest and Titov, 1996), although 3D nulls have a very different structure to their 2D counterparts (Subsection 1.3.4). However, in 3D, reconnection can also take place along a separator (Parnell et al., 2008) or in a non-null region (Priest and Démoulin, 1995, Démoulin et al., 1996).

One of the main thrusts of reconnection theory at the moment is to understand the details of different ways in which it may occur in 3D.

### 3D null point reconnection

Priest and Titov (1996) considered kinematic models involving steady ideal evolution (satisfying  $\mathbf{E} + \mathbf{v} \times \mathbf{B} = 0$  and  $\nabla \times \mathbf{E} = 0$ ) in the neighbourhood of a null point or separator. Three types of reconnection at null points were proposed depending on where the currents concentrated, namely spine reconnection, fan reconnection and separator reconnection.

Later, the nature of the flow in the diffusion region was studied by Pontin et al. (2004) and computational experiments by Galsgaard et al. (2003), Pontin and Galsgaard (2007) led to a new categorisation. Priest and Pontin (2009) propose a division into three different types, depending on the nature of the flow near the spine and fan of the null.

**Torsional spine reconnection** occurs when there is a rotation of the field lines in the vicinity of the fan plane. This drives a current along the spine and gives rise to torsional spine reconnection due to the field lines becoming disconnected and rotating around the spine creating a rotational slippage.

**Torsional fan reconnection** where the field lines near the spine rotate in opposite directions above and below the fan and create a current that is concentrated in the fan with a rotational flux mismatch slippage. In both of these regimes, the spine and fan are perpendicular and there is no flux transfer across either the spine or fan.

**Spine-fan reconnection** is the most common in practice and combines elements of the previous spine and fan models. In this case, in response to a generic shearing motion that tend to fold the spine and the fan towards each other, the null point collapses. It forms a current sheet that is focused at the null itself, in a sheet that locally spans both the spine and fan. In this regime the spine and fan are no longer perpendicular and there is flux transfer across both of them.

### Separator reconnection

Magnetic separators are important locations of three-dimensional magnetic reconnection (Longcope and Cowley, 1996, Galsgaard et al., 2000, Parnell et al., 2010). Separators are lines that link pairs of opposite polarity null points (one positive and one negative, Figure 1.13) or, in other words, lines that lie at the boundary between four flux domains and represent the intersection of two separatrix surfaces. Since the intersection of two surfaces produces an X-type structure, when viewed along the line of intersection, the global three-dimensional topology of the magnetic field around a separator is hyperbolic. It is therefore usually assumed that the projection of the magnetic field lines themselves onto a two-dimensional plane perpendicular to a separator is also hyperbolic in nature. Parnell et al. (2010) show that the projection of the magnetic field lines in a cut perpendicular to a separator may be either hyperbolic or elliptic and that the structure of the magnetic field projection may change in space, along the separator, as well as in time, during the life of the separator. In separator reconnection the rate of reconnection is related to the amount of electric field parallel to the separator (Sonnerup, 1979, Hesse and Birn, 1993, Hesse, 1995, Parnell et al., 2008) (Equation 1.32).

Studying the nature of the parallel electric fields along the separator reveals where the reconnection is occurring along it. The reconnection, in fact, along the separator, occurs where there are high parallel electric fields and, hence, when there is a constant resistivity, high parallel currents. In magnetic reconnection the null point in 2D has a key role (Sonnerup, 1979, Lau and Finn, 1990), but in 3D this is not the only location important and, in particular, not for separator reconnection. Parnell et al. (2010) have found that separator reconnection is distinct from null point reconnection and does not seem to involve reconnection at the null points at the end of the separator.

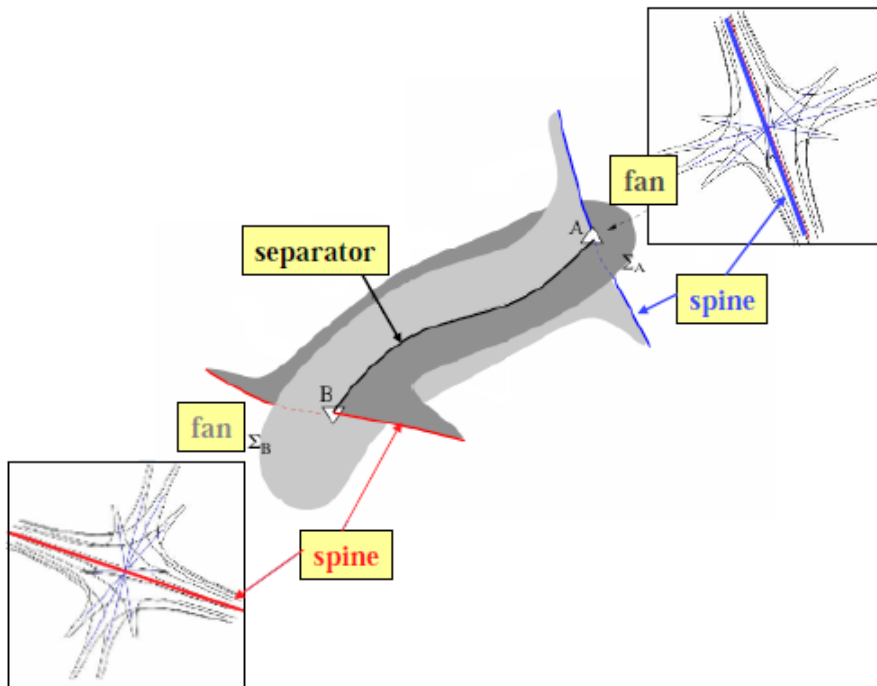


Figure 1.13: The structure of a null-null separator line. Positive and negative null points  $B$  and  $A$  have separatrix surfaces  $\Sigma_B$  and  $\Sigma_A$  shown in light and dark shades of grey and spines in red and blue, respectively. The nulls structure is shown in the boxes. (Figure adapted from Longcope et al. (2005))

### 1.4.5 Quasi-separator reconnection

As we said reconnection in 3D does not require the presence of a null point, but can take place also in a non-null region. One type of non-null reconnection is quasi-separator reconnection which was introduced by Démoulin et al. (1996). This reconnection involves the presence of so-called “quasi-separatrix layers” (QSLs). In this type of reconnection, the field lines close to the QSLs continuously change their connectivity at a very rapid rate as opposed to having a discontinuous change in connectivity as seen in 3D null reconnection i.e., they slip along one another. This is the reason why the Aulanier et al. (2006) termed this type of reconnection “slip-running” reconnection.

#### Quasi-separatrix layers

Quasi-separatrix layers (QSLs) are regions where there is rapid change in field line connectivity (Priest and Démoulin, 1995, Démoulin et al., 1996). In other words, these regions correspond to large mapping distortions or strong “squashing” of flux tubes (Titov et al., 2002). QSLs can be calculated by measuring the squashing degree  $Q$  related with the photospheric boundary plane  $z = z_0$ .

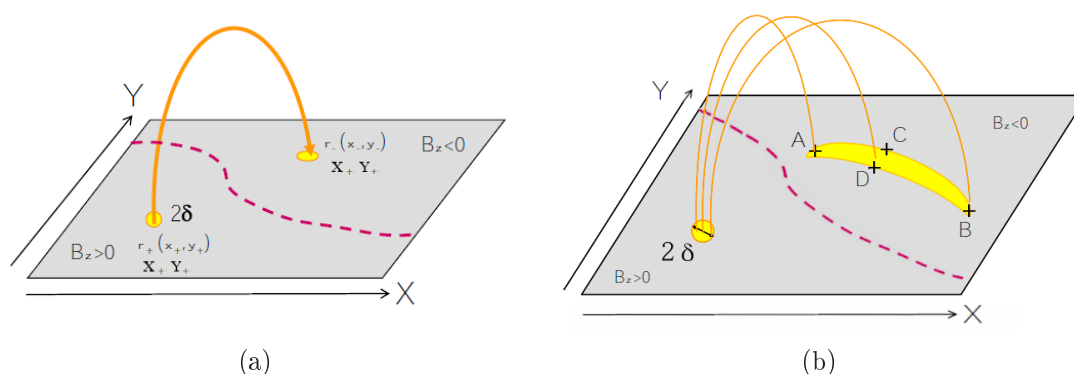


Figure 1.14: (a) Field line mapping. (b) Example of field line connectivity.

Let us consider, in Cartesian geometry, the field line mapping (Figure 1.14 a) from one footpoint in a given layer  $z_0$  to another in the same layer:  $r_+ = (x_+, y_+, z_0) \rightarrow r_- = (x_-, y_-, z_0)$ . Also, one may consider the reverse mapping. These mappings can be represented by vector functions  $[X_-(x_+, y_+), Y_-(x_+, y_+)]$  and  $[X_+(x_-, y_-), Y_+(x_-, y_-)]$ , respectively. From these, for the determination of QSLs, Priest and Démoulin (1995) proposed to use the functions  $N(r_+)$  and  $N(r_-)$  (called “the Norm” because they

represent the norm of the respective Jacobian Matrices):

$$\begin{aligned} N(r_{\pm}) &= \sqrt{\left(\frac{\partial X_{\mp}}{\partial x_{\pm}}\right)^2 + \left(\frac{\partial X_{\mp}}{\partial y_{\pm}}\right)^2 + \left(\frac{\partial Y_{\mp}}{\partial x_{\pm}}\right)^2 + \left(\frac{\partial Y_{\mp}}{\partial y_{\pm}}\right)^2} \\ &\equiv N_{\pm}. \end{aligned} \quad (1.33)$$

To better visualise this coefficient we can rewrite  $N$  referring to the particular case on Figure 1.14 b, obtaining:

$$N = \frac{\sqrt{|AB|^2 + |CD|^2}}{2\delta}. \quad (1.34)$$

It was proposed that  $N(r_{\pm}) \gg N_{\min} = 1$  defines field lines belonging to QSLs (Démoulin et al., 1996), and that the map of  $N(r_{\pm}, z = z_0)$  is the footprint of the QSL.

When different normal field components ( $B_{z+}$  and  $B_{z-}$ ) arise at the field line footpoints, a difficulty with the definition of QSLs by Equation 1.33 is that  $N(r_+) \neq N(r_-)$  if  $|B_{z+}| \neq |B_{z-}|$ . To overcome this, Titov et al. (2002) defined another characteristic function for QSLs which is independent of the mapping direction, called the squashing degree  $Q$ . It is calculated as follows:

$$Q_{\pm} = \frac{N_{\pm}^2}{|B_{z\pm}/B_{z\mp}^*|} \equiv Q_{\mp}^* = \frac{N_{\mp}^{*2}}{|B_{z\mp}^*/B_{z\pm}|} \equiv Q, \quad (1.35)$$

where the functions that have asterisks indicate that their arguments  $x_-$  and  $y_-$  are substituted in  $X_-(x_+, y_+)$ , and  $Y_-(x_+, y_+)$  respectively. With this prescription a QSL is defined by  $Q \gg Q_{\min} = 2$  and the map of the largest  $Q$  values on the plane ( $z = z_0$ ) values shows the footprint of the QSL.

### Bald patches

An additional feature that could be used to define a quasi-skeleton is the “bald patch” (Titov et al., 1993). Bald patches (BPs) are regions where some field lines are tangentially touching the boundary (i.e. the photosphere). This can happen along portions of the polarity inversion line (PIL) which is a location where the normal magnetic field on the photosphere changes sign. Fieldlines which head through a BP come from the corona (or chromosphere) and fall to the photosphere, touching the PIL on the BP before rising up into the corona again as shown in Figure 1.15. The criteria for the existence of BPs was first given by Seehafer (1986), and in more detail by Titov et al. (1993). The condition for such a feature to exist is that

$$(\mathbf{B} \cdot \nabla) B_z|_{z=z_0} > 0. \quad (1.36)$$

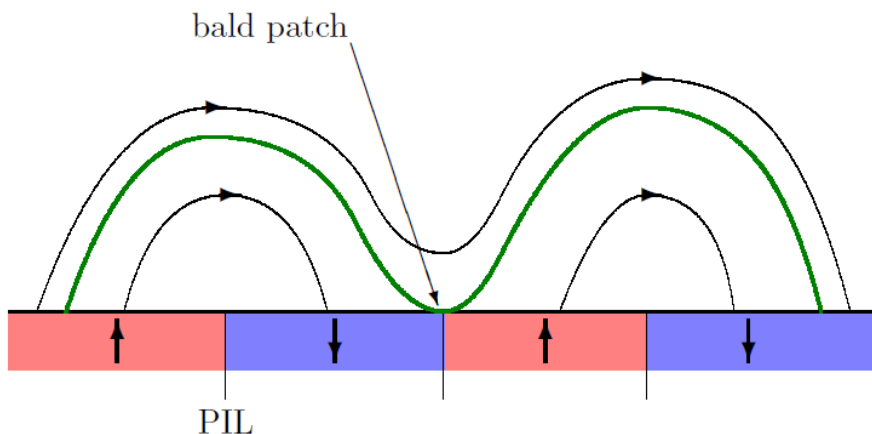


Figure 1.15: Sketch of a bald patch configuration in 2D. The bald patch is marked on a polarity inversion line (PIL) with two bald-patch separatrices (green lines) extending in each direction. The red regions denote upwards flux through the photosphere, blue denotes downwards flux.

BPs are interesting topological features for several reasons. They define “bald-patch separatrix surfaces” where current layers can develop (see e.g. Low and Wolfson, 1988, Vekstein et al., 1991, Aly and Amari, 1997), but unlike separatrix surfaces, these surfaces are not closed, and thus bald patch separatrix surfaces cannot fully divide the magnetic field. BP separatrices, starting at two distinct BPs, may intersect defining a topologically special field line, called separator line (BP-BP line), where magnetic reconnection is quite plausible (Bungey et al., 1996). In this aspect BPs are important since, contrary to the traditional definition, such separator does not connect two null points. Besides, during the evolution of some magnetic configurations, BPs may be precursors of the emergence of a null point in the coronal field (Bungey et al., 1996), being again associated with reconnection processes. Furthermore, BPs are thought to be the locations where chromospheric material can be lifted up and, so, they can be also linked to processes occurring in prominences (Titov et al., 1993, Aulanier et al., 1998). Titov and Démoulin (1999) extended previous studies on BPs to a non-linear force-free magnetic configuration representing a twisted flux tube (see Chapter 4).

### Squashing degree $Q_{\perp}$

A recent definition has been introduced for the squashing degree  $Q_{\perp}$  (Titov, 2007), which takes into account the inclination of the field lines with the plane  $z = z_0$ , considering the squashing only in the directions orthogonal to the field lines. The aim of  $Q_{\perp}$  is to provide a more precise description of the magnetic field structure in

a 3D volume, removing from the QSL footprint projection effects that depend only on the orientation of the vectors of magnetic field arriving at  $z = z_0$  the plane of the footprint. Deriving  $Q_{\perp}$  in the case of a closed magnetic configuration described in a global Cartesian system of coordinates  $(x, y, z) = (x^1, x^2, x^3)$  with the photospheric boundary plane  $x^3 = 0$  (on which we calculate the  $Q_{\perp}$ ), we obtain:

$$Q_{\perp} = \frac{N_{\perp}^2}{|\Delta_{\perp}|}, \quad (1.37)$$

where

$$N_{\perp}^2 = \frac{\partial X^i}{\partial x^k} \left( \delta_{ij} - \frac{B_i^* B_j^*}{|\mathbf{B}^*|^2} \right) \frac{\partial X^j}{\partial x^l} \left[ \delta^{lk} + \frac{B^l B^k}{(B_3)^2} \right], \quad (1.38)$$

and

$$|\Delta_{\perp}| = \frac{|\mathbf{B}|}{|\mathbf{B}^*|}, \quad (1.39)$$

where  $\delta$  is the Dirac delta function, with  $i, j = 1, 2$  which indicate the location of the end (target) footprint in the photosphere  $(X^1, X^2) = (X, Y)$  and  $k, l = 1, 2$  which indicate the location of the starting footprint  $(x^1, x^2) = (x, y)$ . The asterisk on the magnetic field indicates that it is relate to the target footprints.

QSLs resulting from  $Q_{\perp}$  are very similar in shape and location to those calculated with  $Q$  in the same magnetic field configuration (Titov, 2007). There is one difference, though. By considering a change of the plane at which the squashing degree is calculated, from the footprint plane to the plane that crosses the field lines perpendicularly, this new formula removes the portion of the QSL that is due to very flat field lines, i.e., those whose perpendicular plane is almost at right angles to the footprint plane. Thus, the regions identified by  $Q_{\perp}$  are usually similar to those found by  $Q$ , but they tend to remove projection effects such as those that occur near bald patches (Titov et al., 1993).

Hereafter, we are going to investigate the relation between quasi-topology ( $Q$ -factor and/or  $Q_{\perp}$ ), topology and current on different data representing the magnetic field in the solar atmosphere. In Chapter 2 we consider a magnetic system derived from observed surface magnetic field: a non-linear force free magnetic field extrapolation. We take a solar flare event from December 2006 considering, in particular, two snapshots, one before and one after a flare. In Chapter 3 we consider the easiest and basic way to represent a magnetic system creating a potential field from a distribution of sources. We take different potential point source models: two four sources models already presented in the literature and a random distribution of fifteen sources. In Chapter 4, we close our study investigating two different flux rope emergence simulations. In particular we take one case with unmagnetised ambient field and one with an overlying magnetic field. We conclude summarising our main results and possible ideas for future work.

# Chapter 2

## Investigation of QSLs in a solar flare

### 2.1 Coronal magnetic field approximations

The magnetic field in the solar corona plays a key role since in this region the plasma  $\beta$  is low. Determining the magnetic field in the corona is crucial for understanding the behaviour of this region. Knowing the magnetic field and how it evolves would provide a direct link between theoretical models and observations, allowing us to compare magnetic field structures with observed plasma structures. However, magnetic fields are often very complex, but determining the magnetic topology (null points, separatrix surfaces, bald patches) or geometry (e.g. QSLs) of the field provides the key information which describes the structure of the magnetic field in a much simpler way than plotting thousands of individual field lines. At the present, there are different methods that are used to estimate the magnetic field in the solar corona. All of them extrapolate the magnetic field from the photosphere. This is because at the moment it is not possible to have direct measurement of the coronal magnetic field. The main problem is that the corona is optically thin and we do not know where we are sampling the field. Photospheric magnetograms are produced by taking advantage of the Zeeman effect in which spectral lines over-split under the presence of a magnetic field. In the corona this measurement is not easy, due to the corona's low density, the lack of suitable strong spectral lines and due to the fact the field in corona is much weaker than in the photosphere: typically a few Gauss (10 G vs. 1000 G). This means that the Zeeman splitting effect is too small to be measured accurately.

In models of the Sun's magnetic field there are different ways to approximate the magnetic field on the base of the domain using sources of flux. They can be classified into three different groups: point sources, finite sources and continuous fields (e.g. Parnell, 2007). Point sources are isolated infinitesimally small sources of magnetic flux, discrete sources are also isolated (i.e. are separated by regions of zero

field normal to the boundary) but have finite size, and for continuous fields there can be a component of the magnetic field normal to the photosphere everywhere.

Modeling the magnetic field on the photosphere as discrete finite sources or as continuous field gives a better representation of the Sun’s magnetic field than point sources, however, the later technique is far easier to implement and so is more commonly used. In this case the magnetic field can be approximated with a set of photospheric point magnetic charges (point sources) or unipolar regions of photospheric flux. These lead to models known as magnetic charge topology (MCT) models. The topology of the magnetic field, in these models as in all finite sources models, is defined by its null points, most of which occur on the sources plane, the separatrix surfaces and the separators that extend from these null. These divide the photosphere into domains (Section 1.3.4). These models consider any two field lines with both their footpoints in the same domain to be topologically equivalent. The most natural partitioning occurs when each unipolar region is surrounded by a vertical field-free “sea”, or is a point magnetic source located at the photosphere. This definition of topological equivalence is most natural with point charges since there is only one footpoint location for each region: the charge itself. A related class of models use the potential field from a set of submerged ( $z < 0$ ) charges or dipoles to produce a smooth photospheric field (Seehafer, 1986, Gorbachev and Somov, 1988, Démoulin et al., 1992b). Photospheric regions are then defined by the mapping from submerged poles and may be delineated by curves mapping from fans of submerged null points as discussed in detail in Section 3.1. As we said, the vertical magnetic field on the photosphere can be also assumed to be continuous and vanishing only along curves known as polarity inversion lines (PILs). Here the magnetic field is defined starting from a continuous map of field on the photosphere taken from smoothed magnetograms or approximations to them and the magnetic field in the volume is calculated through extrapolations (Section 2.2). Where the field on the photosphere is modelled by a continuum the topology of the magnetic field will often be less complex due to the loss of the majority, if not all, of the null points on the photospheric boundary. Here, instead, by considering the geometry of the field, a quasi-skeleton may be found including quasi-separatrix surfaces and quasi-separators or hyperbolic flux tubes (Titov et al., 1993, Priest and Démoulin, 1995, Titov and Hornig, 2002). In these types of magnetic fields sources and flux domains may be identified with flux domains bounded by quasi-separatrix “surfaces”.

In this chapter, we concentrate our attention on this last method. First (in Section 2.2) we introduce the concept of a magnetic field extrapolation and then (in Section 2.3) we concentrate our attention on a particular set of data regarding the solar flare on 12-13 December 2006 which occurred in the active region NOAA 10930.

## 2.2 Magnetic field extrapolation

As already mentioned the magnetic field dominates the structure of the solar corona, but unfortunately direct measurements of coronal magnetic fields are not available. Routine measurements of magnetic field with sufficient accuracy and spatial resolution are only possible in the photosphere. The photospheric magnetic field is measured routinely with vector magnetographs, so one common approach is to extrapolate the magnetic field into the corona using the measured magnetic field as a boundary condition. We can extrapolate from photospheric measurements neglecting velocity variations ( $v \ll v_a$ ), so the equation of motion (Equation 1.9) becomes:

$$-\nabla p + \rho \mathbf{g} + \mathbf{j} \times \mathbf{B} = \mathbf{0}. \quad (2.1)$$

In a large part of the corona the plasma pressure is much less strong than the magnetic pressure ( $p \ll \frac{B^2}{2\mu}$ ). This means that their ratio ( $\beta$ ) is much lower than one. The pressure scale height ( $H = \frac{p}{g\rho}$ ) is extremely large in the corona ( $\sim 6 \times 10^4$  km) and in particular larger than our length scale,  $l$ . It has been shown from (Woltjer, 1958, Gold and Hoyle, 1960) that under these conditions ( $\beta \ll 1$ ,  $l \ll H$ ) the pressure and the gravity force can be neglected. This reduces Equation 2.1 to have only the Lorentz force component,

$$\mathbf{j} \times \mathbf{B} = \mathbf{0}, \quad (2.2)$$

and this is called the “force-free” approximation. Using the Ampère’s law (Equation 1.7) we can rewrite Equation 2.2 as

$$(\nabla \times \mathbf{B}) \times \mathbf{B} = \mathbf{0}, \quad (2.3)$$

then, if the magnetic field is not potential (i.e.  $\mathbf{j} \neq \mathbf{0}$ ), the general solution is where the current is parallel to the magnetic field ( $\mathbf{j} \parallel \mathbf{B}$ ). Thus,

$$\mu \mathbf{j} = \alpha \mathbf{B}, \quad \Rightarrow \quad \nabla \times \mathbf{B} = \alpha \mathbf{B}, \quad (2.4)$$

for some scalar  $\alpha$  which may be a function of position (and time). The scalar function  $\alpha$  is not completely arbitrary. From the properties of vectors, we know that  $\nabla \cdot (\nabla \times \mathbf{B}) = 0$ , and therefore from Equation 2.4

$$\begin{aligned} \nabla \cdot (\nabla \times \mathbf{B}) &= \nabla \cdot (\alpha \mathbf{B}) \\ &= \alpha \nabla \cdot \mathbf{B} + \mathbf{B} \cdot \nabla \alpha \\ &= 0. \end{aligned}$$

Hence, after applying the solenoidal condition 1.5,

$$\mathbf{B} \cdot \nabla \alpha = 0 \quad (2.5)$$

so that  $\alpha$  is constant along each field line, but it may vary from field line to field line.

The force-free assumption leads to three different types of magnetic field.

**A potential field** corresponds to a minimum energy state for a given distribution of  $B_z(z = 0)$  and has the simplest physical assumption ( $\alpha = 0$ ), i.e. it is current-free:

$$\mu \mathbf{j} = \nabla \times \mathbf{B} = 0. \quad (2.6)$$

In this case the required photospheric boundary condition is just the vertical component of the magnetic field ( $B_z(z = 0)$ ). This is a well-posed boundary value problem given a unique solution for defined normal component of the magnetic field on the boundary. First considered by Schmidt (1964), this model has now led to an almost routine type of reconstruction, used for observational purposes (Sakurai, 1989), but also for building initial conditions for dynamical MHD numerical simulations and as initial conditions for other force-free relaxation models such as some of the ones listed on Table 2.1. The limitation of the current-free assumption becomes apparent in many active regions, where the magnetic configuration is known to have stored free energy and hence where currents are important.

**The linear force-free field** is based on the so called constant- $\alpha$  force-free hypothesis:

$$\nabla \times \mathbf{B} = \alpha \mathbf{B}, \quad (2.4)$$

where  $\alpha$  is a constant in the volume. Then by taking the curl of Equation 2.4 we obtain:

$$\nabla^2 \mathbf{B} = -\alpha^2 \mathbf{B}. \quad (2.7)$$

This is a Helmholtz equation that is linear and may be solved by the usual mathematical methods. Here the boundary conditions imposed are usually the vertical component of the magnetic field ( $B_z$ ) and a value for  $\alpha$  along with side and top boundary conditions. The value of  $\alpha$  has to be guessed, to be adjusted to coronal observations (e.g. Wiegmann and Neukirch, 2002, Carcedo et al., 2003), or to be derived from vector magnetograms (e.g. Leka and Skumanich, 1999, Leka et al., 2005). This condition allows the presence of electric currents in the corona, but the solution turns out to be non unique. To avoid this problem some authors consider the possibility of imposing more than one magnetic component at the boundaries. For instance, Hannakam et al.

(1984), Gary (1989) suggested that it is possible to impose two components of the magnetic field, while Kress (1989) proposed a least-squares approach (for which he presented a version valid for two-dimensional fields) in which all magnetic field components are used and Amari et al. (1997) generalised this technique to three-dimensional fields.

The main limitation of the linear force-free assumption is that electric currents are diffused, because the force-free field approximation implies that electrical currents run only along the field lines, while observations clearly show strong localised shear along the neutral line of many active-region magnetic configurations (Hagyard, 1988, Hofmann and Kalman, 1991). The only hope to incorporate strong localised electric currents is to assume that the coronal magnetic configuration is in a nonlinear force-free state.

**The nonlinear force-free field (NLFFF)** satisfies the following equations:

$$\nabla^2 \mathbf{B} + \alpha^2 \mathbf{B} = \mathbf{B} \times \nabla \alpha, \quad (2.8)$$

$$\mathbf{B} \cdot \nabla \alpha = 0, \quad (2.5)$$

where  $\alpha$  is a function of space. Equations 2.8 and 2.5 cannot be solved analytically and a range of different numerical schemes have been applied. The boundary conditions, for these schemes, depend on the method that it is chosen.

For simplicity we report the main numerical schemes and their boundary conditions in Table 2.1. The methods listed in Table 2.1 differ in the way they solve the system of differential equations, but, for all, the required boundary conditions, besides top and sides boundary conditions, are to specify the values of the vertical magnetic field  $B_z$  and  $\alpha$ . The first of these is the so-called *Grad & Rubin* technique (Craig and Henton, 1995). This method uses a potential field as an initial condition and then progressively currents are introduced into the system and the fields are relaxed towards a force-free state. The basic idea behind this scheme is to decompose the system of Equations 2.8 and 2.5 into two different systems: a hyperbolic part corresponding to the transport of  $\alpha$  along field lines, and an elliptic part updating the magnetic field configuration.

An alternative is the optimisation approach. In this approach (Wheatland et al., 2000, Wiegmann, 2004) a functional containing the force-free equations is minimised. The method directly uses the measured vector magnetograph data and an explicit computation of  $\alpha$  is not necessary.

A third possibility is to use vertical integration (Wu et al., 1990). In this scheme the boundary conditions are given by the measured magnetic field components on the photospheric boundary  $z = 0$ , which also define the  $\alpha$  parameter in this layer. From the horizontal derivatives at  $z = 0$ , it is possible

Method	bottom boundary conditions	boundaries on other sides	initial state	preprocess and comments
Grad & Rubin by Amari et al. (1999) by Sakurai (1989) by Wheatland (2006) by Inhester and Wiegelmann (2006) by Amari et al. (2006)	$B_z$ and $\alpha^\pm$ " " " "	closed " no $B_n$ unchanged $B_n$	potential " " " "	smooth $\alpha$ no no no no
Optimisation by Wheatland et al. (2000) by Wiegelmann (2004)	$B_x, B_y, B_z$ "	$B_x, B_y, B_z$ "	potential "	no minimising forces and torques
Vertical integration by Wu et al. (1990) by Démoulin et al. (1992a) by Song et al. (2006)	$B_x, B_y, B_z$ " "	no " "	no " "	no smoothing function smooth functions, asymptotic expansion
Evolutionary technique - stress and relax by Roumeliotis (1996) - evolutionary method by Mikic (1997) - magnetofriction by Valori et al. (2005, 2010) by van Ballegoijen et al. (2007)	$B_x, B_y, B_z$  $B_z, J_z$  " $B_z, \alpha^\pm$	no  closed  no "	potential  "  " non-force-free flux rope	matching $B_t$ and  external circuit  no "
Boundary elements by Yan and Li (2006)	$B_x, B_y, B_z$	closed	no	no
Finite elements by Amari et al. (2006)	$B_z, \alpha^\pm$	$B_n, \alpha^\pm$	potential	smooth $\alpha$

Table 2.1: Boundary conditions and initial states used to derive the NLFFF in the corona from photospheric or chromospheric boundary conditions for several numerical schemes (Extended from Régnier, 2007)

to calculate the vertical ones (e.g. Aschwanden, 2004) providing information on the field at level  $z + dz$ . We can then iterate this approach in the upwards direction to a desired upper boundary of the coronal volume. This method was numerically tested by Démoulin et al. (1992a). The main problem of this scheme is that it suffers from exponentially growing errors with height  $z$  associated with the mathematically ill-posed nature of problem. Mathematically it is possible to have a solution with eigenmodes that grow with height faster and faster for smaller and smaller horizontal magnetic features. Other problems of this scheme are that boundary conditions are imposed only on the bottom boundary and that when there is a small variation in the base boundary conditions, this can change the solutions dramatically of the extrapolated field lines and thus this is a big problem with noisy magnetogram data.

An alternative set of technique of a nonlinear force-free calculation method are the MHD-based techniques such as the evolutionary technique, the stress-and-relax method, and the magnetofrictional method. The MHD evolutionary method, as implemented by McClymont and Mikić (1994), follows the time-dependent evolution of the resistive, viscous, MHD equations using changing boundary conditions. An incompressible two-dimensional flow is imposed on the boundary in order to inject the observed current density (due to transverse field) in the magnetic configuration. The coronal resistivity is needed to allow the connectivity of field lines to evolve in time (i.e. to reconnect). The stress-and relax method (Roumeliotis, 1996) is very similar to the MHD evolutionary technique solving similar MHD equations. But the resistive relaxation is driven by the transverse components of the magnetic field and also includes the uncertainty of the magnetic field measurements. This method alternatively adjusts the vector potential field by stressing and relaxing phases until the transverse field at the lower boundary is optimally matched. The magnetofrictional method (Yang et al., 1986) uses a dissipative relaxation to drive the MHD equations towards an equilibrium. The boundary conditions are injected by a series a stress-and-relax procedures. This method has been implemented by Valori et al. (2005) with a zero plasma  $\beta$  which results in a final state close to a force-free state. In the same group of methods, van Ballegoijen (2004) developed an alternative method for constructing NLFFFs that does not require vector field data. Instead, the model requires measurements of the line-of-sight component of the photospheric field, which are more accurate than transverse field measurements and are not subject to the 180 degree ambiguity (McClymont et al., 1997). To constrain the distribution of  $\alpha$  in the model they use observations of  $H\alpha$  filaments or other coronal structures that are affected by the presence of coronal electric currents. The method involves inserting a magnetic flux rope into the coronal field at the location of

an observed  $H\alpha$  filament. An initially non-force-free flux rope is relaxed to a force free state using magneto-frictional relaxation. Recently this method has been improved including the effects of magnetic diffusion solving the MHD induction equation in the magnetofrictional relaxation (Bobra et al., 2008). This technique allows one to specify both the axial and poloidal fluxes of the flux rope, which can be estimated by comparing the resulting NLFFF model with the structure of the observed  $H\alpha$  filament. As in any numerical model, the magnetic field and current density are assumed continuous functions of position, so thin current sheets are excluded.

Another method was proposed by Yan and Sakurai (1997, 2000). A direct boundary integral formulation for a force-free magnetic field with finite energy content is presented. This is a new formulation for a three-dimensional nonlinear force-free field in which the boundary data can easily be incorporated.

The boundary integral equation method was first proposed by Yan and Sakurai (1997) and used to extrapolate the nonlinear force-free magnetic field in the solar atmosphere considering the half-space above the lower boundary with vanishing field at infinity. Yan and Li (2006) have further improved this method and propose the direct boundary integral equation formulation, which represents the nonlinear force-free magnetic field by direct integration of the magnetic field on the bottom boundary surface without the volume integral.

The last method that we mention here is the finite element method. The hyperbolic-elliptic system of the NLFFF field as described in the Grad & Rubin method section can be discretised using the finite element technique. The implementation of the finite elements has been done by Amari et al. (2006). It is important to note that the elliptic part is solved with a discretisation on non divergence-free finite elements. For the hyperbolic part, a linear system is solved, instead of propagating  $\alpha$  along a field line using a field line tracing technique Amari et al. (1999). The boundary conditions are similar to those for the Grad & Rubin method.

In addition to these methods there are others that are not discussed here. There are many different methods, but it is not clear which method is the best, with different methods being better than others on a case by case basis. Indeed, a number of papers have been published on comparing these methods (e.g. Schrijver et al., 2006, 2008, DeRosa et al., 2009).

Fortunately the comparison of the extrapolation methods for our event has already been done by Schrijver et al. (2008) computing 14 NLFFF models with four different codes and a variety of boundary conditions (see Schrijver et al. (2008) for more details). The best-fit model for our event was found to be the Wheatland positive-field solution ( $Wh_{pp}^+$ , Wheatland, 2004, 2006) applied to a preprocessed

lower boundary (including spatial smoothing). So we use the data extrapolated with this method to do our investigation.

### 2.3 12-13 December 2006 event

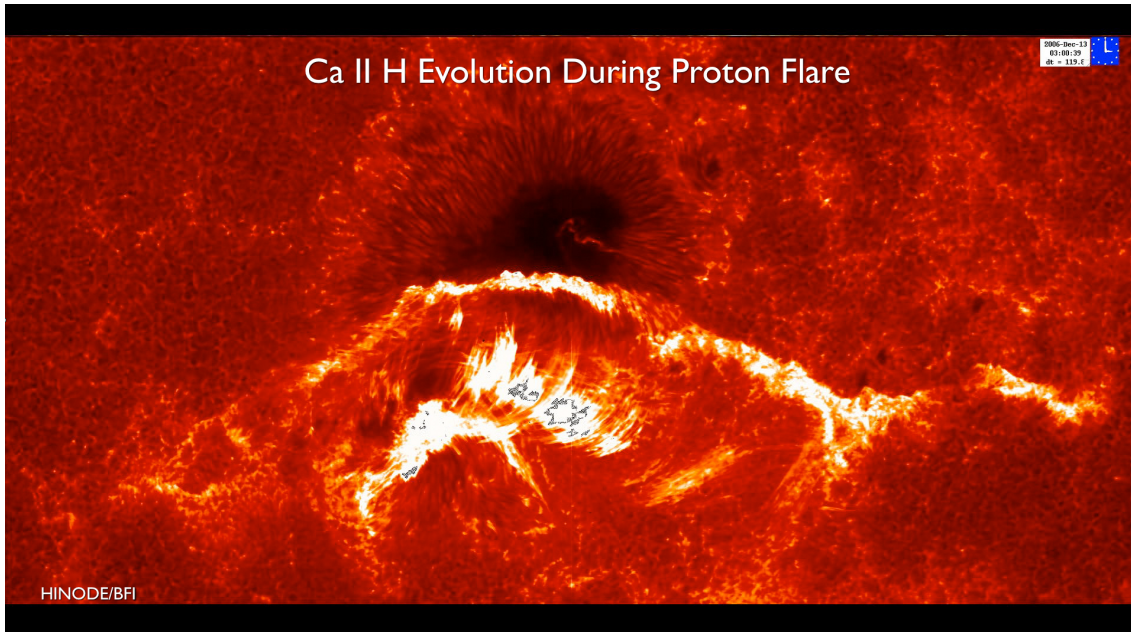


Figure 2.1: Observed NOAA AR 10930 at 03:00 13/12/2006 in the chromospheric Ca II H channel on Solar Optical Telescope (SOT) on board the Hinode spacecraft ([www.nasa.gov](http://www.nasa.gov)).

Solar flares and coronal mass ejections (CMEs) are the most energetic phenomena in the solar atmosphere, and are associated with rapid changes in field line connectivity. In this context the magnetic configuration and the evolution of the magnetic connectivity play a key role. Complicated magnetic topology and strong magnetic shear are necessary for a solar flare. Our goal is to investigate the QSLs in a solar flare before and after the event, and to determine the QSLs relation to the current occurring at the same time and to the magnetic topology.

With this aim we are going to investigate a particular event which occurred in active region NOAA 10930 on 12-13 December 2006. This was observed by the Solar Optical Telescope (SOT) and X-Ray Telescope (XRT) both on board *Hinode* and is an interesting event because it happened during solar minimum, therefore it is expected that the large scale topology was simple at this time.

During the evolution of the magnetic field leading up to this flare, we can see that there is a spin rotation of the positive spot around its own axis combined with

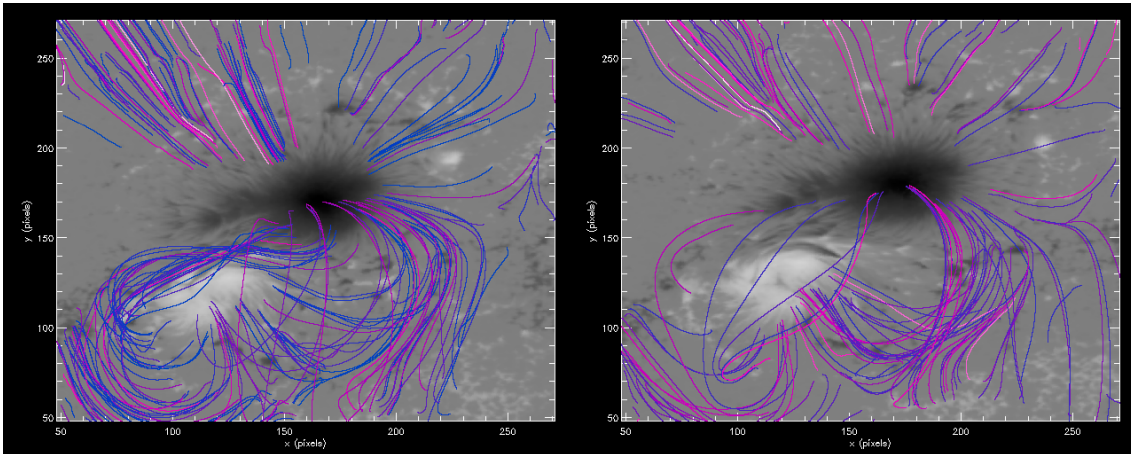


Figure 2.2: These images show the magnetogram on the photosphere before the event (20:30 12/12/2006) on the left and the magnetogram after the event (04:30 13/12/2006) on the right. The plots have 224x224 pixels area (with sides of 101 Mm). Black denotes a negative polarity (magnetic field pointing into the Sun) while white denotes a positive polarity (magnetic field pointing out of the Sun). Over plotted are some of field lines that “end” inside the box and have a  $\log(Q\text{-factor})$  greater than 3. Field line colour indicates strength of  $Q$ -factor along the field line. With violet is indicated low  $Q$  and with red and white high  $Q$ .

a strong eastward motion of the same spot around the negative larger neighbour located to its north <sup>1</sup>. Flux emergence between the two spots, as well in the area west of that, continued from the early hours of 10th December 2006 through to the second half of 14th December 2006, leading to an X3.4 flare during the early hours of 13th December 2006. In particular the overlying higher arched loops do not exhibit bright ribbons until approximately 2:30 UT (Figure 2.1).

We consider, for simplicity, two snapshots: one at 20:30 12/12/2006, before the flare and an other after the event, at 04:30 13/12/2006. The magnetograms for which are shown in Figure 2.2. As we have already mentioned, we use the magnetic field extrapolated from the magnetogram with Wheatland positive-field ( $Wh_{pp}^+$ ) model to trace field lines (Figure 2.2), calculate QSLs (Figure 2.6) and the null points (Figure 2.4).

The current has been already analysed by Schrijver et al. (2008) from which we take Figure 2.3. In this figure one can clearly see the location of the current sheet in the volume. The field line plots can be interpreted as a low altitude sheared arcade between the spots. We return to this point of the discussion later on in this chapter when we discuss the geometry of the field lines. Another thing that one can notice is that the current is much higher before the event than after ( $\sim$  three times more) and the main reason is because the flare has dissipated the current.

To compare the current with the topology, lets us consider the null points of these snapshots. As we already said the magnetic skeleton is strictly related with the null points. Calculating the nulls in these two snapshots we found 17 nulls (resp. 18) for the snapshot before (resp. after) the event. Unfortunately only three of these nulls from the first snapshot are coronal null points, while the others are all null points situated on the first vertical grid point. This is not good for our study because the null points so close to the magnetogram level are not reliable, in fact the location and number of them depend on the resolution of the magnetogram and the extrapolation method. The null points in higher grid points are more stable and they do not change drastically with the resolution of the magnetogram (e.g. Longcope and Parnell, 2009).

We investigated these three points (Figure 2.4). Two of them are positive and one negative. We plotted the structure of the positive nulls in red and blue with darker spine and lighter fan field lines and vice versa for the negative null that we plotted in green. Unfortunately these three null points are not sufficient to make a good comparison with the current location, first of all because they are located relatively far away from the current sheet. Furthermore their structure is not enough extended to get the picture of the complexity of the event and in particular they are not close to the location of the flare ribbons observed with SOT (Figure 2.1).

Therefore we require an other feature other than nulls and separatrices. We

---

<sup>1</sup>[http://www.lmsal.com/~schryver/NLFFF/HinodeNFI\\_X3.4\\_24hflareinterval.mov](http://www.lmsal.com/~schryver/NLFFF/HinodeNFI_X3.4_24hflareinterval.mov)

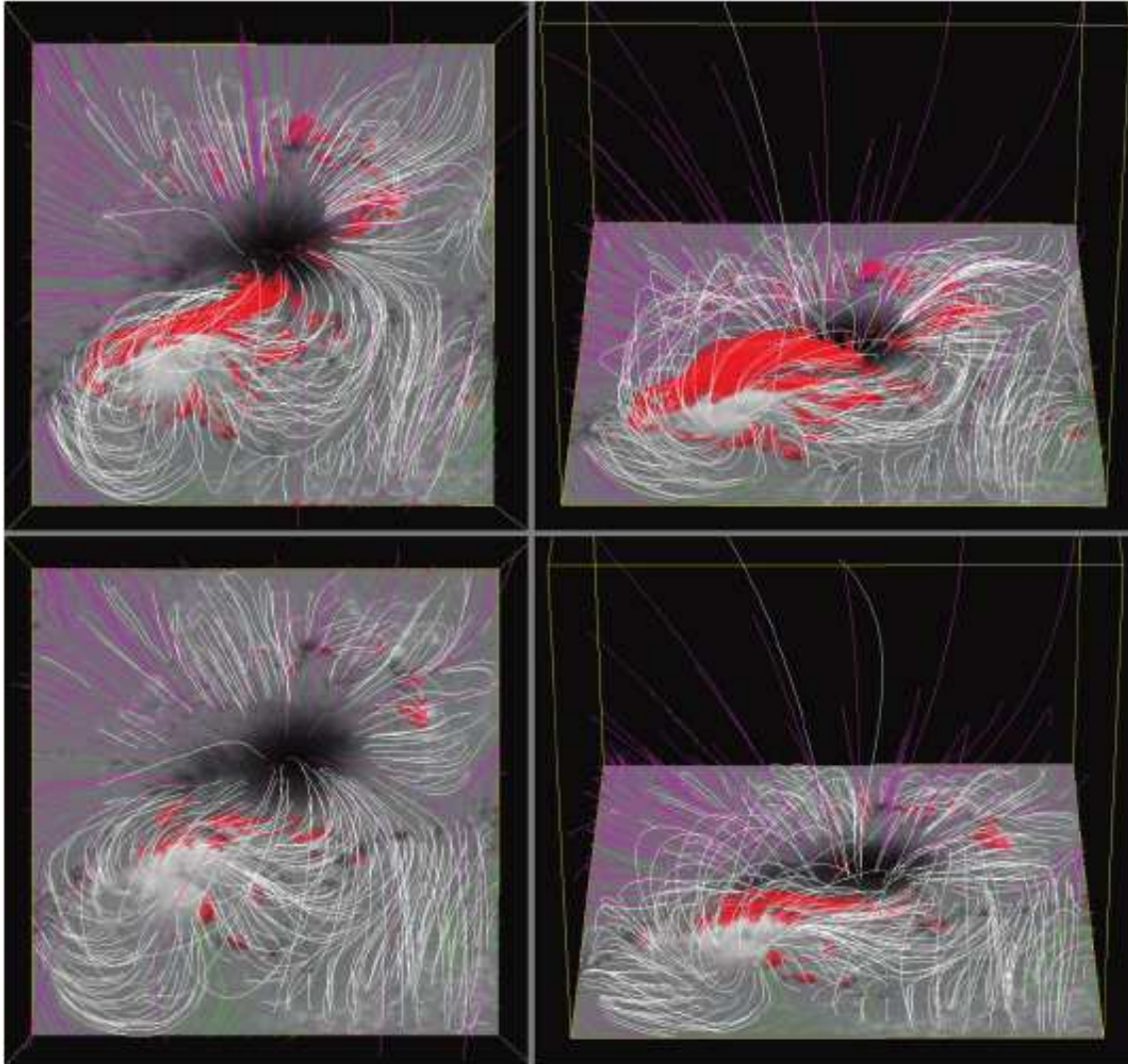


Figure 2.3: Visualisations of the magnetic field over NOAA AR 1930 before (top) and after (bottom) the X3.4 flare, shown against the corresponding map of  $B_z$ . Sample field lines outline the field; white field lines close within the NLFF model volume, while coloured field lines (purple or green for the two polarities of  $B_z$  at their base) leave the volume to connect to more distant regions. The rendered volumes (red) show where the electrical current densities are highest, using the same threshold level in both panels. (Figure from Schrijver et al. (2008)).

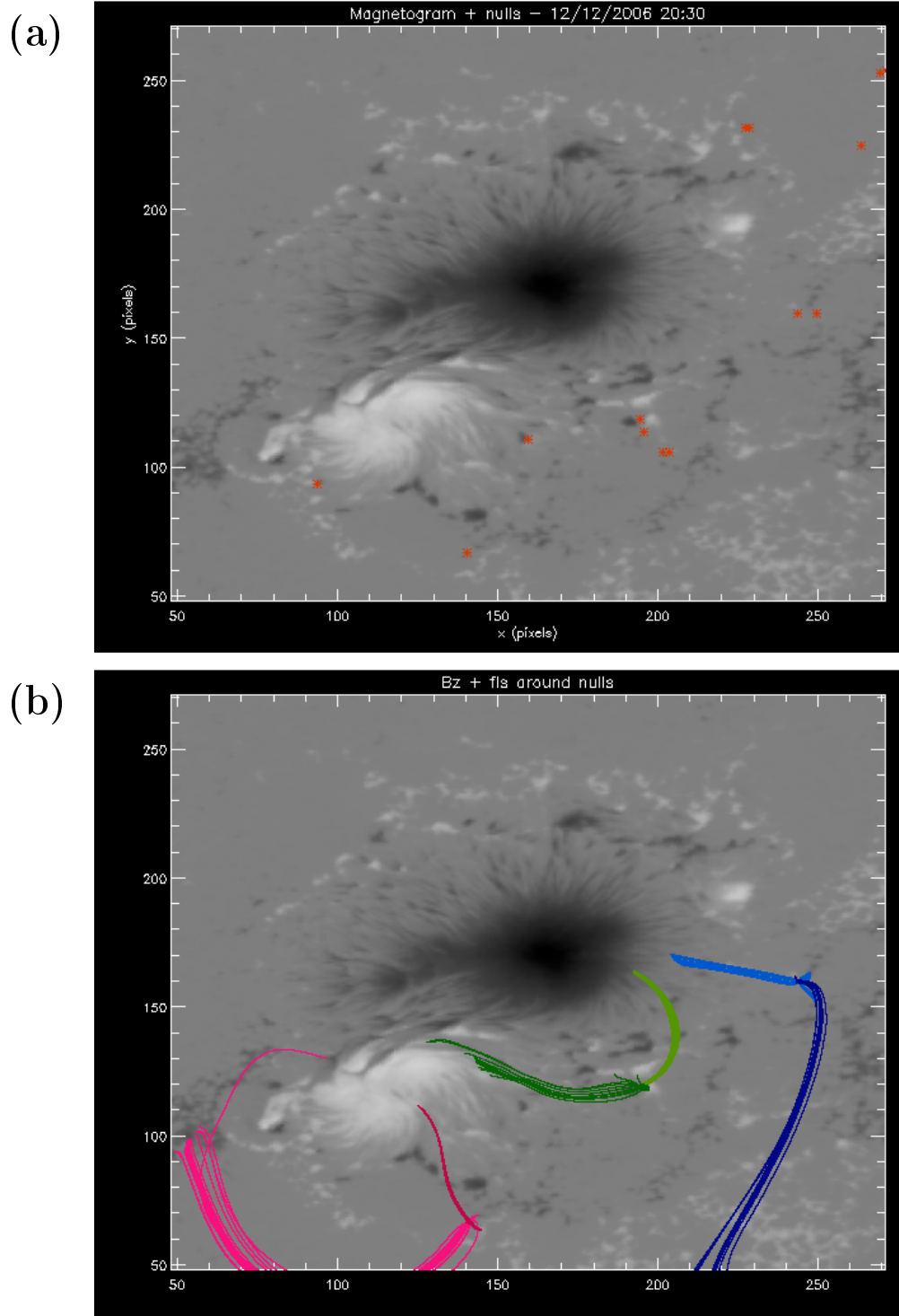


Figure 2.4: These images show before the flare, (a) the locations of the null points and (b) the field line around the 3 highest nulls: red is in the  $z = 3.10 \text{ pixel}$ ; blue in the  $z = 3.41 \text{ pixel}$ ; green in the  $z = 1.94 \text{ pixel}$ .

determine the so-called quasi-topology by investigating the QSLs. To determine it we need to choose a horizontal level from where we can calculate the squashing factor. As we show on Figure 2.5, it is not a good idea to take the photospheric level ( $z = 0 \text{ pixel}$ ) for this comparison, in fact the QSLs at this level (Figure 2.5 a) are really messy and there are a lot of small structures that are not necessary related with the flare but with small-scale magnetic field flux locations. This can be seen also in the current profile in Figures 2.5 b-c which show the current density cuts at different levels ( $z = 0 \text{ pixel}$  and  $z = 5 \text{ pixel}$ ) before the flare calculated using:

$$j = |\mathbf{j}| = |\nabla \times \mathbf{B}| .$$

On the photosphere, both the  $Q$ -factor and the current look messy and it is not useful to compare them, because it is difficult to observe the analogy due to their complexity (Figures 2.5 a-b). For this reason we chose to compare them by looking at a higher level, at  $z = 5 \text{ pixel}$  ( $z \simeq 3000 \text{ km}$ ).

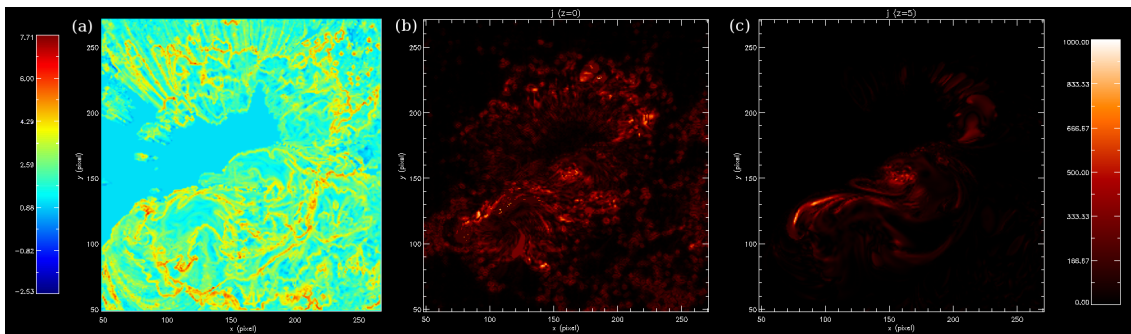


Figure 2.5: These images show (a) the QSL and (b-c) current densities with the same colourbar scale in a specific level at 20:30 12/12/2006. On the left (a-b) it shows the photosphere level ( $z = 0$  in the box) and on the right (c) it shows  $z = 5 \text{ pixel}$  ( $z \simeq 3000 \text{ km}$ ).

We can now compare the PIL (Figures 2.6 a1 and a2), QSLs footprints (Figures 2.6 b1 and b2) and the current on the same level (Figures 2.6 c1 and c2) for the two snapshots considered. We can clearly see that there is an affinity between them and that the QSL seems to highlight the contour of the current at the same horizontal cut. The current is higher before and lower after the event (Figure 2.6) similarly there are fewer regions with high  $Q$ -factor after the flare. These are similarities between them, but the correspondence is not one to one. As in the Wilmot-Smith et al. (2009) case, “no simple relationship has been found between the locations of maxima in the two quantities”.

As we said the main difference between the snapshots, before and after the event, is the complexity of the geometry of the magnetic field as evidenced by  $Q$

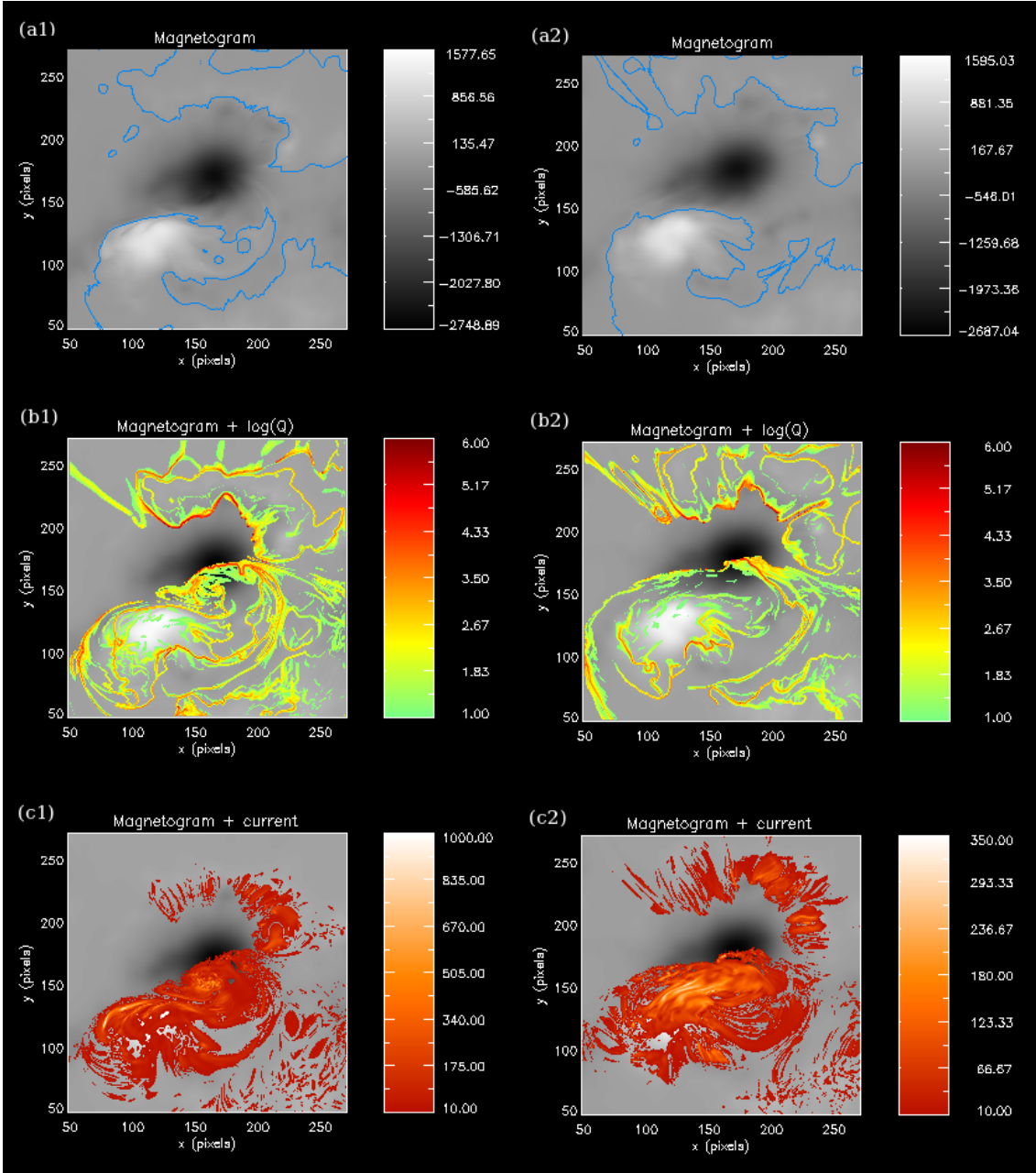


Figure 2.6: These images show, at  $z = 5 \text{ pixel} \simeq 3000 \text{ km}$ , (from the top to the bottom) the vertical magnetic field with the PIL in light blue, the logarithm of the  $Q$ -factor (calculated at  $z = 5 \text{ pixel}$ ) and the current density both over-plotted on the magnetogram (before on the left and after on the right).

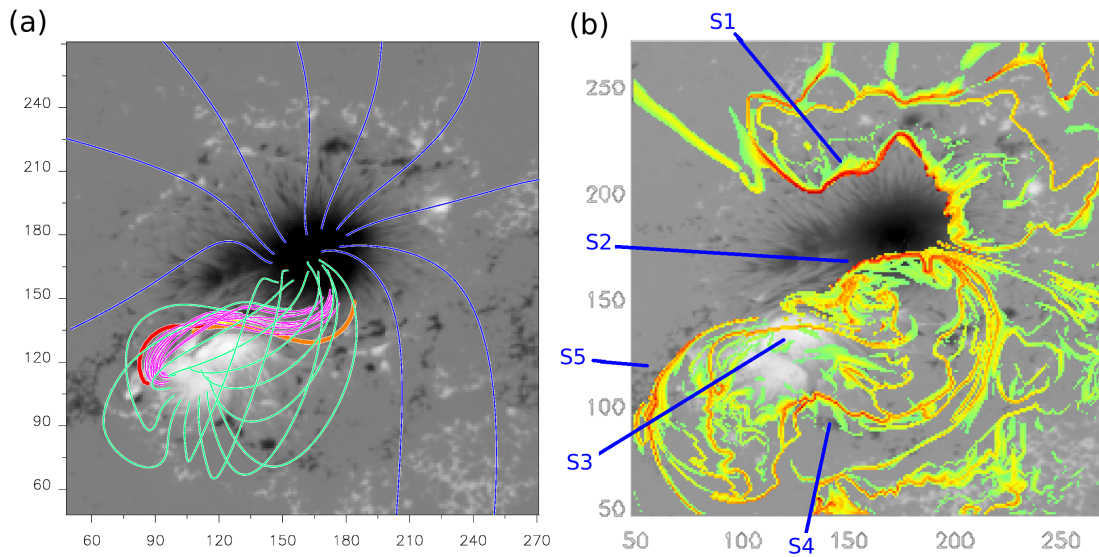


Figure 2.7: On (a) is plotted a selection of field lines between the two polarities. The pink lines are related to the HFT while the green are part of the overlying flux rope. On (b) is plotted the QSL at  $z = 5 \text{ pixel}$  overplotting to the vertical magnetic field at  $z = 0 \text{ pixel}$

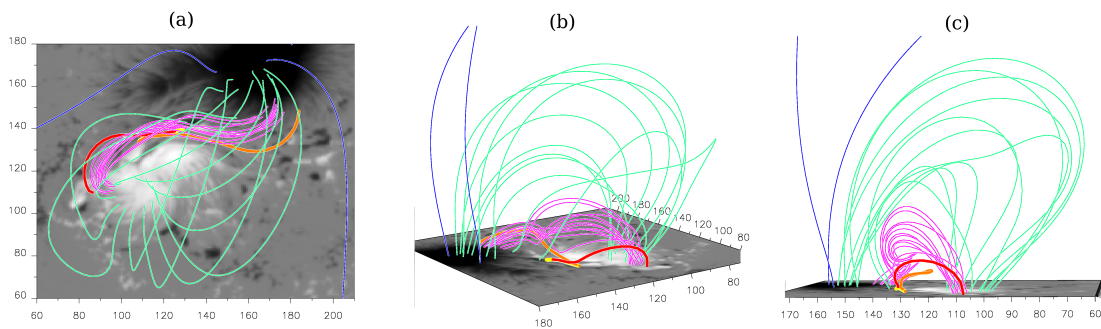


Figure 2.8: A zoom of the field lines discussed above seen, from (a) above, (b) the side viewed from the top-left corner, (c) the side viewed from the left.

(Figures 2.6 b1 and b2) and field lines plots (Figures 2.2 and 2.3). In the second case there is a reduction in complexity, if compared with the first case which is very complex and present various thin high  $Q$  structures. To investigate the geometry of the field in the case before the event in detail (Figures 2.7 and 2.8), we plotted field lines anchored at  $z = 0 \text{ pixel}$  around the PIL between the location of the two polarities where the two parallel ribbons start to be generated (see Figure 2.1). In this region, on  $z = 5 \text{ pixel}$ , we have a main QSLs structures labelled as S3 in Figure 2.7 b. The S3 is related with the centre of the flare and is the S-shape with high- $Q$  value slightly to the north of the positive polarity, following the PIL at the same level (Figure 2.6 a1). We carefully plot field lines around this region. We have found an hyperbolic flux tube (HFT) related to this QSLs feature (S3) which we plotted in pink in Figures 2.7 a and 2.8. This HFT passes above a null point located at  $z = 4 \text{ pixel}$ . Below this null we plotted three field lines: in yellow (small arcade crossing the PIL at  $z = 0 \text{ pixel}$ ), orange and red that can be seen best in Figure 2.8 b. In particular it is presumable that the orange and red field lines reconnect forming the field lines making up the HFT (the pink lines in Figure 2.8) and the short yellow field line. The QSLs in the  $z = 5 \text{ pixels}$  cut are higher than the null in this zone, hence the PIL (Figure 2.6 a1) to the north of the positive polarity denotes the lower windings of the HFT.

Another two important QSLs feature for us, are the one located where the big ribbons start lighting (labelled S2 and S4 in Figure 2.7 b) apart the ones generated by the change between open and closed field lines (labelled S1 in Figure 2.7 b). These are the red high  $Q$ -factor line in the middle of the negative source (S2) and the hook structure on the bottom of the positive polarity (S4). When we plot the field lines around these zones, we have seen that these two QSLs are connected by an overlying flux rope traced with green field lines in Figures 2.7 a and 2.8. To plot this rope we took starting points in  $z = 0 \text{ pixel}$  plane lying on a circle over the positive polarity. These field lines correspond to the two QSL features at  $z = 5 \text{ pixel}$ . This overlying flux rope is weakly twisted due to the spin rotation of the positive sunspot. Extra open field lines from the negative sunspot are plotted in dark blue.

Summarising, the geometry of the magnetic field in the studied case before the event consist of a HFT (pink field lines in Figure 2.7 a and 2.8) overlaid by a flux rope (green field lines in Figure 2.7 a and 2.8). This is the result of the combination of the shear and the spin rotation of the positive polarity. Several distinct computational models exist for such a configuration. A few of them consider only the sheared component such as DeVore and Antiochos (2000) who interpreted the HFT as a low-altitude sheared arcade between the two spots underneath an essentially potential field that is nearly orthogonal to the arcade (green flux rope). Alternatively, Aulanier et al. (2010) and Amari et al. (2003a,b) consider a magnetic field with a pair of spots in which they gave the same spin rotation to both spots, clockwise in the first case and anticlockwise in the others. This rotation resulted in a twisted overlying flux

rope and in both types of imposed movements also lead to a shear at the PIL, since the two spots are close by. The sheared field lines (e.g. orange and red field lines in Figure 2.8) eventually touch each other at a low altitude, in our case around  $z = 4 \text{ pixel}$ , where we have the presence of a null point, and reconnect. This reconnection forms the HFT, which is built up through successive reconnection to form a low altitude rope which is of a smaller scale than the globally rotating field.

As we can see from comparing Figure 2.3 with Figure 2.7, the high current before the flare corresponds to the HFT and it seems mostly located between the HFT and the overlying flux rope. It is generally accepted that there are essentially two possibilities for the origin of the enhanced current density: one is that the current is transported along with the field as it emerges from the convection zone and the other is that it is created by the moving field lines footprints in the photospheric surface which stress the coronal field and create a shell of current around the tube (Low, 1996). It is not easy in our case to distinguish between these.

In the horizontal cut, we can clearly see the presence of the current in the core of the HFT (Figure 2.6 c1). The current shell it is not quite visible because it is too thin. So to better highlight the current sheet around the HFT we plot in Figure 2.9 an artificial quantity  $\alpha^*$  proportional to the inverse of the grid size calculated as

$$\alpha^* = \mathbf{j}/\mathbf{B},$$

that is bigger when the thickness of the current is smaller, independently from the value of the magnetic field.

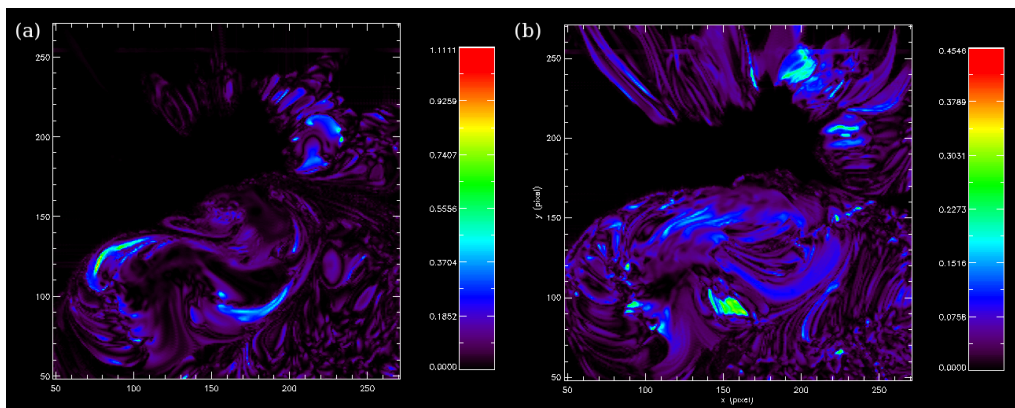


Figure 2.9: Plots of  $\alpha^*$  (the current normalised by the magnetic field) (a) before and (b) after the flare on the horizontal cut at  $z = 5 \text{ pixel}$ .

In Figure 2.9 a we can clearly see the sides of the emerging HFT (high- $\alpha^*$  feature in  $x \sim 100, y \sim 120$  and  $x \sim 170, y \sim 90$ ) that are not present after the flare as shown in Figure 2.9 b, due to the relaxation of the magnetic field during the event.

This current is really important for the study of the pre-erupting configuration. As new flux emerges from the photosphere, it forms a current sheet as it is pressed against field structure that are already present. This is a well known effect schematically illustrated in Figure 2.10. As the current in the sheet grows, it may then reach a critical point and eventually the whole system becomes unstable and the emerging HFT may reconnect with existing flux rope as described by e.g. in Forbes (2000), Isobe et al. (2007). Even though it is now widely accepted that solar eruptions are due to such a violent destabilisation of previously energised coronal magnetic fields, the detailed mechanisms which bring a system to an eruptive stage, and which eventually drive the eruption, are not yet fully understood. When the eruption occurs, the HFT rises and reconnects with the overlying flux rope generating a two-ribbon flare and the energy stored in the stressed magnetic field is converted to other forms of energy leaving a much less complicated geometry of the field.

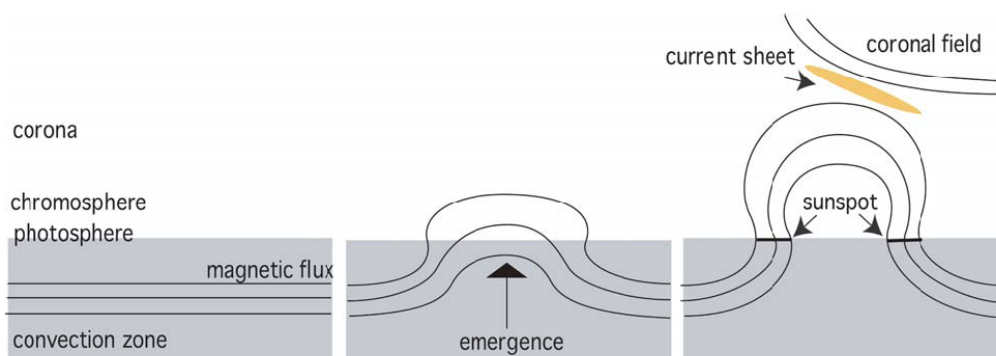


Figure 2.10: Schematic illustration of an emerging flux region. (Figure from Isobe et al., 2007)

In this chapter we have investigated the relation between the QSLs, currents and the geometry of the field lines in two extrapolated magnetic fields to determine before and after a large X-class flare. We have found a good relation between them. In particular the QSL footprints (e.g. features labelled as S2, S4, S5 in Figure 2.7 b) seem to highlight the shape of the current at the same level while some of the high current correspond to features of  $Q$  (e.g. high current in Figure 2.6 c1 with S3 feature of  $Q$  in Figure 2.7 b). Another point that we would like to investigate is the relation between the QSLs and the magnetic topology. Here this comparison has been not possible due to the location of the null points. In fact the ones that we could trust, when not located close to the flare structure, that we were interested in studying. Our next step, therefore, is to analyse a simpler case where the magnetic field is potential and generated by magnetic field point sources which we do in the next chapter.

## Chapter 3

# Comparison of the magnetic skeleton and QSLs in source models

In this chapter (adapted from Restante et al., 2009) we investigate the link between the magnetic skeleton and QSLs using magnetic field configurations that are simple, but still representative of observed flaring regions.

Bridging the gap between the magnetic skeleton and QSLs has been the object of several studies. First, the highest squashing degrees are found within hyperbolic flux tubes (HFTs) and so these features can be thought of as the “core” of a QSL (Titov et al., 2002). A separator (which is at the intersection of two separatrix surfaces) appears to be similar to an infinitely squashed HFT (Démoulin et al., 1996, Titov et al., 2002, Titov et al., 2003, Galsgaard et al., 2003) and the HFT footprints have been mentioned to be located roughly above spine field lines by Titov et al. (2002). Second, in a given magnetic field configuration built from magnetic sources, it has been shown that a transition, from the skeleton to QSLs, takes place when all the sources and related null-points are displaced from the photospheric layer to below it (Démoulin et al., 1996, Titov and Hornig, 2002). The dependence of the maximum value of the squashing degree, with respect to the depth of the sources, has been found to be a power law, the index of which depends on the relative positioning of the sources (Titov and Hornig, 2002). Also, the closer the sources are placed to the photospheric plane, the greater the portions of the skeleton that are covered by the QSL footprints. This is clearly shown in Démoulin et al. (1996) in their Figure 1 which we reproduce here as Figure 3.1. This particular distribution of sources is taken to be our first sources distribution, to better compare our study with literature results. Third, these findings have recently been complemented by the spatial correlation found between QSL footprints and parallel electric fields integrated along reconnecting field lines in an MHD simulation that used a potential field extrapolation as initial conditions. The QSLs have also been compared with parts of the complex skeletons that were calculated in various discrete potential

field flux concentration models for the same observed photospheric magnetic field (Maclean et al., 2008).

Our interest is in the associations between QSLs, magnetic skeletons and flare ribbons. We further pursue the analysis of the link between skeletons and QSLs. We show and explain geometrically which parts of the skeleton of any given magnetic field configuration, built with magnetic sources, can turn into QSLs. Our results therefore can be used to predict which elements of the magnetic field, in source models, can be involved in coronal reconnection, and where flare ribbons can be located in the chromosphere. We use potential field models to conduct this study, therefore our results only apply to particular magnetic field configurations. Riley et al. (2006), in fact, found that potential field sources models produce similar results with the MHD models for configurations based on untwisted coronal field and showed that these models are useful tools for computing the large scale coronal field when time-dependent changes in the photospheric flux can be neglected.

### 3.1 Source models

Models based on source distributions have been often use to model the coronal magnetic field. In particular, in quite a few models the sources have been placed on the photospheric level and are concentrated in a point (i.e. monopoles). The magnetic field generated from these sources is usually potential. The resulting magnetic field will contain photospheric and possibly coronal null points that give the skeleton of the magnetic field. The occurrence of null points, in particular photospheric null points, and coronal separators, is a very natural property of magnetic field configurations which are formed by discrete photospheric flux concentrations (either singular or extended), around which there is no magnetic flux passing through the photosphere (e.g. Gorbachev and Somov, 1989, Démoulin et al., 1994a, Longcope and Klapper, 2002, Schrijver and Title, 2002, Close et al., 2005, Priest et al., 2005b, Maclean et al., 2008). Such models can therefore result in a complex distribution of distinct flux domains, whose boundaries are defined by separatrix fan surfaces. These fans form part of the skeleton of the magnetic field, when combined with their associated photospheric null points and spine field lines (Longcope and Cowley, 1996). Such models have been applied to observations of bright points (e.g. Parnell et al., 1994, Longcope, 2001, Maclean et al., 2008) and flares (Longcope et al., 2005, Barnes et al., 2005, Longcope et al., 2007, Des Jardins et al., 2009). In general, however, the use of discrete sources and the magnetic skeleton has been applied to try and determine not only the number and approximate position of the reconnection sites, but also to determine the energy released during reconnection. This is because, with the magnetic skeleton, it is very easy to determine the amount of flux transferred between flux domains and hence estimates can be made of the

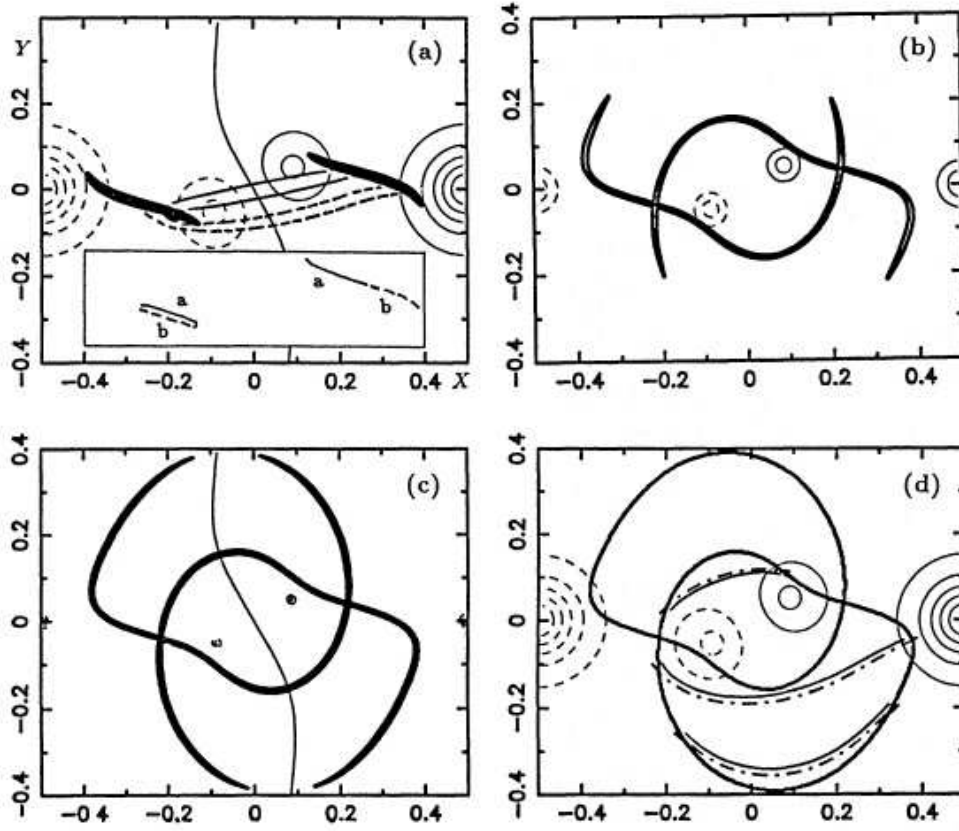


Figure 3.1: This picture shows the relation between the depth of the sources and the extension of the QSL region. In fact, the closer the sources are placed to the photospheric plane, the greater the portion of skeleton covered by the QSL footprints. In this configuration the bipoles are inclined at an angle  $\psi = 30^\circ$  to the  $x$ -axis. The vertical photospheric magnetic field  $B_z$  is shown by equi-spaced isocontours with positive values (solid), negative values (dashed) and the PIL is the elongated thin S-shape continuous line in the middle of the plane in (a) and (c). (a)-(c) show an isocontour of the function  $N$  ( $=5, 10, 10$ , respectively) in the photospheric plane with source depth  $z = 0$ ,  $z = -0.95$ ,  $z = -0.98$  respectively. In (a) some selected field lines are drawn in continuous (dashed) lines to show the particular link existing between the two regions: they start from the upper (lower) border of the left region and reach the lower-left (lower-right) border region. In (d) the intersection of the separatrices with the photospheric plane is given by the thick continuous lines. Figure from Démoulin et al. (1996).

currents generated and then released during these flux changes. In particular, this is the philosophy that led to the development of the minimum current corona model (Longcope, 1996, Longcope and Cowley, 1996, Longcope, 2001), which has been used to model flares to determine where and how much energy is released in such events (e.g. Longcope and Silva, 1998, Barnes et al., 2005, Longcope et al., 2007). Furthermore, Priest et al. (2002) have applied the magnetic skeleton approach to create a coronal model to explain coronal heating. Close et al. (2004, 2005) considered quiet-Sun magnetograms and, using the magnetic skeleton approach based on a potential field connectivity model, were able to determine that during solar minimum all the magnetic connections within the corona are replaced in just 1.4 hrs, a factor of 10 times faster than the recycling time of the magnetic features in the quiet-Sun photosphere (Hagenaar, 2001). When applied to flare observations, clear correlations have been found between the locations of observed chromospheric bright ribbons and of the low altitude trace of the modeled skeletons (e.g. Démoulin et al., 1994a, Longcope et al., 2007, Longcope and Beveridge, 2007, Des Jardins et al., 2009).

One problem of this approach is that, in reality, the Sun’s surface is not composed of large regions where the normal component of the magnetic field to the surface is zero and the magnetic field is distributed in positive and negative regions. This means that, on the Sun itself, there will be far fewer nulls lying exactly on the surface, and hence far fewer separators, than predicted by these models that are anchored at the Sun’s surface.

A better approach is to locate the sources below the photospheric surface as introduced by Seehafer (1986), Gorbachev and Somov (1988) and as we do here in our cases. In this way the magnetic field at the photospheric level is spread in a circular zone. But this does not solve the presence of a large region with weak component of the magnetic field. Thus, an alternative approach, avoiding these unnatural zero normal field regions, is commonly used in which complex photospheric magnetic fields are modeled in terms of a continuous distribution of flux on the base, derived, for instance, from a smoothed magnetogram. The magnetic field in the corona in these cases is reconstructed using a magnetic field extrapolation model (Section 2.2).

## 3.2 Models involving four sources

### 3.2.1 Studied configurations

We analyse the topology and the field line linkage where a potential magnetic field is created from point charges, i.e. monopoles, placed below the photospheric surface. In such source models, in Cartesian geometry,  $(x,y,z)$  where the sources are placed on a  $z = \text{constant}$  plane and so  $z$  refers to the altitude or depth and the magnetic field  $\mathbf{B}$  is singular at the sources.

We can find the magnetic field at any point in space away from the sources using the following equations:

$$B_x(x,y,z) = \sum_{i=1}^n F_i(x - x_i)r_i^{-3}, \quad (3.1)$$

$$B_y(x,y,z) = \sum_{i=1}^n F_i(y - y_i)r_i^{-3}, \quad (3.2)$$

$$B_z(x,y,z) = \sum_{i=1}^n F_i(z - z_i)r_i^{-3}, \quad (3.3)$$

$$r_i = \sqrt{(x - x_i)^2 + (y - y_i)^2 + (z - z_i)^2}, \quad (3.4)$$

where  $n$  is the number of sources,  $F_i$  is the flux of each source  $i$ , and  $(x_i, y_i, z_i)$  is the position of source  $i$ .

The charges themselves, and the field in the region below the photosphere, are artifacts of the modeling and are not intended to represent the true sub-photospheric field. Adjusting the depth of the sources and their flux we can obtain different distributions of the magnetic field on the photosphere. In particular, submerged charge models produce a vertical photospheric field:

$$B_z(x,y,0) = - \sum_{i=1}^n F_i z_i r_i^{-3}. \quad (3.5)$$

By adjusting the parameters of the sources, it is possible to approximate the vertical field observed by a magnetogram. The salient features of such representations are that each charge generates a smooth, circular flux concentration of radius comparable to its depth. The combination of charges produces a non-intermittent photospheric field with smooth PILs separating regions of opposing polarity.

Potential fields are interesting to conduct our study for several reasons. Historically, they have been used to calculate coronal topologies which have been related to flares and other coronal phenomena (Section 3.1). It has been found that this approximation (including the linear force-free one) is often sufficient to model small confined flares and bright points. Physically, it is expected that the overall topology of a quasi force-free (non dynamic) magnetic field configuration should not be very sensitive to non-potential effects if the electric currents are distributed on a scale which is smaller than that of one of the bipoles. Indeed, Aulanier et al. (2005) and Pariat et al. (2009) show that relatively small-scale currents do not change the overall QSL and null-point topology, respectively, whereas Haynes et al. (2007) found the formation of new separators in dynamically moving bipoles embedded in horizontal fields, and Démoulin et al. (1996) and Titov and Démoulin (1999) showed how large-scale twisted fields induce new QSLs and bald patches, respectively. The

present study therefore does not apply to non force-free fields and/or to force-free fields that contain strong and large-scale currents.

We initially consider two configurations which have already been investigated in the literature by (Démoulin et al., 1996, hereafter **D96**) and (Aulanier et al., 2005, hereafter **A05**). We chose these configurations for three main reasons. First, their QSLs have been calculated in the related papers. D96 actually calculated the norm  $N$  (Equation 1.33) at various altitudes above that of the sources, but we calculate here  $Q$  (Equation 1.35) and show that  $N$  and  $Q$  in this case are closely related. Thus D96, brought first insights to the transition between QSLs and magnetic skeleton structures. Second, the features of the D96 and A05 configurations are similar as they are both formed by four sources, which define a smaller bipole of weak flux embedded in a main larger bipole of strong flux. In particular, in D96 at  $z = 0$  the smaller bipole has weaker magnetic fields than the larger one, whereas in A05, due to the different depth of the sources which form the larger bipole, the magnetic fields of the smaller bipole are stronger than that of the larger bipole. Both configurations have the same main bipole, with its axis along  $x$ . In D96, the inner bipole is roughly parallel to the axis of the main bipole (it inclined at an angle  $\psi = 30^\circ$ ), whereas the bipoles are nearly antiparallel in A05 ( $\psi = 150^\circ$ ). Third, A05 is different to most continuous source models, because its two bipoles are placed at different depths, which creates an asymmetry in the model, as well as spine field lines which are inclined in altitude. Table 3.1 summarises the parameters of the sources in both configurations.

Hereafter, the  $z = 0$  plane will be referred to as the “photosphere”, by analogy with past studies in which subphotospheric sources were considered to emulate the observed distribution of the magnetic field in the solar photosphere. So as to compute the photospheric QSL footprints in our two magnetic configurations, the QSL formulae (Equation 1.35) have been coupled with the MPOLE (Longcope, 2004) libraries, which integrate field lines. The coordinates of the endpoints of the field lines are extracted from MPOLE, since they are required to calculate  $Q$  in the  $z = 0$  plane from Equation 1.35. We used a uniform grid in both  $x$  and  $y$  directions with a grid spacing of  $2.77 \times 10^{-3}$ , which is comparable to that used by D96 and A05. The resulting maps of  $Q(z = 0)$  are plotted in Figures 3.2 a and 3.3 a in a domain  $x \in [-0.61, 0.61]$  and  $y \in [-0.41, 0.41]$ .

The calculated QSLs have the same shapes and localisation as reported in D96 and A05. In the D96 configuration, they form two roughly parallel ‘lanes’ of  $Q$  and the maximum of  $Q$ , at  $z = 0$ , is approximately located where the norm of the magnetic field is minimum. Each lane ends in two little curved hooks. In A05, the shape of the QSLs are different to that in D96. Even though the maxima of  $Q$  are still located around the magnetic field minimum regions, the QSL footprints are arc-shaped and each arc points toward the middle of the other. From this finding, one could first state that the QSLs are always located around minimum magnetic

Table 3.1: Parameters of the magnetic configurations with 4 sources.

Polarity	Parameter	D96 ( $\psi = 30^\circ$ )	A05 ( $\psi = 150^\circ$ )
P1	$x_1$	0.5	0.5
	$y_1$	0	0
	$z_1$	-0.1	-0.2
	$F_1$	1	1
N1	$x_2$	-0.5	-0.5
	$y_2$	0	0
	$z_2$	-0.1	-0.2
	$F_2$	-1	-1
P2	$x_3$	0.0866	-0.0866
	$y_3$	0.05	0.05
	$z_3$	-0.1	-0.1
	$F_3$	0.4	0.4
N2	$x_4$	-0.0866	0.0866
	$y_4$	-0.05	-0.05
	$z_4$	-0.1	-0.1
	$F_4$	-0.4	-0.4

field areas. But this is not sufficient to understand their shape, and their direction of elongation.

### 3.2.2 Fan and spine separatrices emanating from the sources

Instead of using MPOLE to calculate and plot the nulls, the fans and the spines in our four-source models, we use the so-called sources method (SM, see Démoulin et al., 1994a,b), which we briefly describe below.

Firstly, in order to find and to characterise null points, the magnetic field is discretised on a mesh. The sign of the 3 magnetic field components is then calculated on the 12 edges of each 3D cell. When the three components of the field are found to reverse at least once along any of the edges of a cell, a Newton-Raphson method is applied to locate precisely the position of the null in three dimensions. The eigenvectors of the null are then calculated using the standard null-point formula Equation 1.17 (see e.g. Lau and Finn, 1990, Parnell et al., 1996).

In our configurations, both with real eigenvalues, two nulls Nu1 and Nu2 are present, and are located in between two sources of the same polarity, as in Molodenskii and Syrovatskii (1977). In D96, the nulls lie on the same plane as that of the sources, i.e. at  $z = -0.1$ , and are all prone nulls (i.e. the spines lie in a horizontal plane), whereas, in A05, the nulls are located at an intermediate altitude between

the sources which are situated at different depths.

Secondly, for each of the nulls, we integrate with a predictor-corrector scheme the spines in both directions following the eigenvector associated with the eigenvalue whose sign is opposite to that of the other two. In D96 the resulting spines have  $B_z = 0$  and are exactly located in the horizontal plane of the sources, whereas they have finite and varying  $B_z$  values in A05. We use the two other eigenvectors to integrate a set of fan field lines. As found by Fukao et al. (1975), in our case, as in all potential fields, the fan plane is perpendicular to the spine.

The nulls, spines and fans are plotted in Figures 3.2 b and 3.3 b for the D96 and A05 configurations, respectively. The calculated separatrices are of the same type as those found before in four-source models involving two pairs of opposite polarity sources (e.g. Greene, 1988, Gorbachev and Somov, 1989): the spines are low-lying and the fans take the shape of domes which intersect at high altitude along a separator line that connects both nulls.

### 3.2.3 Relation between spines and QSL footprints

Comparing Figures 3.2 a and 3.3 a with Figures 3.2 b and 3.3 b one readily sees that not only the largest photospheric  $Q$  areas are located close to the positions of the sub-photospheric null-points, but also that the main orientation of the QSL footprints roughly follows that of the sub-photospheric spines. This relation was first noticed in Titov et al. (2002). The QSL footprints then tend to join two sources of the same polarity, following a path along which  $B_z(z = 0)$  does not change its sign (i.e. not crossing photospheric inversion lines), and with decreasing  $Q$  values as one moves away from the null-points.

Independently of Titov et al. (2002), parts of the spines of real prone nulls have recently been hinted to be associated with QSLs in potential field source models. First, Des Jardins et al. (2009) found that parts of such spines were located close to regions of Hard X-ray footpoint emission as observed by RHESSI on top of EUV ribbons which developed during three eruptive flares. Since flare ribbons have also been found to match very well with QSL footprints in several case studies (e.g. Mandrini et al., 1996, Démoulin et al., 1997, Schmieder et al., 1997, Bagalá et al., 2000, Démoulin, 2007), their results are similar to ours, even though the applicability of potential fields as models for eruptive flares is questionable. Second, Maclean et al. (2008) compared a set of potential source models with several MHD simulations of an observed bright point. They found that some parts of their calculated skeleton (mostly including spines, and also some fans when looking at their figures) roughly matched both the footprints of the strongest regions of the parallel electric field integrated along the field lines and that of the QSLs, both calculated by Büchner (2006).

Still, these previous results have not fully addressed the question of the nature

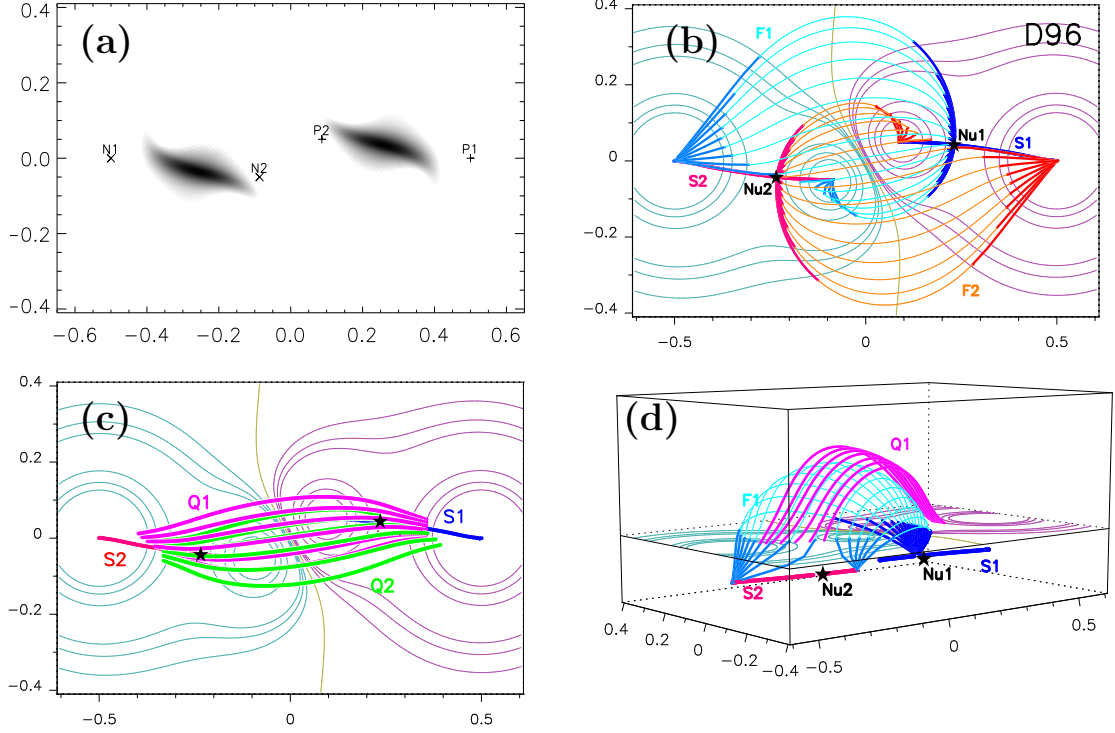


Figure 3.2: Magnetic field topology and geometry for the D96 model. (a) displays a map of the squashing degree  $Q(z=0)$  that shows QSL footprints at  $z=0$ , above the altitude of the sources. White stands for  $\ln Q < 0.6$ . The sources are indicated by  $+$  (resp.  $\times$ ) signs for positive P1,2 (negative N1,2) flux concentrations. (b) shows the same view, but with the null-points Nu1,2 and spine field lines S1,2 at  $z = -0.1$ , as well as some fan field lines F1,2. The latter are drawn thicker along their portions that lie below  $z = 0$ . The pink/cyan/yellow thin contours represent particular positive/negative/zero values of  $Bz(z=0)$ . (c) is the same view as in (a) and (b) and includes the nulls, spines and  $Bz(z=0)$  contours as in (b), but now two sets of QSL field lines (Q1,2) have been overplotted for  $z > 0$  only. The starting points of Q1 (resp. Q2) are located in the positive (resp. negative) magnetic fields at  $z = 0$ , along a short segment that is a cut cross the strong  $Q(z=0)$  along the  $y$  axis. (d) shows a projection view of the configuration, with only one fan F1 and one set of QSL field lines Q1 being drawn above both nulls and spines.

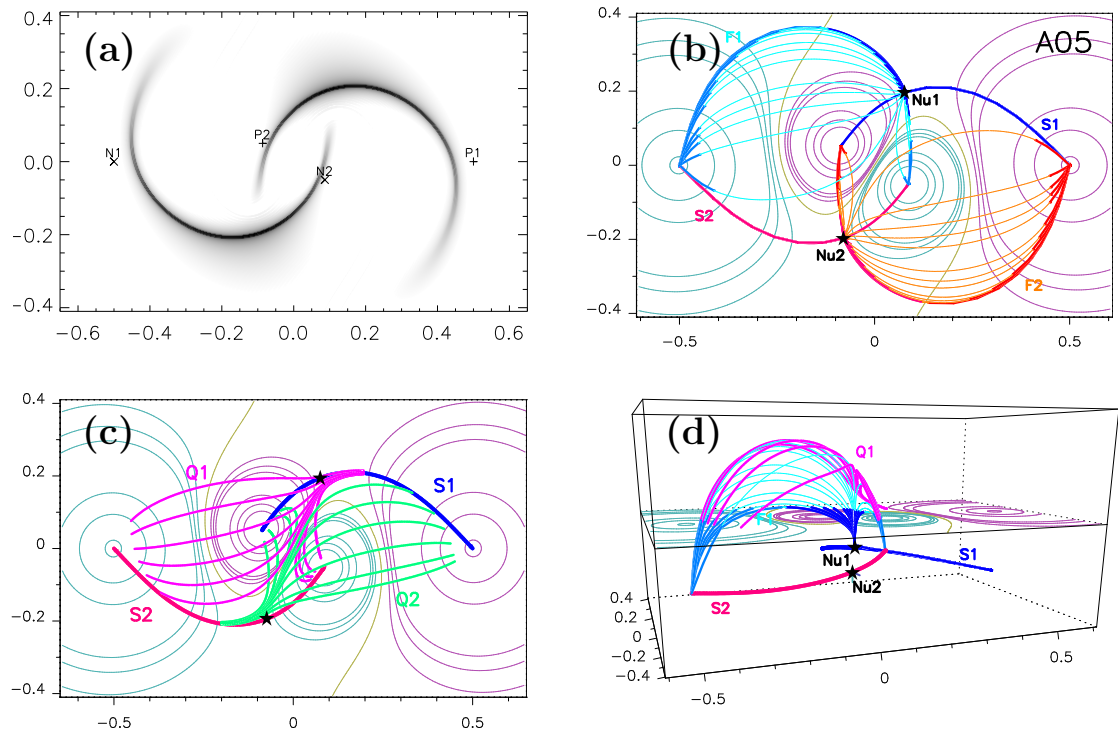


Figure 3.3: Magnetic field topology and geometry for the A05 model. The drawing conventions are the same as in Figure 3.2.

of the transition between elements of the magnetic skeleton and QSLs, and have not addressed the details of the association of spine field lines to QSL footprints. Indeed, Maclean et al. (2008) wrote “the obvious question remaining is, why does only part of the separatrix surface correspond to the location of the strong integrated parallel electric field and the QSL ?”.

Our results clearly show that, when the number of sources is relatively small, the topological transition from the magnetic skeleton to QSLs, which occurs when the nulls pass below the reference photospheric plane, leads to a transformation of the field lines near the nulls that run close to the spine into photospheric QSL footprints. Titov et al. (2002) wrote about the latter that “these are the separatrix lines approaching the nulls perpendicular to the fan surfaces”. This transition can be geometrically explained as follows. If one considers a set of field lines whose starting points are placed in a vertical half-circle of infinitesimal radius that surrounds a nearly horizontal sub-photospheric spine, the field lines will eventually diverge from one another when they approach the null point, and then, they will simply graze the fan surface at large altitudes above the plane of the sources. This same behaviour will occur further and further from the null point, but with less divergence, as one increases the radius of the circle of the field line starting points. All this is a natural property of a potential null-point geometry. This explains why the photospheric maximum of  $Q$  is always located close to the position of the sub-photospheric null-point, the shift only being a natural consequence of the bending of the field lines in response to the flux of the sources. Moreover, by construction, when the reference photospheric plane is placed slightly (resp. far) above the null-point locations, the diverging pattern of the field lines above that plane will be strong (resp. weak), so this explains why the QSL footprints are more (resp. less) extended with stronger (resp. weaker) maximum  $Q$  values, as seen on the Figure 3.2 and Figure 3.3 and the measurements of the  $N$  quantity in D96.

Consequently, a first estimator of a QSL footprint, i.e. a first estimator of the location of flare ribbons and of HXR emissions during reconnection in the solar corona in relatively simple geometries, can simply be given by the distribution of prone nulls and spines in source models.

Still, Figure 3.2 and Figure 3.3 show that the lower  $Q$  extremities of the QSL footprints, namely the hooks in D96 and the arcs in A05, not only pass the location of the sources, but are also much longer than the spines. D96 also clearly showed that, when the depth of the sources is very close to that of the photosphere at which the QSLs are calculated, the QSL footprint eventually covers the intersection of the separatrix surfaces with the photosphere as well. This shows right away that simply associating QSL footprints and spines is only an approximation. Understanding the full nature of the transition between the magnetic skeleton and QSLs therefore requires further investigation. Since it is not straightforward to understand this with our four source models, we address this issue hereafter with a multiple source

model.

### 3.3 Multi sources

#### 3.3.1 Strong spine-related QSLs in complex configurations

Table 3.2: Parameters of the magnetic configuration with 15 sources

Polarity	$x$	$y$	$z$	$F_i$
P1	-0.5	0.1	-0.1	0.8
P2	-0.3	-0.3	-0.1	2.5
P3	-0.2	0.2	-0.1	1.5
P4	-0.0	0.1	-0.1	0.5
P5	0.05	-0.15	-0.1	0.8
P6	0.15	0.4	-0.1	0.7
P7	0.4	-0.2	-0.1	1.5
P8	0.5	0.3	-0.1	3.
N1	-0.5	-0.2	-0.1	-2.
N2	-0.4	0.5	-0.1	-3.
N3	-0.2	-0.1	-0.1	-0.8
N4	-0.1	0.3	-0.1	-0.5
N5	0.1	-0.4	-0.1	-2.5
N6	0.25	-0.1	-0.1	-0.5
N7	0.3	0.15	-0.1	-2.

In this section, we consider a more complex geometry than before. We consider an asymmetric distribution made of 15 balanced sources with different intensities. The source parameters are given in Table 3.2. We consider a set of balanced sources to avoid the presence of artificial sources away from the selected field of view with ( $x = y \in [-1,1]$ ). We chose all sources at the same level  $z = -0.1$  on a square grid with 361 points in each direction in  $x$  and  $y$ . We selected the source parameters in order to have all the nulls lying on the same plane as that of the sources and selected the sources in such way as to avoid the occurrence of any upright nulls. Thus, all the spines lie in the same plane  $z = -0.1$  and there are no vertical spines associated with upright nulls or high altitude null points (as in e.g. Antiochos, 1998, Aulanier et al., 2000, Brown and Priest, 2001, Pariat et al., 2009). The latter would lead to nulls, spines and separatrix surfaces which would be structurally stable (e.g. not turn into QSLs) provided the photospheric plane was not chosen to be above them, as it inevitably is for the surface nulls.

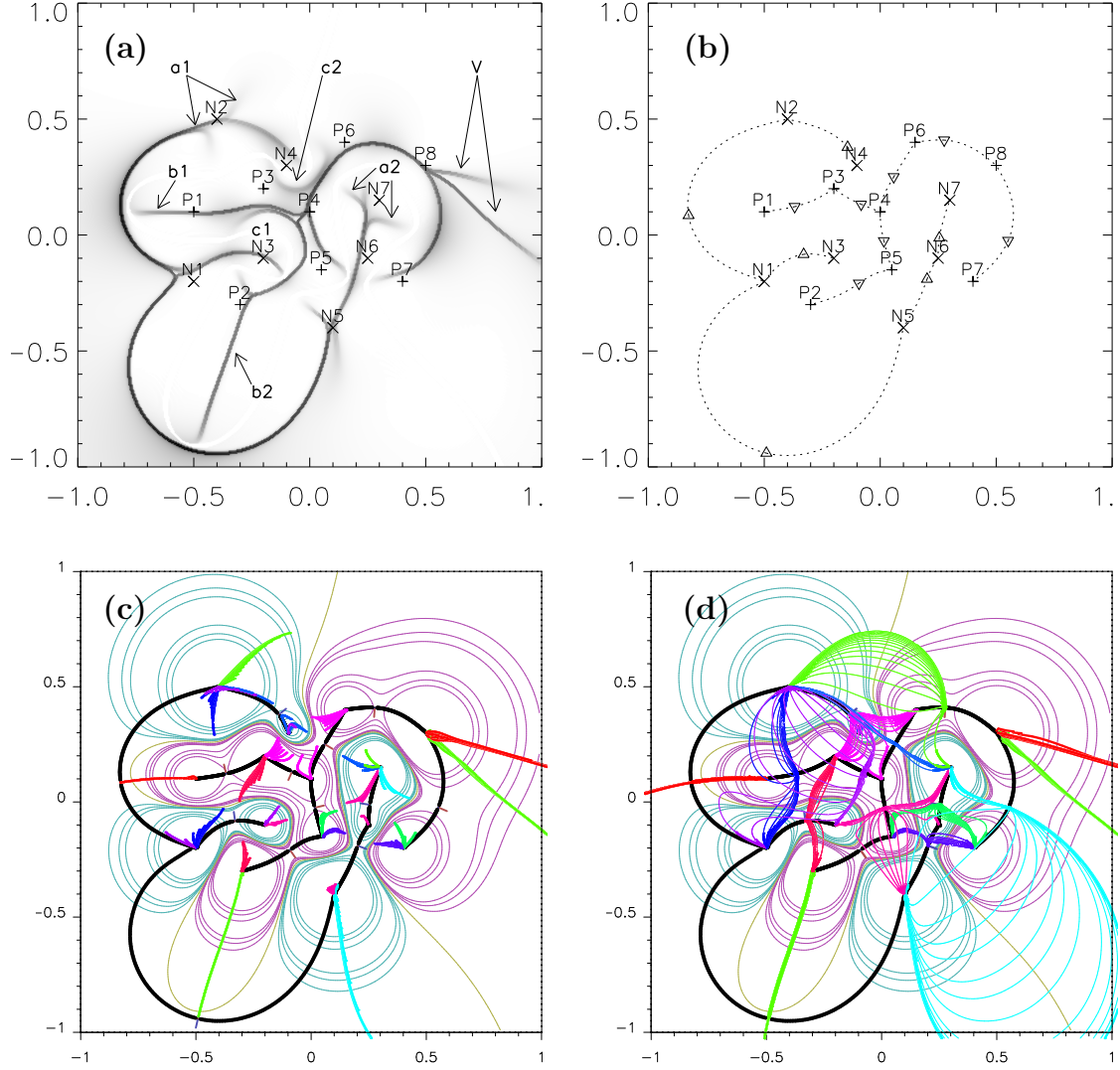


Figure 3.4: Magnetic field topology and geometry for the model with 15 sources. (a) displays a map of the squashing degree  $Q(z=0)$  that shows QSL footprints at  $z=0$ , above the altitude of the sources. The sources are indicated by  $+$  (resp.  $\times$ ) signs for positive (resp. negative) flux concentrations. (b) shows, with the same view, spine field lines with dashed lines, sources with same drawing conventions as in (a), and the null-points all at  $z = -0.1$  as indicated with  $\Delta$  (the negative ones) or  $\nabla$  (the positive ones), calculated with MPOLE. (c) shows the null's spines (black thick lines) calculated with the SM, as well as  $Bz(z=0)$  contours (the inversion lines being drawn in yellow), overplotted by the parts of fans starting from the sources and ending up at  $z=0$  (plotted with thick lines of different colour). (d) is the same as (c), but here the whole fans are plotted.

So as to calculate QSLs footprints (shown in Figure 3.4 a), we used the same method as described in Section 1.4.5. To calculate null points and separatrices, we use both the MPOLE and the SM, as described earlier. MPOLE finds null points using a combination of reasonable initial guesses, and it iterates from them until it finds the locations of the nulls (Longcope, 1996). Both methods gave the same 13 surface nulls, from which we calculated the related skeleton, as plotted in Figures 3.4 b and d.

The resulting skeleton and QSL footprints have a much more complex pattern than in the 4 source models. This enables us to analyse several situations, so as to determine more general rules which govern the topological transitions from the magnetic skeleton to QSLs.

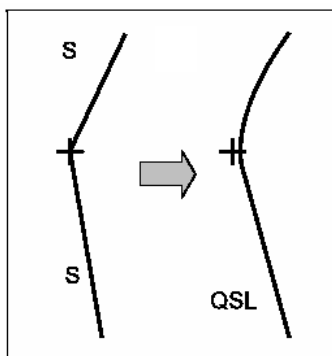


Figure 3.5: This cartoon shows the behaviour of  $Q$  when we have two consecutive spines (S). The QSLs footprint follow their shape, but tend to smooth the point connection between them.

One can see that the strong relation found before between spines and QSL footprints remains valid (Figure 3.4 a-c). Most of the QSL footprints (where  $Q$  takes the higher values) still lie above the spines. Moreover, this configuration reveals that, when two consecutive spines follow each other through a given source, there having a sharp discontinuity in their directions, a continuous corresponding QSL footprint is found above the spines, and it displays a smooth curvature around the position of the source. This behaviour is sketched in Figure 3.5. This situation is found to be very common in our configuration, e.g. between the sources P1-3-4, P4-6-8. Such consecutive spine patterns were also found in the source models of Des Jardins et al. (2009). This transition which we find now clearly explains the relation between several consecutive spines modeled in various source models by Maclean et al. (2008) and the overlying smoother distribution of the footprints of QSLs and of the electric field integrated along the field lines, calculated by Büchner (2006) in a full MHD simulation.

### 3.3.2 Identification of non-spine related QSLs

There are number of regions where the QSL footprints are actually not related to spines. The QSL pattern shown in Figure 3.4 a indeed has more structure than

shown by the spines alone in Figure 3.4 b. Three types of non-spine related QSL footprints can be identified: due to their shapes, we will refer to them as “branches”.

The first significant branches (Figure 3.4 a) are the two very long QSL footprints (b1, b2) which emanate, respectively, from the sources P1 and P2. They cross the positive polarities at  $z = 0$ , as if they were a simple extension of the QSL footprint associated with spines lying in the  $z = -0.1$  plane between P1-3 and P2-5, respectively. The branches extend from the positive sources toward the null points located below on  $z = -0.1$  between N1-2 and N1-5 respectively, but they do not reach them. Instead, they end close to the curved part of the inversion line that closes around the related positive flux concentration at  $z = 0$ . Interestingly, a major difference between these QSL footprints and those associated with spines is that, for the former,  $Q$  peaks at a maximum close to a magnetic source, whereas for the latter  $Q$  is maximum near the null-point. Unlike in the 4 source models, those branches cannot be regarded as minor, because of their relatively large lengths. Also, these are clearly not an artifact of our calculation. Indeed, the U-shape of the inversion lines naturally imply shell-shapes for the distribution of field lines located above  $z = 0$ . In other words, the field lines form a set of arcades above the inversion line, which have the shape of a curve tunnel. At the base of this shell pattern, a gradient of connectivity is naturally expected (as found in magnetic field extrapolations by Mandrini et al., 1996, Schmieder et al., 1997, for an observed bright point and a C-class flare, respectively).

A second type of long branch is rooted in the source P8 (e.g. V in Figure 3.4 a). It has a V-shape. So it is actually composed of two QSLs, which not only merge with one another in a flux concentration, but which also merge with another QSL, that one being associated to the consecutive spines P6-8-7. As found above,  $Q$  in these branches decreases away from the magnetic source, oppositely to what is found in spine-related QSLs. This V-shape QSL pattern is also not an artifact of the calculations, since field line plots show that these two QSLs separate the positive flux concentration at  $z = 0$ , that results from the P8 source, in three quasi connectivity domains, which are linked to the negative flux concentrations associated with N2-1-5.

The third type of branch consists of many small curved QSL footprints (e.g. a1, a2, c1,c2 in Figure 3.4 a), which are located close to almost all other spine-related QSLs. They typically display low  $Q$  values, and they have arc shapes. Some of them have horse-shoe shapes, they graze the spines and partly surround sources (e.g. around N3 (c1) and N4 (c2)). Such QSL footprints have already been reported in Mandrini et al. (1996) and Schmieder et al. (1997). Other arc shaped branches in our model have weaker curvatures, and they simply extend away from the sources (e.g. near N2 (a1) and between N6-7 (a2)). Because of their lengths and shapes, these seem to be of the same kind as the small hook and arc-shaped QSL extensions which we identified in the 4 source models.

### 3.3.3 The role of fan field lines

QSLs have already been found in simple bipolar configurations, in which the corresponding potential fields calculated from point- or line-sources would not possess null points, and therefore no spines. But this has only been reported in highly non-potential fields, in which large-scale shear or twist either creates an S shape bald patch separatrix (Titov and Démoulin, 1999) or a double-J shape QSL footprint pattern (Démoulin et al., 1996, Titov, 2007). But in potential source models, one can hardly imagine how QSLs could not be related to any topological property of the potential magnetic field configuration.

Apart from the spine field lines, the only topological elements in source models are the separatrix (or fan) surfaces. Fan field lines calculated with the SM are plotted in Figure 3.4 d. Note that for most of the fans, we have not plotted field lines covering their whole surface. This is visible, for example in Figure 3.4 d, for the red fan associated with the null point between N1-3, for the dark-blue fan associated with the null point between P4-6, and for two very large-scale red and green fans associated with the null points between N1-2 and N1-5 respectively. The reason is that for most of the null points, the fans are far from being axisymmetric around the axis of the spine, because the complex distribution of sources results in generating fan-related eigenvectors of different amplitudes. For the 4 nulls described above, the ratio between the pair of fan eigenvalues of each null is 3.5, 4.9, 8.1 and 24, respectively. In these cases, fan field lines starting from the null bend in directions parallel or anti-parallel to the eigenvector associated with the largest eigenvalue, as described by Parnell et al. (1996) and found by Mandrini et al. (2006) for photospheric null points and by Masson et al. (2009) for coronal (i.e. high altitude) null points.

The sum of spines and fans (Figure 3.4 d) now show more structures than the QSL footprints (Figure 3.4 a). Still, one can surprisingly associate the V shape and the spine extension branches, with the two red and green fans of very large eigenvalue ratios described above. Those match very well with one another. This fan-branch relation was not expected from the results from our 4 source models, and then could not be predicted with our first explanation of QSL footprint locations on plane above point sources. However, this relation is far from being obvious elsewhere in the model. This shows that, in general, only a subset of the fan field lines can transform into QSL footprints.

On one hand, there is not a single branch that starts from the null points, even though  $Q$  there peaks to large values. On the other hand, only the parts of fans that start from the sources seem relate to branches. To clarify this, we plot in Figure 3.4 c the spines at  $z = -0.1$  as well as the portions of fan field lines only, starting from the sources at  $z = -0.1$  and ending in the photospheric plane at  $z = 0$  (where  $Q$  was calculated). Comparing this with Figure 3.4 a, one can see that these

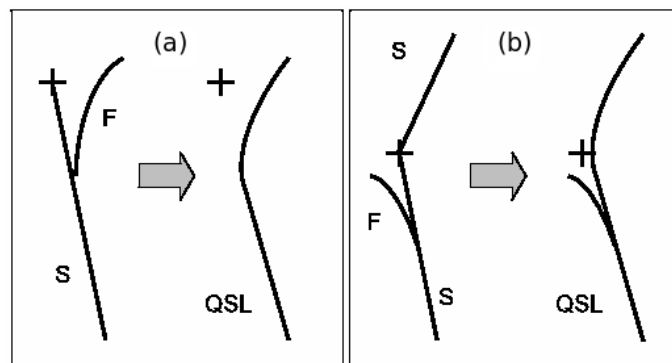


Figure 3.6: This cartoons show the behaviour of  $Q$  when we have a spine (S) and a fan (F). (a) shows  $Q$  factor follows the spine shape (S) until it has a fan contribution (F) that is given by the end points of fan field lines starting from the source (+) on the photospheric plane. In this case it curves on that shape. (c) shows that (a) case is true, but when we have also the presence of a consecutive spine, the  $Q$  factor smoothly follow it and also a branch following the fans contribution.

photospheric ending points all match with the branches. As can be seen, for example, with the fuchsia fan portions that start from the sources P3-4-6, whose photospheric endpoints fit the horse-shoe shape branch that surrounds the source N4. A similar association can be seen around N7, where the spine-related QSL footprint does not end in the source, but rather splits into different branches that correspond to the endpoints of the blue, cyan and green fan field lines. The topological transitions from separatrices to QSLs in these two examples are sketched in Figures 3.6. This finding explains the reason why the long V shape and spine extension branches were readily matched by the drawn red and green fan field lines. Indeed, the very small relative amplitude of the  $z$ -aligned fan eigenvector in these two fans permits a very small amount of magnetic flux to cross the  $z = 0$  plane. So the majority of field lines which we plotted in Figure 3.4 d were actually confined below  $z = 0$ .

The full curve that joins the photospheric endpoints of field lines which belong to a given fan, and which start from a given source, extend from close to this source at  $z = 0$  up to the inversion line at  $z = 0$ . If this whole curve would turn into a QSL footprint in all cases, then all branches should stop just before an inversion line. Figure 3.4 a shows that this indeed happens (see, e.g., the long branches which link the spine-related QSL footprints from P1, P2 and P7), but that it is not the case in general (see e.g. the branches which emanate from N2 and N7). These different behaviours actually relate to the lower limit for  $Q(z = 0)$  for which one considers a QSL to be significantly narrow (i.e. important).

So, qualitatively, our results show that apart from the main spine-related QSL footprints, QSL branches correspond to the curve defined by the photospheric endpoints of all fan field lines which start from a subphotospheric source. This gives us an improved estimator for QSL footprints in source models.

### 3.3.4 Comparison with the 4 source models and interpretation

If one reconsiders the previous simple models which we addressed in this chapter in light of the above findings, one can now relate the hook and arc shape QSL footprints to the branches in the complex 15 source model. Figure 3.2 and Figure 3.3 indeed show an excellent match between the low- $Q$  extensions of the QSLs with the ends at  $z = 0$  of the thick portions of the subphotospheric fan field lines originating from the sources.

As for the transformation of subphotospheric spines into QSL footprints, the topological transition between fan field lines and QSL branches can be understood from the geometry of field lines. Two field lines starting from a subphotospheric source (e.g. P1 in D96) on both sides of a given fan remain roughly parallel along the fan, with weakly varying distances between one another across the fan (which is

formed by red lines in Figure 3.2 b). Close to the null point (Nu2 in Figure 3.2 b) however, these same field lines actually diverge from one another as they tend to follow the spine (S2 in Figure 3.2 d) in opposite directions (towards N1 and N2). As a consequence, the photospheric trace of these field lines, close to the initial source (P1), is smaller than that close to the null point (Nu2). This implies the presence of a relatively strong squashing degree  $Q$ , hence a branch, around the photospheric trace of the fan close to the source. This explains the fan contribution to the QSL footprints.

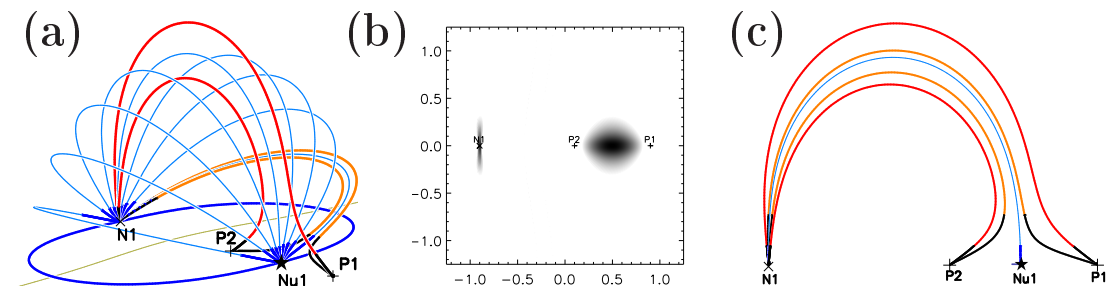


Figure 3.7: Toy model for understanding the nature of the *branches*: (a) in blue we report the fan field lines, in red (in orange) a couple of field line starting from a distance  $\delta$  at the photospheric level above  $N1$  surrounding a vertical (slanting) fan field line, in black we draw the part of these couple of field line below the photospheric level; (b) QSL photospheric footprints; (c) is obtained by rotating the planes on which the pairs of orange and red field lines from (a) on to the same plane.

One can go further and explain the reason why  $Q$  decreases away from the source in these branches. Consider, as a first approximation, that the eigenvectors of the fan have comparable amplitudes, so that the null point structure can be considered to be axisymmetric around the spine axis. In order to have this configuration, we can, for example, generate a minimised model (Figure 3.7) using three balanced sources (two of them being positive) placed along the same line at the same altitude. In this geometry we have only one null having both fan eigenvectors with the same eigenvalue. This implies that in this case we have a radial symmetric fan which simplifies the analysis of the field line geometries. As in our other models, the sources are placed on a plane below the plane taken as the photosphere.

Consider two pairs of field lines, which start from the negative source (N1) and lie either side of the fan surface, which comes from the null point (Nu1) and let each pair be located around a different fan field line: one of them leaving the null at right angles to the plane of sources, and the other inclined at an acute angle to this plane (still allowing the surrounding field lines to pass above the photospheric plane). The two pairs of field lines, drawn in orange and red in Figure 3.7 a, are chosen so as to result in equal distances between their photospheric footprints above N1. Their

subphotospheric portions are drawn in black, so as to visualise their intersections with the photospheric plane. When both pairs reach the photosphere close to the null point, they both diverge along the spine that joins the P1 and P2 sources. In particular, the red pair of field lines diverge there more than the orange pair: the footpoint distance of the orange lines at the vicinity of the null point is smaller than that of the red lines. This implies that on the footprints of the fan field line surrounded by the red pair (resp. the orange pair), close to (resp. far from) the position of the source, the  $Q$ -factor is higher (resp. lower). This fits the QSL footprint which we calculated in this configuration, as shown in Figure 3.7 b.

In order to explain this behaviour and to apply this finding in the general case, we further analyse the way different pairs of field lines intersect a photospheric plane placed above that of the sources. In Figure 3.7, the red and the orange field lines were selected so that the horizontal distance between their pairs of photospheric footprints at the vicinity of the negative source was equal. Due to the symmetry of the configuration, each pair with its middle fan field line lies on the same plane, the one for the red pair being vertical and the one for the orange pair being inclined. For the analysis, let us rotate the plane of the orange lines vertically, so that all field lines now belong to the same plane. Doing this, we keep the length of initial subphotospheric field line segments, drawn in black in Figure 3.7 a. The resulting 2D field line distribution is plotted in Figure 3.7 c. In this projection, the altitude of the photosphere is larger in the orange lines than in the red lines, due to the applied rotation of the plane of the orange lines. Due to the axisymmetric properties of this configuration, this projection readily results in one (blue) fan field line, closely surrounded by the pair of orange lines, themselves being surrounded by the red lines, all along their length. Close to the null point, all field lines that are close to the fan tend to diverge away from it, so as to follow the spine toward the sources P1 and P2. Therefore, for both pairs of field lines, their separation from the fan is smaller (resp. larger) at larger (resp. smaller) altitudes above the null point Nu1. So, in the 2D projection, the distance between the orange lines, at the (higher) altitude of their own photosphere, must be smaller than their distance at the (lower) altitude of the photosphere of the red lines, which is in turn smaller than the distance between the red lines. These geometrical properties show that the ratio between the photospheric footprints above Nu1 and above N1 for the orange lines is smaller than that for the red lines. Hence, the  $Q$ -factor for the red lines must be larger, and must decrease away from the source toward the orange lines.

In other words, the orange pair of field lines, which originate in the  $z = 0$  plane further from the sources, actually lie closer together across the separatrix surface than the red pair. Hence, they remain closer (to the separatrix surface) all the time they are above the photosphere and only diverge as they are near the null below the photosphere. Hence, they have a lower  $Q$ .

This explains why, contrary to spine-related QSL footprints, fan-related branches

display lower and lower  $Q$  further and further away from the sources.

### 3.3.5 Connections between branches and null-halos

In Figure 3.7 b one can see that the QSLs footprint is formed by two distinct patterns. The one located around the source N1 is formed by the branches, and the other one is located around the null point Nu1. The latter is formed by a high- $Q$  core due to the contribution of the underlying spine that connects P1 and P2, as well as by a low- $Q$  halo centred around the null point, which we refer to as the “null-halo” hereafter.

Following the orange pair of field lines in Figure 3.7 a, we can also notice that the footpoints that correspond to the end-part of the branches are linked with the ones that correspond to edge of the null-halo which extends perpendicular to the spine direction. If we consider Figures 3.2 c and 3.3 c we can find the same behaviour. As shown in these Figures, if we take starting footpoints along a segment that crosses the QSL footprint perpendicularly to the spine direction across the null point area, one notices that their conjugate footpoints lie all along the conjugate QSL footprint. The centres of these QSLs have a large  $Q$  corresponding to the spine, but their ends have lower  $Q$  that are branches corresponding to the fan contribution.

As we have already mentioned,  $Q$  has the same value at either end of a field line. Within the null-halo, the field lines rooted in the region that is far from the spine are therefore connected to the branches, whereas those rooted closer to and over the spine are connected to the conjugate spine-related QSL footprint. So the length of the branches seem to be directly related to the width of their related null-halo, perpendicular to the local spine direction. This is also valid in the more complicated case Figure 3.4: comparing the different panels, one can relate each branch with its conjugate null-halo. For example, consider the branches V rooted in the source P8 and their associated parts b1 and b2 (Figure 3.4 a). They are connected to the null-halo around the null points located between the sources N1-N2 and N1-N5 respectively. Also, the upper branch in a1 and the left branch in a2 are connected to the conjugate null-halo between P6-P8. Such associations can be found for each fan shown in Figure 3.4 d, by relating them to branches and null-halos in Figure 3.4 a. All these associations, if we consider the limitations due to the presence of other spine contributions and polarity inversion lines (PIL), suggest that the length of the branches seems to be related to the width of the conjugate null-halo.

It is noteworthy that, in general, the longer the branches, the more they cover the fan projection on the photospheric plane, so the narrower the QSL footprint (as shown by Démoulin et al. (1996) and in Sec 2.4) and the larger the maximum value of  $Q$  (or  $N$ ). Indeed in our models, when one compares the QSLs footprints in the D96 and A05 configurations (Figure 3.2 a and Figure 3.3 a), short (resp. long) branches that are far from (resp. that are almost) fully covering the fan projection

up to the PIL in D96 (resp. in A05), are related to relatively smaller (resp. larger) values of  $Q$  (as clearly seen in the divergence of the coloured Q1 and Q2 field lines in Figures 3.2 c and 3.3 c), hence to a relatively wider (resp. narrower) width of the spine-related QSL footprint. But since we have found that the length of the branches is related to the width of the null-halo, we find the interesting and counter-intuitive result that the narrower the core of the QSL footprint, the wider becomes its null-halo: in practice, when looking at a grey scale rendering for a  $Q$  map, the narrowest part of the QSL is located where the grey scale distribution is the broadest.

### 3.4 Conclusion

In this chapter, we investigated the topological transition between magnetic skeleton and QSL footprints. Our study was motivated by the fact that, despite there being a good relation between the magnetic skeleton and QSLs, so far this relation is not well understood. The QSL footprints match only a part of the skeleton projected on to the photospheric plane (where one can calculate the squashing degree, i.e. the  $Q$ -factor) (Démoulin et al., 1996, Maclean et al., 2008), but the precise relation between them has not yet been investigated. Understanding this relation is important because flare ribbons as observed in  $H\alpha$  as well as in hard X-Rays have been shown to match well with QSL footprints (Démoulin et al., 1996, Démoulin et al., 1997), whereas the ribbons match only part of the skeleton (Démoulin et al., 1994b, Longcope et al., 2007, Des Jardins et al., 2009). Moreover, even if the regions of strong  $Q$ -factor localise better the ribbons, and give a good prediction where current sheets can form when the system is perturbed, in potential source models, the magnetic skeleton is easier to calculate. Indeed, it only requires the location of magnetic null points to be found. This may explain why magnetic skeleton calculations are, currently, more widely used than QSL calculations.

Our goal was two fold. First, we aimed to quantify the topological relation between the topology and the quasi-topology with geometrical arguments. Second, we wanted to find a general method for predicting which parts of the skeleton, calculated with source models, turn into QSL footprints when the photosphere is considered to be located above all magnetic sources, so as to predict the location of current sheets and flare ribbons, in non-eruptive configurations.

We considered three different magnetic field configurations: two relatively simple ones with four sources, already considered in previous studies by Démoulin et al. (1996), Aulanier et al. (2005) to which we refer in this chapter as D96 and A05 respectively, and a more complex one formed by an asymmetric set of 15 sources. In all these models, we calculated the QSL photospheric footprints (the photospheric regions that have the strongest squashing degree), by placing the photosphere at some small altitude above that of the sources, and we compared these regions with

the following components of the calculated skeleton: null points, fan surfaces, and spine field lines.

In the D96 configuration (Figure 3.2) we noticed that the maxima of  $Q$ , the squashing factor, were located near (above) the position of the nulls, and that the shape of the sheet-like distribution formed by the strongest  $Q$  values tends to follow the shape of the spine, but not all of it. This is fully consistent with the QSL plots using  $N$  achieved in D96. When we considered the A05 geometry (Figure 3.3), we found that the QSL footprint was more elongated than the spine projected on the photosphere. In order to understand non-spine related parts of QSL footprints, we investigated a more complex geometry (Figure 3.4), generated by 15 sources located at the same subphotospheric height and chosen such that all the null points were in the same plane as the sources. In this configuration, as in the two previous ones, we found many parts of the QSLs footprint (which we called “*branches*”) that were not due to spine contributions. We found the interesting result that all *branches* actually follow the first intersection with the photosphere of the fan’s field lines starting from subphotospheric sources.

We explained that the topological transition between spines and QSL footprints can be attributed to the divergence of field lines from the spines. Consider, for instance, a positive null from which a separator extends to a negative null. When two field lines lying close to the spine from the positive null, but on different sides of the separatrix surface from the negative null (and vice versa) they cause a large  $Q$ -factor on their foot prints. We also managed to explain the origin of the branches (i.e. non-spine related QSL footprints) as being due to the spreading of the other ends of field lines that make up the narrow high  $Q$  regions that occur above the spines. Naturally these field lines are all above a flux concentration. This spreading can be explained to be less and less important for pairs of field lines anchored further and further from the flux concentration. Since the  $Q$ -factor is constant along field lines, we also explained why some isolated spines (i.e. not related to a separator) can result in a QSL footprint.

With these findings, any one using source and skeleton models should be able to identify which parts of complex skeletons can be related to QSL footprints and (non-eruptive) flare ribbons, by applying the following rules:

- the maxima of the  $Q$ -factor in the photosphere are located near and above the position of the subphotospheric null points;
- the shape of the maximum values of the  $Q$ -factor tend to follow the spine shape (as first noticed by Titov et al., 2002), but not all of it;
- the non-spine related QSL footprints (i.e. *branches*) match with the curves defined by the photospheric endpoints of all fan field lines that start from subphotospheric sources and their conjugate footprints are rooted in the related

null-halo.

So we have found the correlation between magnetic skeleton and quasi-skeleton for a generic photospheric potential point sources distribution, but we would like to generalise this correlation. A different way to simulate an active region on the sun is via a flux emergence simulation. Such simulations have been used extensively over past years to simulate the so called “sigmoids” (S-shape structures) observed with soft X-ray data. In particular, in the next chapter, we are going to investigate two different data set from Archontis et al. (2004b, 2009) and ? without and with overlying magnetic field, respectively.

## Chapter 4

# Investigation of QSLs in 3D MHD simulations of an emerging twisted flux tube

One of the most important processes responsible for many dynamic phenomena observed on the Sun is the emergence of magnetic flux, which occurs on a wide range of scales, forming large active regions or tiny intranetwork ephemeral regions. Large scale emergence can lead to the significant modification of the coronal magnetic field causing increased heating of the corona and often flaring. Although the exact nature of these mechanisms has not yet been completely explained, there exist various numerical experiments of flux emergence from the solar interior into the solar atmosphere. The most common way to reproduce it computationally is to have an initial flux system below the surface that is unstable to small perturbations (usually driven by a density deficit) which then rises through the solar interior and emerges at the surface to form a bipolar system representing an active region or ephemeral region. The mechanism by which this happens is a two-stage process (e.g. Magara, 2001, Archontis et al., 2004a, Murray et al., 2006, Toriumi and Yokoyama, 2010), with both stages relating to buoyancy. In the first stage, as the buoyant flux system rises, the top of the  $\Omega$ -loop structure intersects the photosphere and creates sunspots in bipolar regions but rises no further. In the second part it emerges through the photosphere and chromosphere and expands into the corona where it may interact with other magnetic fields (Figure 2.10). During the first stage, the flux rises through the solar interior due to buoyancy resulting from a lower plasma density. It suffers a gradual deceleration by the time it reaches the photosphere and extends horizontally in the photosphere/chromosphere. Meanwhile, magnetic flux is still transported from below to enhance the magnetic pressure within the flux tube in the photosphere. As the magnetic pressure gradient enhances, the flux becomes locally unstable to a second instability (Parker instability) so that the further

evolution of flux from the tube into the corona occurs (Parker, 1979).

Several experiments have confirmed this “two-step” model. Magara (2001) studied the emergence of the magnetic flux tube from the convection zone by means of 2.5D MHD simulations focused on the cross section of the tube. He found the deceleration of the rising flux tube due to the convectively stable photosphere and the subsequent horizontal outflow. Archontis et al. (2004a) performed 3D simulations to analyse the magnetic buoyancy instability within the photosphere/chromosphere, while Murray et al. (2006) did parameter studies of the dependence of the initial magnetic field strength of the tube and its twist, finding that the tube evolves in a self-similar way when varying the field strength and that the second buoyancy instability does not occur when the field is too weak.

In the literature, there exist a range of different numerical experiments that try to simulate and understand the flux emergence process. One early paper by Shibata et al. (1989a) involved a 2D model in which they introduced the aforementioned Parker instability as a mechanism to allow the flux to emerge. Shibata et al. (1992) considered another 2D model for flux emergence, but their setup included an ambient field in the corona which was antiparallel to the emerging field. Further (2D and 2.5D) models investigated the rise of twisted magnetic flux tubes with translational symmetry of all variables along their axis (e.g. Krall et al., 1998, Magara, 2001). In particular, Krall et al. (1998) found that by including an ambient field oriented vertically the minimum value of twist shown by Moreno-Insertis and Emonet (1996) to be necessary to maintain the integrity of the rising tube could be lowered.

The 3D emergence of a single flux tube or sheet into an initially field-free atmosphere was first studied by Matsumoto and Shibata (1992) who obtained many basic features of the emerging field, such as draining of plasma down the fieldlines, expansion of loops into the corona, and the formation of shock waves at the loop footpoints. However, it was dozen years after this that the first of the modern generation of 3D MHD simulations of the emergence of a twisted magnetic flux tube into the solar atmosphere was published by Fan (2001). She performed an emergence of helical field lines of a twisted flux tube in a stratified atmosphere. In these experiments the axis of the tube remains near the photosphere after emergence. In a similar simulation Magara and Longcope (2001) observed that axial magnetic field may rise well above the photosphere. In both models the original axis of the flux tube never emerges fully into the higher atmosphere because of the very dense material that is trapped in the dipped portions of the twisted magnetic field lines around the original axis. In the literature, various papers suggest similarities between these results and different structures observed on the actual Sun, like sequences of S-shaped loops between active regions observed in X-rays (Matsumoto et al., 1998), photospheric observations of the birth of active regions (Fan, 2001) and X-ray sigmoids (Magara and Longcope, 2001).

3D MHD flux emergence simulations can be divided in two general families: one

with a field-free corona, and the second with a magnetised corona. A number of three-dimensional models (e.g. Fan, 2001, Magara and Longcope, 2003, Manchester et al., 2004, Archontis et al., 2004b) have studied the buoyant rise of a flux tube from the convection zone into a non-magnetised corona. The first model that studied the presence of a coronal magnetic field and the interaction with the emerging flux system was a two-dimensional model by Shibata et al. (1989b). They included a simple horizontal field in the corona and a horizontal magnetic flux sheet below the photosphere to simulate the emerging flux. Then they performed a series of experiments changing the direction of the overlying field (from horizontal to partly vertical) in 2D (Yokoyama and Shibata, 1995) and in 2.5D (Yokoyama and Shibata, 1996). All the configurations result in a current sheet forming over the emerging loops, and the production of magnetic islands and jets via the tearing instability. More recently, (e.g. Fan and Gibson, 2004, Archontis et al., 2004a, Galsgaard et al., 2005, Archontis et al., 2005, Isobe et al., 2005) presented three-dimensional MHD simulations in which an emerging twisted flux tube interacts with a pre-existing coronal magnetic field.

In this chapter, we consider the resulting magnetic structures after the emergence of a twisted flux tube in both of these cases (without and with preexisting ambient magnetic field) from 3D resistive MHD simulations. The first experiment, from Archontis et al. (2004b), involves a flux tube emerging into a non-magnetised corona and, the second, Archontis et al. (2004a), involves the rise of a flux tube into an ambient magnetic field. In particular, we investigate the nature of the QSLs and their connection to current structures and coronal loop structures. We will attempt to compare the current, the  $E_{\parallel}$  integrated along the field lines and the logarithm of the  $Q$ -factor in different horizontal and vertical cuts and for different snapshots of the simulation and try to understand better the relation between them. We also extend, comparing with these quantities, the work done by Maclean et al. (2008) who studied the null points and Parnell et al. (2010) who studied the separators and connectivity of the field lines, both for the case with overlying magnetic field. With these goals we investigate these two different simulations.

## 4.1 Non-magnetised coronal atmosphere

### 4.1.1 Model

The first model that we consider consists of a twisted buoyant magnetic flux tube rising into a field-free atmosphere. The numerical setup for the simulation that we consider has been investigated in different works by Archontis et al. (e.g. 2004b, 2009) (where more precise details can be found). The three-dimensional time-dependent resistive MHD equations are solved numerically on a uniform Cartesian  $(x, y, z)$

grid of resolution (256, 256, 320). The actual physical size of the box is 34 Mm  $\times$  34 Mm  $\times$  27.2 Mm. We use a uniformly spaced coordinate system in the horizontal directions ( $x$  and  $y$ ), but stretched in the vertical direction ( $z$ ) from  $-4.25$  Mm to 22.95 Mm. The initial atmosphere is stratified and its structure is shown in Figure 4.1, where gas pressure, temperature, and density are shown as a function of height.

It is important to notice that all the profiles (and values that we are going to use later on) are normalised according to photospheric values. For the conversion to variables with dimensions, the following values for the units can be used:  $p_{ph} = 1.4 \times 10^5 \text{ erg cm}^{-3}$ ;  $\rho_{ph} = 3 \times 10^{-7} \text{ g cm}^{-3}$ ;  $T_{ph} = 5.6 \times 10^3 \text{ K}$ ;  $H_{ph} = 170 \text{ km}$ . From these values, one obtains a velocity unit,  $V = (p_{ph}/\rho_{ph})^{1/2} = 6.8 \text{ km s}^{-1}$ , a time unit  $t_{ph} = 25 \text{ sec}$  and magnetic field unit  $B_{ph} = 1.3 \times 10^3 \text{ Gauss}$ , chosen so that the Alfvén speed is unity for  $B_{ph}$  and  $\rho_{ph}$ , and the plasma  $\beta$  is 2 for a pressure  $p_{ph}$ . This implies that, for example, to have the real time, we need to multiply the times given by  $t_{ph} = 25 \text{ sec}$ . This is a highly simplified model of the actual solar case, including two isothermal ranges: a cool photosphere and chromosphere ( $T = 6500 \text{ K}$ ) with thickness 1.7 Mm and a hot corona ( $T = 10^6 \text{ K}$ ) with thickness 19.5 Mm. The transition between those layers is made via a steep temperature gradient region that defines our transition region. Below the photosphere the temperature increases gradually with depth.

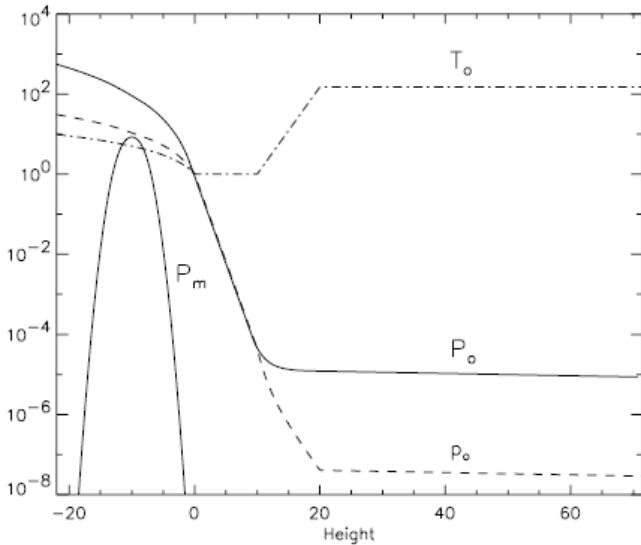


Figure 4.1: Initial distribution of pressure (solid line labelled  $P_0$ ), temperature (dot-dashed line labelled  $T_0$ ), density (dashed line labelled  $\rho_0$ ), and magnetic pressure (solid line labelled  $P_m$ ) along height ( $x = 0$ ,  $y = 0$ ).

In the simulation considered, a horizontal magnetic flux tube with axis lying initially along  $x = 0$  at height  $z = -10$ . The flux tube has uniformly twisted field lines and the initial value of the radius of the tube is  $R = 2.5$  ( $\approx 425 \text{ km}$ ). The axial magnetic field component is given by a simple Gaussian profile. In Figure 4.1

we plot also the magnetic pressure of the initial flux tube. Initially, it is in pressure balance with its surroundings. Then, the tube is made buoyant through a density deficit which peaks toward  $x = y = 0$ . More precisely, the deficit is reduced as one goes from the centre (where the tube temperature equals the external temperature) toward the ends of the tube following a Gaussian profile. The density deficit has its maximum value at the centre, generating the first buoyancy instability. Thus, the tube adopts the shape of an  $\Omega$ -loop as it rises. The buoyant flux tube rises through the lower level of the atmosphere until, at  $t = 30$ , it slows down. The further upward motion of the tube involves lifting overdense plasma against gravity. The density changes with a factor of 14 from  $z = -10$  to the photosphere (Figure 4.1). When the flux tube rises, this causes a marked expansion of the tube when it reach the photospheric plane. Vertical and horizontal expansion rates are different. In fact, it expands faster in the horizontal directions than in the vertical one, since for a vertical expansion extra work must be done against gravity, as anticipated by Spruit and Roberts (1983) and studied in 2.5D by Magara (2001). The latter made a detailed investigation of the expansion processes during emergence. This work was extended into 3D by Magara and Longcope (2001), as we have mentioned before. Due to this expansion, the area covered by magnetic plasma at the photosphere increases with time. Thus, the tube enters an intermediate phase, characterised by a much slower rise of the magnetised plasma through of the photosphere. The further evolution, as we have mentioned, occurs following the onset of the Parker buoyancy instability. The flux tube then continues upwards and emerges into the non-magnetised corona with a so called run-away expansion. After this time the flux has a “mushroom” shape as shown in Figure 4.2.

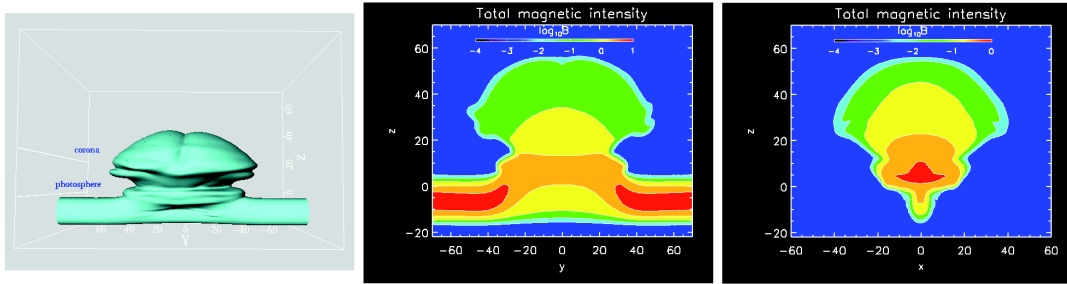


Figure 4.2: 3D isosurface (on the left) and 2D cuts in the  $x = 0$  and  $y = 0$  planes (central and right panels, respectively) of the magnetic strength of the expanding tube at  $t = 70.46$  following the runaway expansion of the flux tube into the corona. The light blue isosurface (resp. contours) corresponds to  $|B| = 10^{-3}$  ( $\max|B| = 2.5$  at this time). Figure taken from Archontis et al. (2004b).

The evolution of the flux passing through the photosphere can be seen from horizontal cuts of the magnetic field at this height. Once the edge of the tube

crosses the photosphere, at  $t = 30$ , the upper part of the rising magnetic system that has reached the photosphere forms a bipolar region (Figure 4.3 top slice). Its orientation at this very early stage of the evolution is perpendicular to the central axis of the tube. This can be seen by comparing the top slice in Figure 4.3 with the bottom slice in Figure 4.3 which shows a lower magnetogram from which one can see the orientation of the flux tube. Later, during emergence, the opposing polarity regions separate and rotate toward a more north-south/axial orientation (Fan, 2001) as in Figure 4.4.

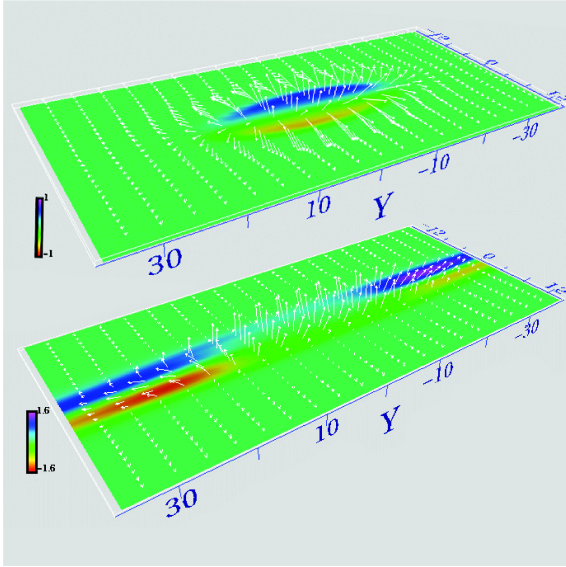


Figure 4.3: Synthetic magnetograms and velocity vector distribution at  $t = 30.4$  on two-dimensional cuts in the  $z = -5$  (convection zone, lower slice) and  $z = 0$  (photosphere, upper slice) planes. Figure from Archontis et al. (2004b).

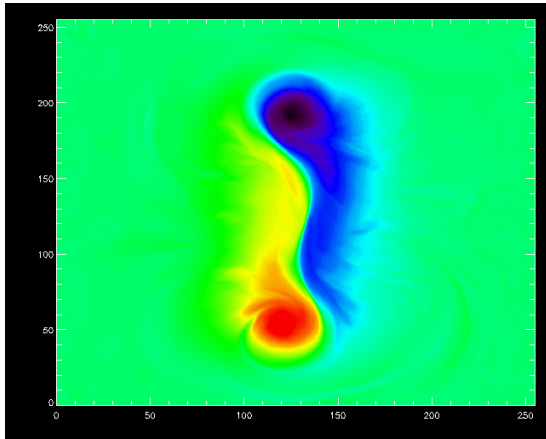


Figure 4.4: Vertical component of the magnetic field on the photosphere ( $z = 20.28$ ) plotted on  $x - y$  axes at  $t = 168$ .

### 4.1.2 Comparison between current and $Q$ -factor

In this section, we follow the evolution of the current density and the  $Q$ -factor during the dynamical emergence of the field. In a first part we are going to summarise the study already conducted in the literature. In this study the first part of the evolution (up to  $t = 120$ ) has been investigated and understood. Our goal in the second part of this section is to try to understand the evolution of the latest phase (e.g.  $t = 140$ ,  $t = 168$ ), calculate the QSL foot prints in the model and investigate its evolution in relation to the formation of the current structures inside the flux system.

#### First part of the evolution

As noticed by Archontis et al. (2009), in the first part of the evolution, the structure of the emerging flux tube is similar to the one produced in the model by Titov and Démoulin (1999), from which we have taken Figure 4.5. The magnetic field model studied in Titov and Démoulin (1999) involved a force-free circular twisted flux tube with an arch-like shape, that rises quasi-statically into an external arched potential magnetic field generated by a pair of magnetic charges with equal strength, but with opposite polarity, positioned below the photosphere perpendicularly to the axis of the flux tube. Titov and Démoulin (1999) point out the importance of the bald patches (BPs) to define separatrix surfaces where there are no null points. As we have mentioned in previous chapters, separatrices have been found to be key locations for current sheet formation during a quasi-static evolution driven by slow photospheric flows of plasma (e.g. Aly, 1990, Lau and Finn, 1993). Titov and Démoulin (1999) studied the evolution of the BPs during the emergence in their model. As the flux tube emerged, a BP first appeared near the apex of the tube. It then grew in size before bifurcating just under the tube apex. As the tube continued to rise, the BPs started to shrink and finally disappeared as soon as the flux tube protruded far enough into corona. The bifurcation of the BP leads to an appearance of a generalised separator line (BP-BP line) as a result of the intersection of the two separatrix surfaces which extend from the two different bifurcated parts of the BP as shown in Figure 4.5. This geometry of the field lines can be seen in the simulation we consider here. To highlight the similarities between our magnetic field configuration at the photosphere and that found by Titov and Démoulin (1999), Archontis et al. (2009) plotted the field lines starting from the bifurcated BPs they found in the photospheric plane of their model in Figure 4.6. In this figure we can also see the current density profile. In this time,  $t = 120$ , its shape is a simple double-J, that becomes more complex later in time (see Figure 4.7).

As shown in Archontis et al. (2009), during the early evolution of the system, the current density is smaller at the middle of the inversion line and larger at the elbows as shown in Figure 4.6. However, as time goes on the current is enhanced in the

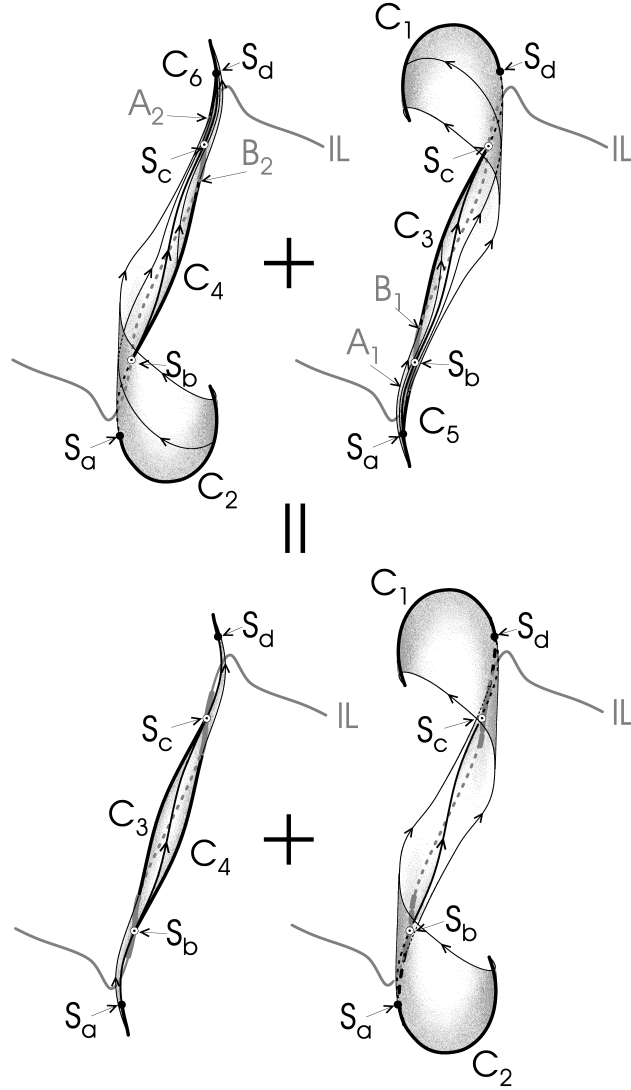


Figure 4.5: Dual representation of the geometrical skeleton of the twisted configuration generated from Bald Patches (BPs). On the top we can see this skeleton as a generation of two distinct separatrices formed by the field lines starting from different BPs: BP1 on the right, located between A1 and B1 and BP2 on the left, located between A2 and B2 along the PIL traced with dashed grey line. On the bottom we can see the same skeleton as a union of the upper (on the right) and lower (on the left) surfaces originating from the corresponding photospheric traces of the field lines. The central arc  $S_a$ - $S_b$  determines the “BP-BP line” along which these separatrix surfaces intersect. Figure from Titov and Démoulin (1999).

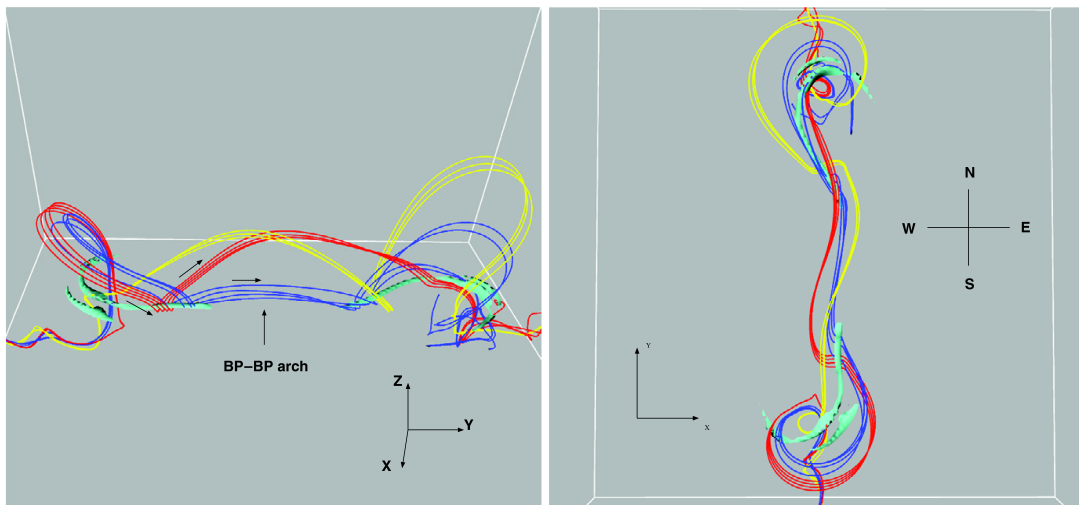


Figure 4.6: Field lines at  $t = 120$ . The green isosurface represents high values of current density at the base of the photosphere. The red, blue and yellow field lines identify different field line groups associated with the double-J BP structure analogous to that found by Titov and Démoulin (1999). Figures from Archontis et al. (2009).

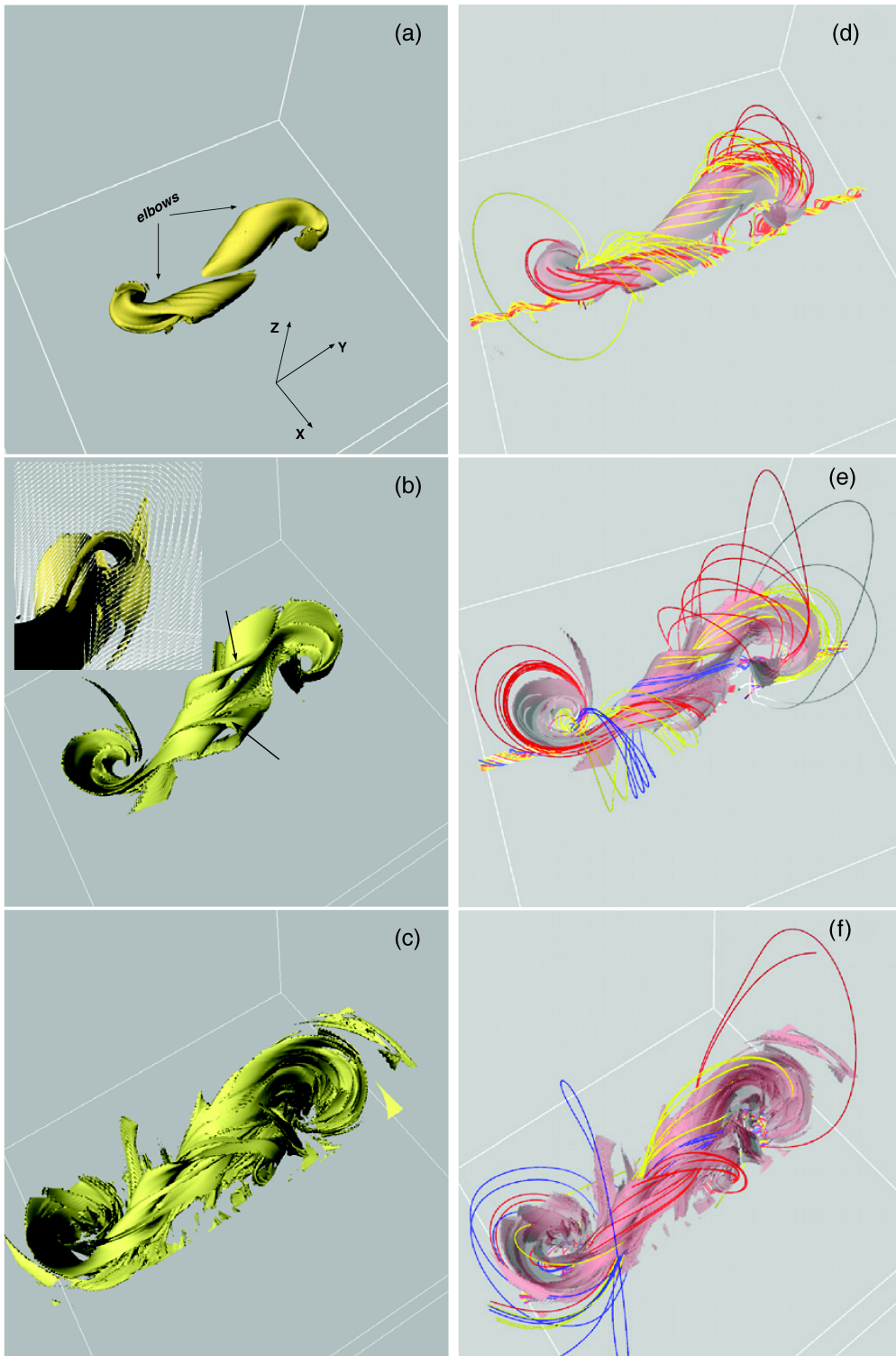


Figure 4.7: High current density isosurfaces (in yellow on the left and transparent pink on the right) illustrating the evolution of the sigmoidal structure. Times are  $t = 120$ ,  $t = 140$ , and  $t = 184$  for the upper, middle, and lower row, respectively. The field lines, which are shown in the right column, are the selected field lines traced from various regions along the isosurfaces. The little inset in panel (b) shows that some of the isosurfaces accompany the rising flux tubes. Figure from Archontis et al. (2009).

central region and the distribution of the current density inside the three-dimensional expanding volume becomes increasingly complex. As we can see in Figure 4.7, the current volume evolves from a classical double J-shape at  $t = 120$  to an S-shaped sigmoid at  $t = 140$ , which becomes more and more fragmented at  $t = 184$ . As we have already seen the magnetic structure during the first part has been equated by Archontis et al. (2009) to the magnetic evolution found by Titov and Démoulin (1999), but the second part of the magnetic evolution is more complex and is not understood. Thus we will concentrate our attention on these later snapshots.

### Second part of the evolution

To investigate this second part of the evolution, we choose two snapshots from the simulation by Archontis et al. (2009), at times  $t = 168$  and  $t = 184$ . Figure 4.8 shows the current and Figure 4.9 the  $Q$ -factor calculated from the plotted level, in horizontal planes at different heights in these two different snapshots. In particular, we show a cut through the high transition region ( $z = 15.28$ ) in Figures 4.8 a-b and Figures 4.9 a-b, a cut in the low corona ( $z = 25.28$ ) in Figures 4.8 c-d and Figures 4.9 c-d, medium corona ( $z = 35.28$ ) in Figures 4.8 f-e, and Figures 4.9 f-e and high ( $z = 45.28$ ) corona in Figures 4.8 g-h and Figures 4.9 g-h. In the QSL footprint there are large regions of dark blue (low  $Q$ ), especially in the transition region cut. The majority of the field lines relating to these regions are “open”. They start in the plane plotted, but leave the box through the side.

Comparing the current and  $Q$ -factor plots, one can see at first glance a general correspondence of the shape of the QSLs and the current but also regions where they do not match. All of them, have generally an elongated S-shape along the flux tube axis going from north to south in the figures and other fragmented features. The main difference is on the north and south sides of the emerging flux tube. Here the current is really low, but the  $Q$ -factor is high due to a change from “closed” field line (that start and end on the level) to “open” field line (that start from the level, but leave the box through a side). These can clearly be seen on the transition region cut (Figures 4.8 a-b and Figures 4.9 a-b). In the  $Q$ -factor at this level, on the right and left at the border of the “closed” and “open” fields there are locations of high  $Q$ , which correspond to locations of really low current. Similarly, at the north and the south at  $z = 25.28$ , high QSL footprints and low current regions are seen for the same reason. Along the main elongate-S structure, their maxima in current and  $Q$ -factor do not correspond exactly, but we need further investigation of the 3D geometry of the field lines to explain this. Concentrating our attention on the first snapshot ( $t = 168$ ) we see that at  $z = 25.28$  the central local maxima of  $Q$  is slightly to the south of the current maxima and the same occurs in the  $z = 45.28$  cut, while at  $z = 35.38$  the central local  $Q$  maxima is closer to the central local maxima of the current. Furthermore, the general fragmented structures in  $Q$  and current in these

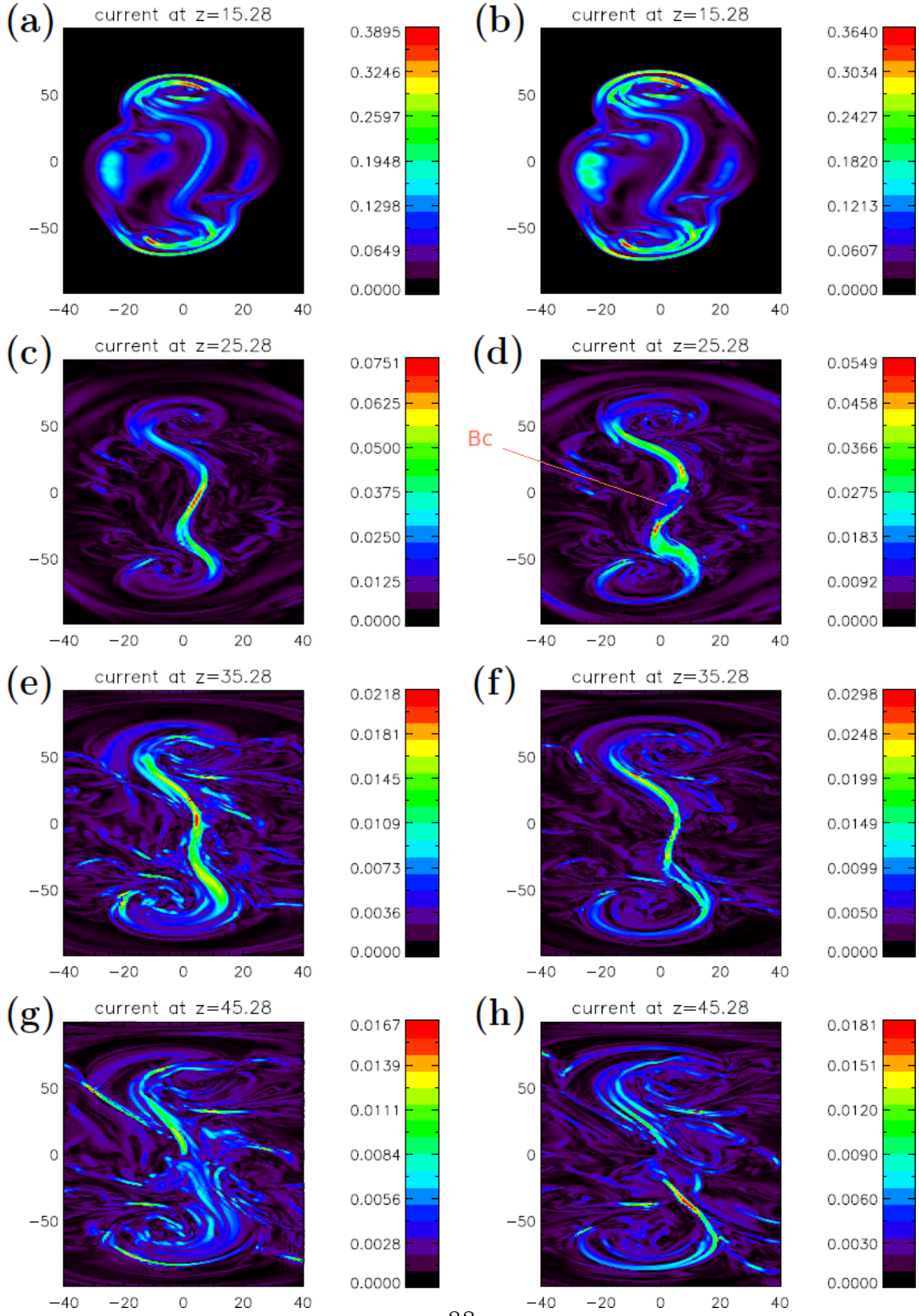


Figure 4.8: Contour plots of current in different  $z$  levels at  $t = 168$  (left column) and  $t = 184$  (right column).

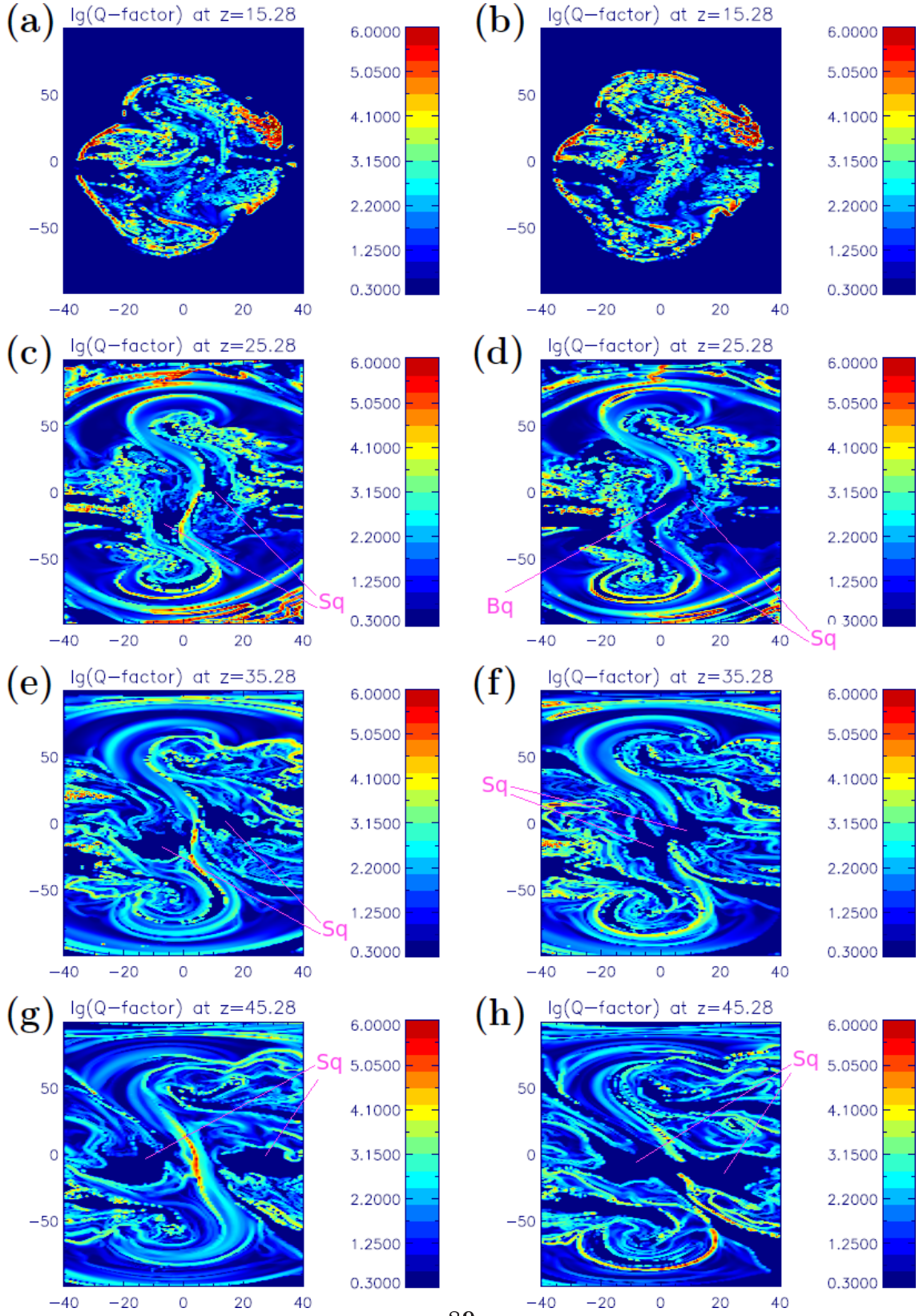


Figure 4.9: Contour plots of the  $Q$ -factor calculated from different  $z$  levels at  $t = 168$  (left column) and  $t = 184$  (right column).

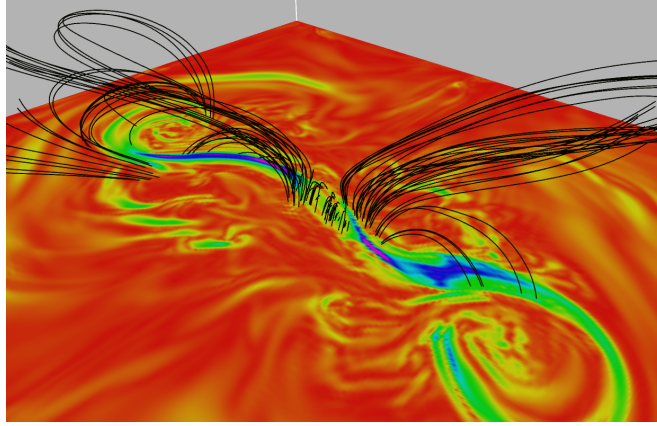
levels around the main S-shaped structure show a similar behaviour. The same sort of correspondence is seen in  $t = 184$ .

When we compare the two snapshots, we can see more or less the same shape in the transition region. The main difference between  $t = 168$  and  $t = 184$  occurs on level  $z = 25.28$  where the S-shape in both the current and the  $Q$ -factor of the former, become a double-J shape once again in the latter. This new double-J ensues for a different reason than that for the first double-J shape we explained before. In earlier snapshots, this was due to the emerging of the flux rope starting from the elbows, as explained by Archontis et al. (2009), and later involving the central part transforming the shape from double-J to S-shape. At  $t = 184$  the new double-J shape does not involve the highest part of the emerging flux rope, as at  $t = 120$ , but just the low corona. In fact this is due to the expansion and change of connectivity of field lines inside the flux rope during the rise that creates the bubble indicated as Bc in the current plot on Figure 4.8 d and Bq in the QSL plot on Figure 4.9 d. This new feature (Bq) is due to the change of geometry of the field lines. The field lines responsible for this bubble are plotted in black in Figure 4.10 overlotted on the current at  $z = 25.28$ . As one can see these field lines correspond to the generation of a lower arcade producing the bobble shape seen in both the  $Q$ -factor (Bq in Figure 4.9 d) and the current (Bc in Figure 4.8 d). These field lines are the result of a change of connectivity of other field lines. To better visualise this, we can look at an earlier time in Figure 4.11. The black field line in Figure 4.10, can be associated with the lower green field lines. It is possible to explain the creation of these twisted field lines as follows: reconnection between the white and yellow field lines, would generate the light blue and the low green lines. The blue field lines form an S-tube inside the over structure that corresponds to the so called “eruption flux rope” (Archontis and Török, 2008).

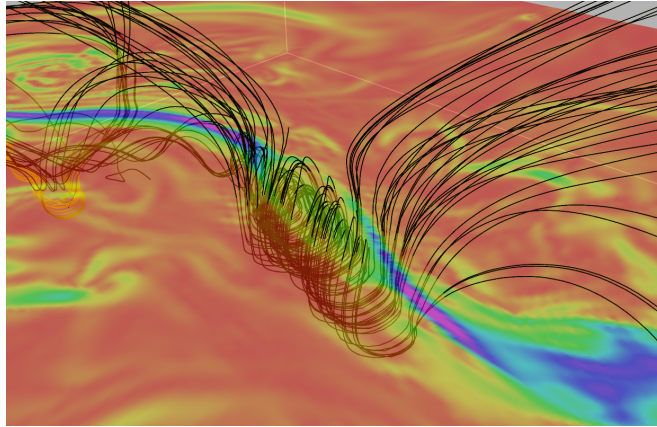
In the higher altitudes ( $z = 35.28$  and  $z = 45.28$ ) are difficult to compare due to their highly fragmented structure (see Figures 4.8 e-f-g-h and Figures 4.9 e-f-g-h). Nevertheless in these highs one can notice in the  $Q$ -factor plots a change between an S-shape to a double-J. The breaking of the S-shape at these higher altitude is due to open field lines. The two regions of open field lines on the side of the central part of the elongated S indicated as Sq in Figure 4.9 e-g at  $t = 168$  merge together in Figure 4.9 f-h at  $t = 184$ . At lower height,  $z = 25.28$ , the same feature (small dark blue Sq on north-east and south-west of the central local maximum of  $Q$ ) becomes smaller in time pushed by the appearance of the central blue bubble Bq described before.

The field lines during the emergence, change their geometry continuously. The internal structure of the rope changes with them, leading Archontis et al. (2004b) to suggest that internal reconnection was occurring. They claim that this internal reconnection gives the fragmentation of the current sigmoid structure. This is the

same behaviour that we notice in Chapter 2. The new lower arcade could be associated with the yellow field lines on Figure 2.8 and the field lines along the central part of the rising flux rope, with the pink line in Figure 2.8 representing the HFT rising during the flare event on December 2006.



(a) Overview.



(b) Zoom with semitransparent current horizontal cut.

Figure 4.10: Contours of the current at  $z = 25.28$  overlaid with some “reconnected” field lines at  $t = 184$ .

In conclusion, at first glance there seem to be a reasonable relation between the location of the current and the QSLs but unfortunately when we look carefully, there is not a one to one match. Some of the  $Q$  structures can be explained but a more detailed investigation following carefully the evolution of the field is required before a full explanation can be reached.

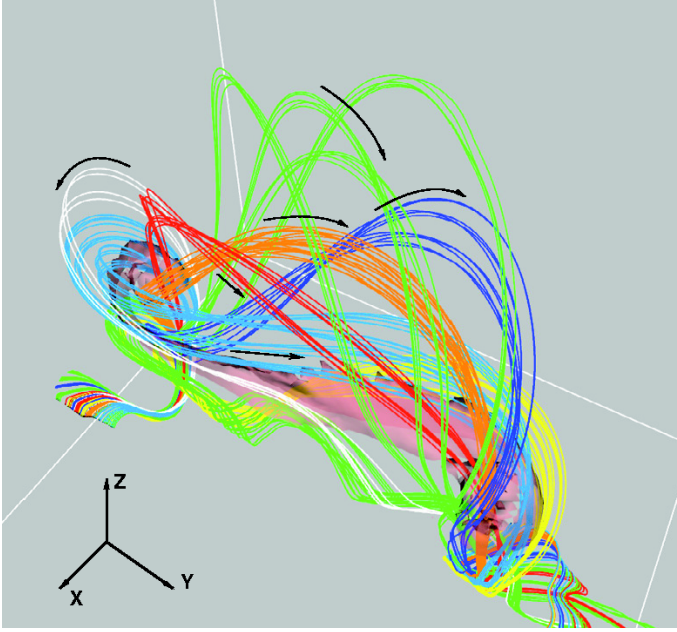


Figure 4.11: Flux rope field lines at  $t = 140$ . The arrows show the direction of the magnetic field. The pink isosurface represents the sigmoidal current layer below the rope. Figure from Archontis and Török (2008).

## 4.2 Magnetised coronal atmosphere

In the previous study we analysed the behaviour of QSL footprints during the emergence of a flux rope into a non-magnetised ambient atmosphere. Here we again investigate the emergence of a flux rope, but we now consider a more realistic simulation, which includes a pre-existing magnetic field in the upper atmosphere. In particular here we consider the nature of the  $Q$ -factor compared to the sites of reconnection identified by plots of the parallel electric field integrated along the field lines ( $\int E_{\parallel} dl$ ) and currents.

The 3D numerical MHD experiment of flux emergence into an overlying horizontal coronal magnetic field that we investigate was first considered by Archontis et al. (2004a) and extended by Archontis et al. (2005), Galsgaard et al. (2005, 2007). Maclean et al. (2008) found the null points and followed their evolution during the emergence and Parnell et al. (2010) investigated the behaviour of the topology and connectivity of the magnetic field in this experiment. The set up of the experiment is essentially the same as that for the non-magnetised case except an overlying coronal horizontal field, inclined at an angle of  $135^\circ$  to the axis of the flux tube, is included in the corona. In particular, an equivalent background stratification to the one used in the non-magnetised case is included, but with slightly different equations (see Archontis et al., 2004a, for details).

Again, all the parameters are normalised with respect to the photospheric values (see preceding section). This flux emergence experiment has 220 time frames,

covering 62 minutes in time. In this simulation a stretched grid in all three directions is used with the highest resolution in the base of the box (along  $z$ ) and in the centre of the domain for the horizontal component ( $x$  and  $y$ ). A grid of  $148 \times 160 \times 218$  points is used distributed in the following dimensionless domain in  $x, y, z : (-60,60) \times (-70,70) \times (-20,82)$ . This domain corresponds to a real size for the whole box of  $23.8\text{Mm} \times 20.4\text{Mm} \times 15.6\text{Mm}$ . The side boundaries of the box are periodic, while the top and the bottom boundaries are closed. As in the previous case, a twisted magnetic flux tube is placed initially in the convection zone with its axis lying at  $z = -10$  along  $x = 0$ . As already explained the main difference between this and the first experiment is the preexisting horizontal uniform magnetic field inclined with respect to the flux tube with a polar angle of  $\phi_0 = 135$ .

The general evolution of the system has been described in detail by Galsgaard et al. (2007), with different orientations of the plane-parallel coronal field relative to the emerging flux tube. They also investigated the current sheet formed between the emerging tube and coronal magnetic field depending on the orientation of the overlying magnetic field.

The initial phase of the emergence of the tube is very similar to that in the non-magnetised case. In fact the introduction of an ambient coronal magnetic field has a negligible effect on the rise of the tube across the layers below the transition region (Figure 4.12). At the beginning ( $t = 20$ ), a relatively small bipole forms (see also Figure 4.12) in the photosphere ( $z = 22.48$ ) that spreads and rotates in time. The bipole starts practically perpendicular to the flux tube axis, due to the strong twist of the field lines around tube. The bipole elongates/rotates along the tube axis during the simulation resulting in a north-south orientation (along  $x = 0$ ) as shown in Figure 4.13 and Figure 4.14. In fact, if we look at horizontal slices of the magnetic field in time at different heights in the domain (Figure 4.13), we see a similar behaviour to that in the case with non-magnetised corona. The rather strong buoyancy given to the central section of the flux tube initially makes it rise toward the photosphere, and after the second instability that allow the tube rises the tube adopts a classical  $\Omega$ -loop shape (Figure 4.14). As shown in Galsgaard et al. (2007), during the rising, the overlying coronal magnetic field is constantly removed by the reconnection process. Thus, the magnetic flux above the rising tube is decreased and the buoyant system can make its way up into the upper atmosphere as illustrated in Figure 4.12.

Our goal is to determine the relation between the geometrical features associated with the QSLs with the current, sites of reconnection and to topological features. As we have mentioned, a good analysis of the evolution of the null points for this case has been published by Maclean et al. (2008). From this paper we know that the emerging flux tube begins to interact with the overlying field around  $t \simeq 20$  when there is the appearance of the first null points. Once the first nulls have appeared, more follow, and there are null points present in every frame from then

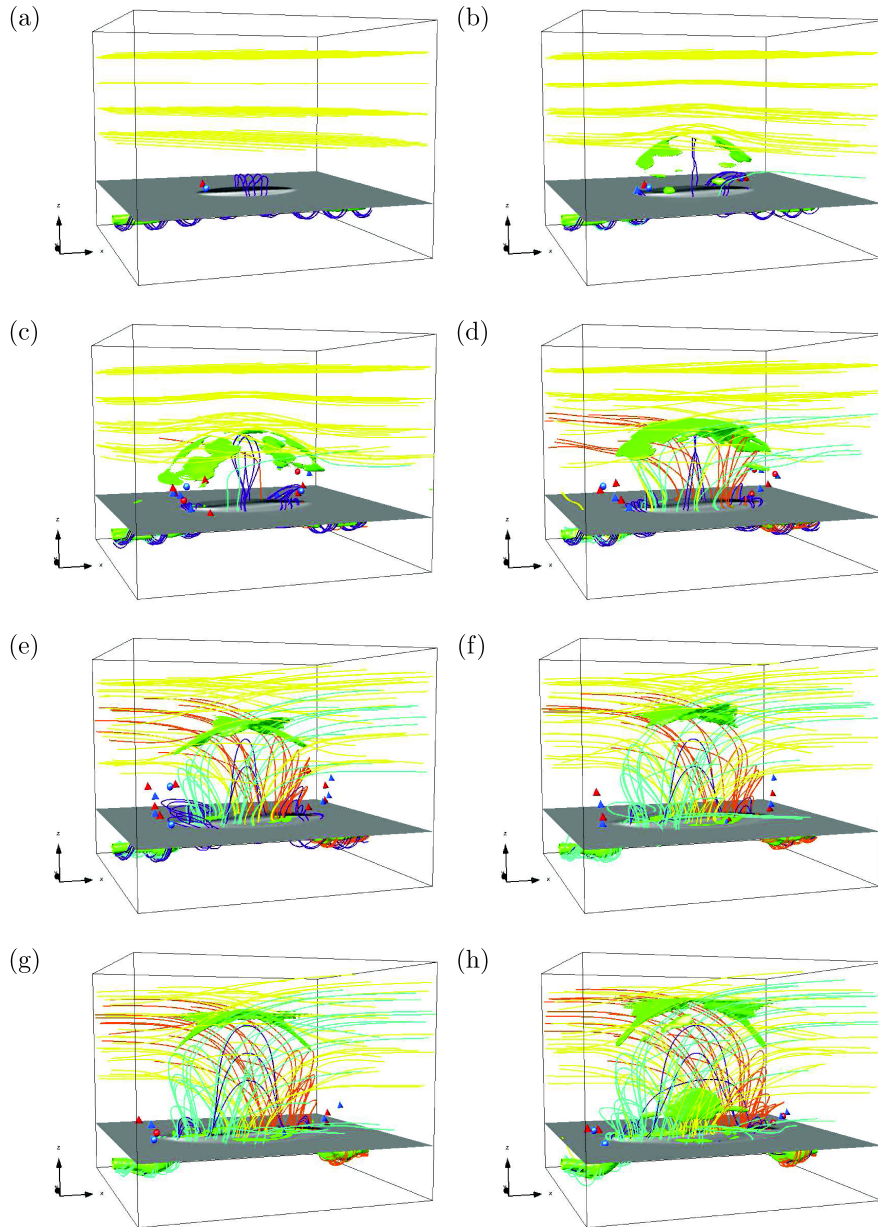
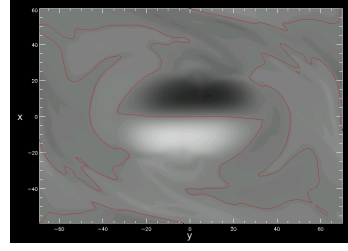
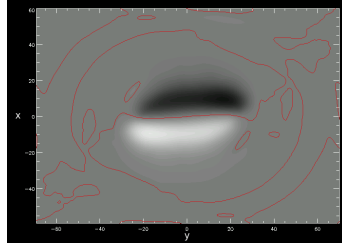
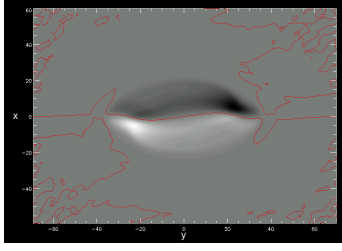
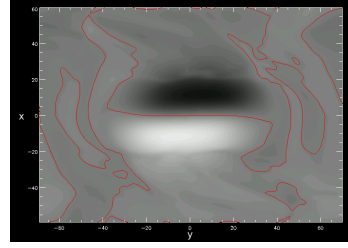
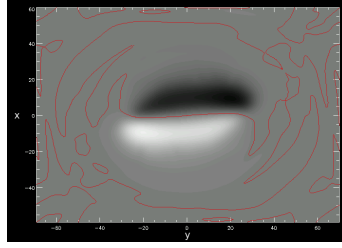
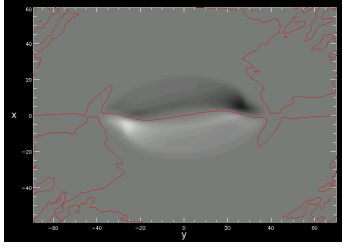


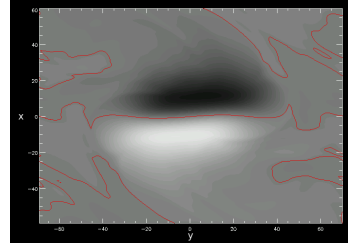
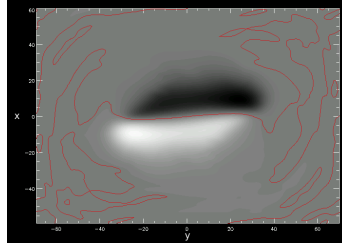
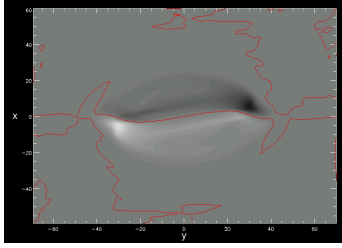
Figure 4.12: 3D views of the model as it evolves, with snapshots taken at times 20, 25, 30, 35, 40, 45, 50, and 55. An isosurface of parallel electric field is shown in green. The base of the photosphere is shown in the middle of the box as a grey scale contour plot of the vertical component of the magnetic field on the photosphere. Magnetic null points are displayed as tetrahedral for improper nulls and spheres for spiral nulls. Red colouring indicates a positive null and blue colouring a negative null. Finally, fieldlines are plotted in four colours: yellow for overlying field, purple for field in the flux tube, and cyan and orange for the two different connectivities of reconnected field joining the flux tube to the overlying field. Figures from Maclean et al. (2008).



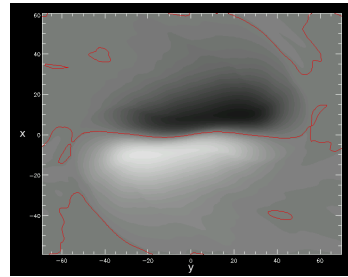
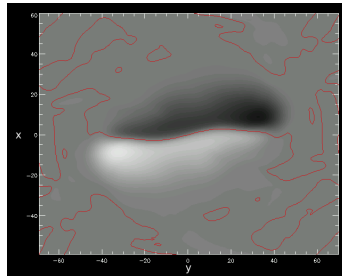
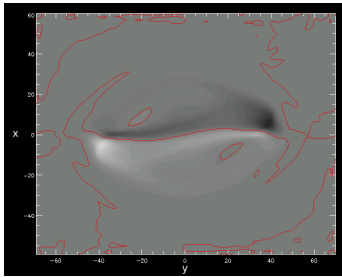
(a)  $z = 22.48$  photospheric cut (b)  $z = 30.06$  cut at snapshot 85 ( $t = 34.02$ ). (c)  $z = 40.16$  cut at snapshot 85 ( $t = 34.02$ ).



(d)  $z = 22.48$  photospheric cut (e)  $z = 30.06$  cut at snapshot 100 ( $t = 37.28$ ). (f)  $z = 40.16$  cut at snapshot 100 ( $t = 37.28$ ).

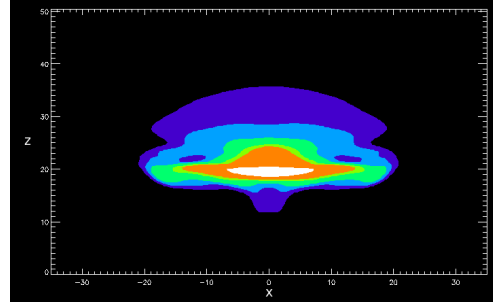
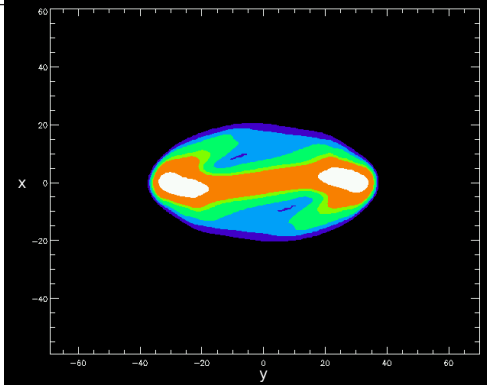


(g)  $z = 22.48$  photospheric cut (h)  $z = 30.06$  cut at snapshot 119 ( $t = 42.20$ ). (i)  $z = 40.16$  cut at snapshot 119 ( $t = 42.20$ ).

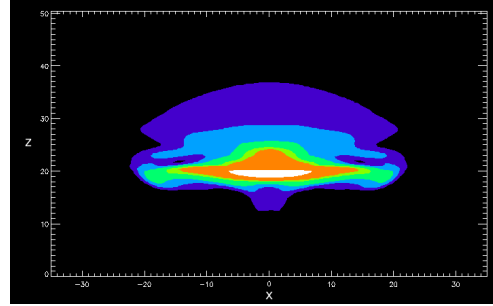
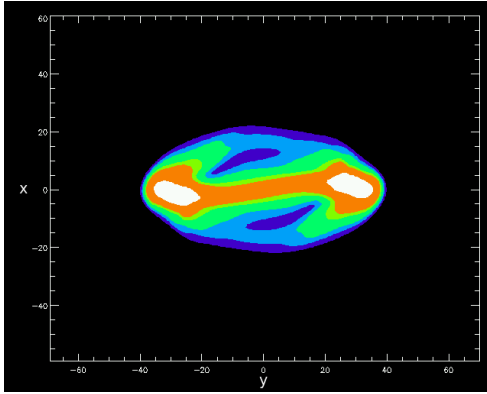


(j)  $z = 22.48$  photospheric cut (k)  $z = 30.06$  cut at snapshot 178 ( $t = 55.13$ ). (l)  $z = 40.16$  cut at snapshot 178 ( $t = 55.13$ ).

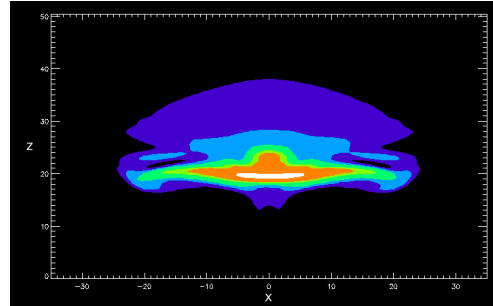
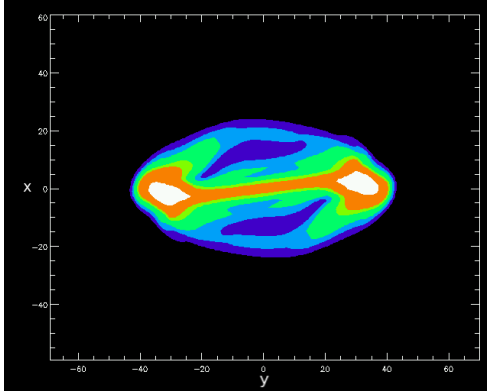
Figure 4.13: Horizontal cuts ( $x-y$  axis) of the magnetic field in different planes and times for the flux emergence experiment with overlying magnetic field. The polarity inversion line (PIL) is plotted in red.



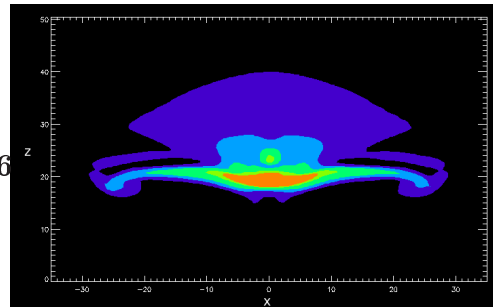
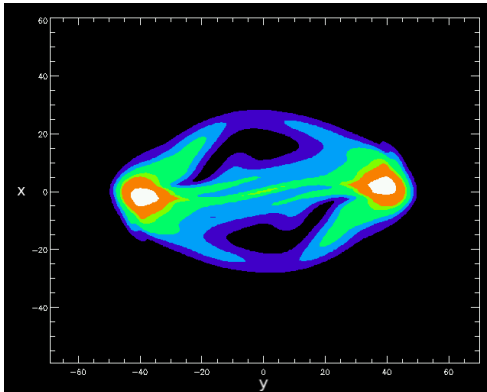
(a)  $z = 22.48$  cut at snapshot 85 ( $t = 34.02$ ). (b) Vertical cut along  $y = 0$  at snapshot 85 ( $t = 34.02$ ).



(c)  $z = 22.48$  cut at snapshot 100 ( $t = 37.28$ ). (d) Vertical cut along  $y = 0$  at snapshot 100 ( $t = 37.28$ ).



(e)  $z = 22.48$  cut at snapshot 119 ( $t = 42.20$ ). (f) Vertical cut along  $y = 0$  at snapshot 119 ( $t = 42.20$ ).



(g)  $z = 22.48$  cut at snapshot 178 ( $t = 55.13$ ). (h) Vertical cut along  $y = 0$  at snapshot 178 ( $t = 55.13$ ).

Figure 4.14: Magnetic field strength. On the left horizontal photospheric cuts ( $y-x$  axis) and on the right vertical cut ( $x-z$  axis) on the middle of the flux rope ( $y = 0$ )

on. In particular they double in number from  $t \simeq 32$  and then oscillate around that number until their number decreased towards the end of the simulation. It is important to notice that the null points (Figure 4.12) are located in two clusters in the low corona ( $z < 20$ ), one to the north and the other to the south of the emerging structure, and that the number of positive null points equal the number of negative null points in every frame. It is interesting that despite the apparent simplicity of the magnetic field passing through the photospheric plane, up to 26 magnetic null points may be present at any time (Figure 4.15). Throughout the model run, only two strong photospheric source regions of magnetic flux are present (one positive and one negative). Parnell et al. (2010) have investigated the separators in this simulation. They found a chain of separators within each null cluster linking the null points and much longer and more important separators (between three connecting one null cluster with the other. The number of these inter-cluster separators change in time from 1 to more than 200. They also relate the separators with high integrated  $E_{\parallel}$  and the connectivity of the field lines. They show that wherever there is a junction of the four flux domains (closed, open, closed-open, and open-closed field lines) a separator has been found, as one would expect. Watching the evolution of the separators, we can see that they change in time starting with very few separator to many separators then going back to only few separators. We chose for our study three snapshots with different topological complexity as shown in Figure 4.16. We start with a snapshot with a complex structure involving many separators and chose snapshots whose topology decreasing complexity in time.

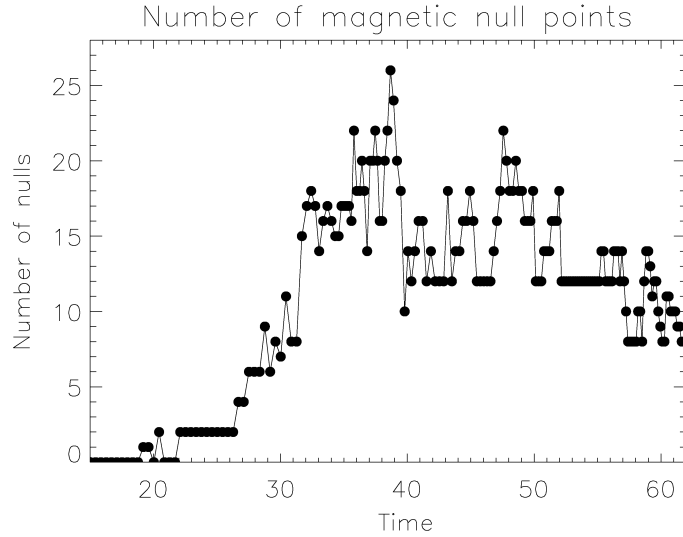
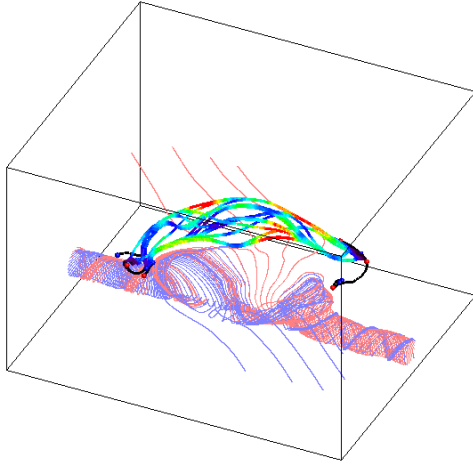
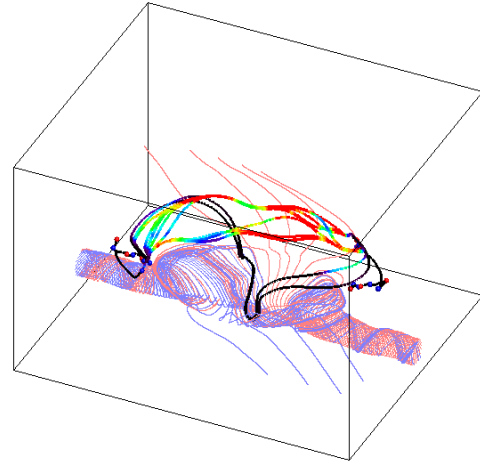


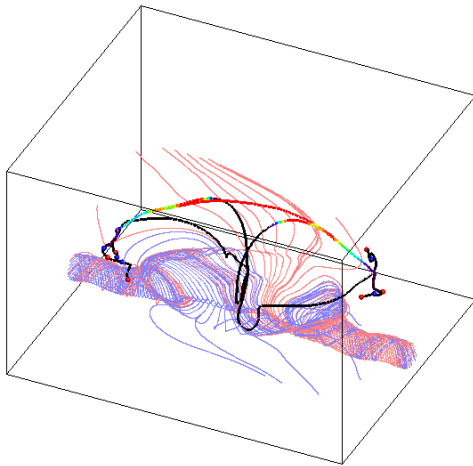
Figure 4.15: The number of magnetic null points present in the model magnetic field, as a function of time. Figure from Maclean et al. (2008).



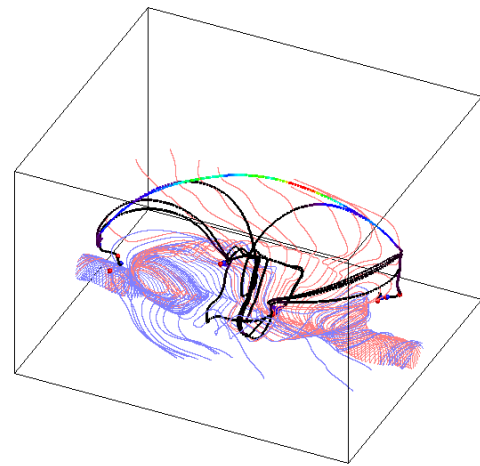
(a) Snapshot 85 ( $t = 34.02$ ).



(b) Snapshot 100 ( $t = 37.28$ ).



(c) Snapshot 119 ( $t = 42.20$ ).



(d) Snapshot 178 ( $t = 55.13$ ).

Figure 4.16: Some of the flux tube field line are plotted in red and blue while the other lines indicate the separators in four different snapshots. The separators are colour coded according to the  $E_{\parallel} > 0$  along them, with black indicating the low  $E_{\parallel} (\approx 0)$  and red indicating the high  $E_{\parallel}$ .

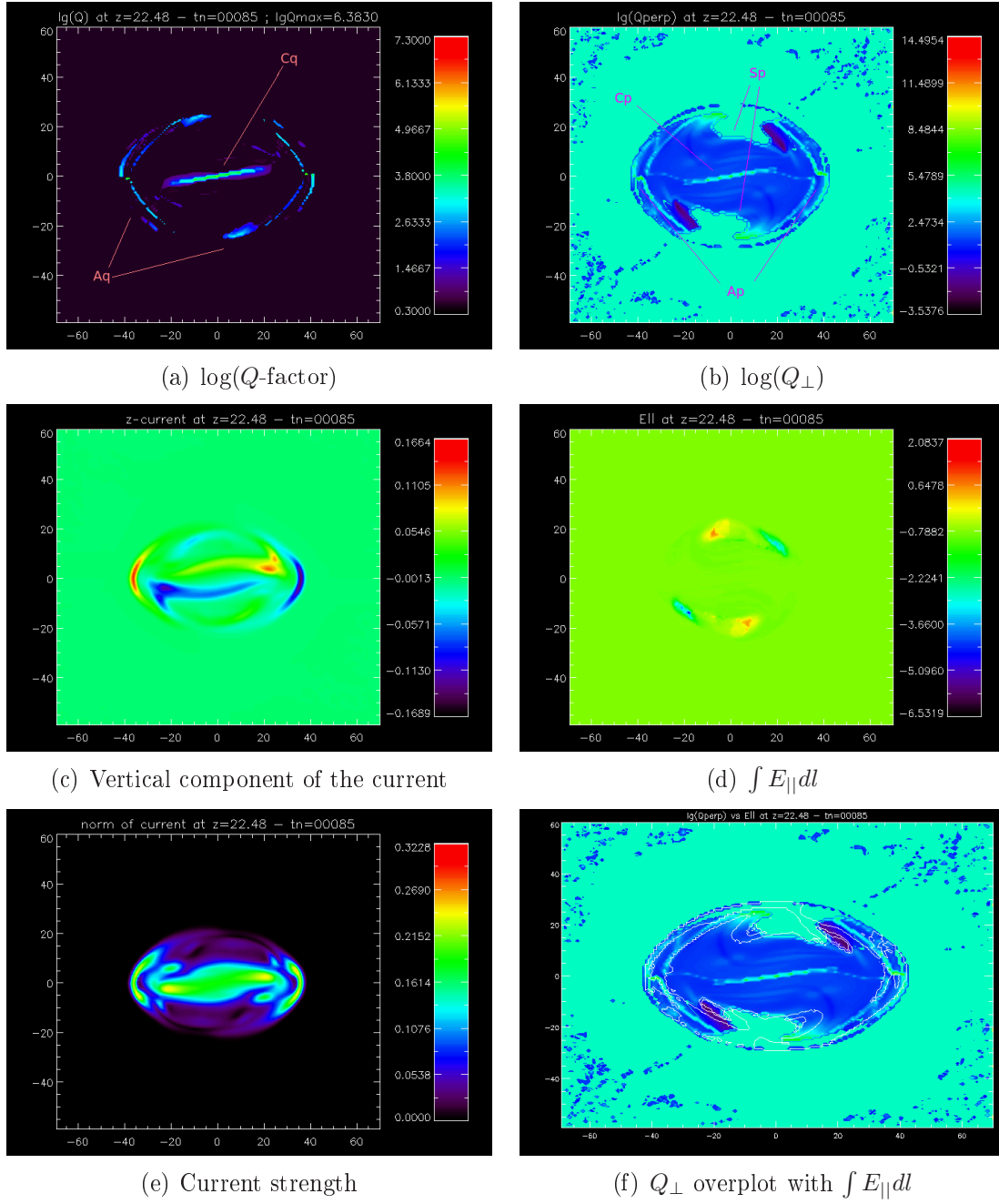


Figure 4.17: Horizontal cuts in the plane  $z = 22.48$  of the respectively quantities at  $t = 34.02$  (snapshot 85).

All the previous papers indicate that the behaviour of the magnetic field is not straight forward during this flux emergence experiment and so here we try to investigate the dynamics of this emergence by considering also the  $Q$ -factor. First we consider horizontal cuts of various quantities. In Figure 4.17, we plot different quantities in the photospheric level for the snapshot 85 ( $t = 34.02$ ) which we are interested in because it occurs after the initial increase in the number of null points and during the reconnection process with the overlying magnetic field. First of all we plot the logarithm of the  $Q$ -factor (Figure 4.17 a) which we compare with the vertical component of the current (Figure 4.17 c) and the strength of the current (Figure 4.17 e). The QSL footprints seems to highlight two main kinds of high  $Q$  regions which are associated with features present in the plot of current. One is the central part of the emerging structure (labelled Cq in Figure 4.17 a), and is passing over the central PIL (see Figure 4.13). This central  $Q$ -factor structure corresponds to a similar structure in the current strength and is surrounded by elongated regions with different polarities of the vertical component of the current as we can see in Figure 4.17 c. The second kind of high- $Q$  feature (labelled Aq in Figure 4.17 a) can be seen in all three plots (Figure 4.17 a-c-e) and it consists of two “arc-like” features on the north and south sides of the emerging structure (compare with Figure 4.13). The associated current sheets on the north and south sides of the emerging flux structure indicate where the flux rope is adjacent the overlying magnetic field in this plane, in fact, it is below the location where the null points have been created (see Figure 4.12).

The other quantities that we plot are the logarithm of  $Q_{\perp}$  and  $E_{\parallel}$  integrated along the field lines and an overplot of these two, at the same time and in the same horizontal cut (Figure 4.17 b, Figure 4.17 d and Figure 4.17 f respectively). As we said in the introduction chapter,  $Q_{\perp}$  is a different way to calculate the squashing factor introduced by Titov (2007) taking into account not only the vertical component of the magnetic field and the horizontal squashing of the field line foot prints, but also taking into account the inclination of the field lines with the plane. In our particular case,  $Q_{\perp}$  seems to have more features then the  $Q$ -factor itself. In particular, one can see the two main structures present in both Figure 4.17 a (Cq, Aq) and Figure 4.17 b (Cp, Ap), but in the  $Q_{\perp}$  they are surrounded by a blue bone shape feature. The north and south part of this bone shape overlap with the arc-like feature (labelled Ap in Figure 4.17 b) of the  $Q$ -factor while “flanks” (labelled Sp in Figure 4.17 b) are additional high- $Q_{\perp}$  features. If we compare the Sp feature with the current (Figure 4.17 e), we can see they surround the central part of the current and in particular the thin regions of the vertical current lying either side of the central PIL (Figure 4.17 c). When we compare the  $Q$ -factors with the reconnection rate ( $\int E_{\parallel} dl$ ) (Figure 4.17 d), we can see that there is not a good match with the  $Q$ -factor. However, when we look at the  $Q_{\perp}$ , it seems that the Sp features (the “flank”) seem to match much better with the  $\int E_{\parallel} dl$ . To verify this, we overplotted

these two quantities (Figure 4.17 f). This overplot reveals that there is not an exact overlap of  $Q_{\perp}$  and  $\int E_{\parallel} dl$ . In fact the high positive (resp. high negative)  $\int E_{\parallel} dl$  is close to the high (resp. low)  $\log(Q_{\perp})$  on the ends of the flank, but are shifted, so they are slightly offset.

Lets now consider the evolution in the photosphere of these different quantities. The quantities that we use to investigate the evolution in the photosphere are the  $Q_{\perp}$ , due to its greater complexity compared to the  $Q$ -factor, and the current (Figure 4.19). As we have already mentioned, with time, the flux rope expands. This can be seen, not only in the magnetic field (Figure 4.13) and in the magnetic field strength (Figure 4.14), but also in the  $Q_{\perp}$  and the current. In the  $Q_{\perp}$  one can see that, while the outer oval structure is expanding, the dark blue bone elongates along the flux tube axis (in a north-south direction), and the flank regions expand and become closer and closer making the bone structure thinner and thinner. Similarly the main central current region lengthens and narrows. The zone outside the blue oval shape is related with open magnetic field.

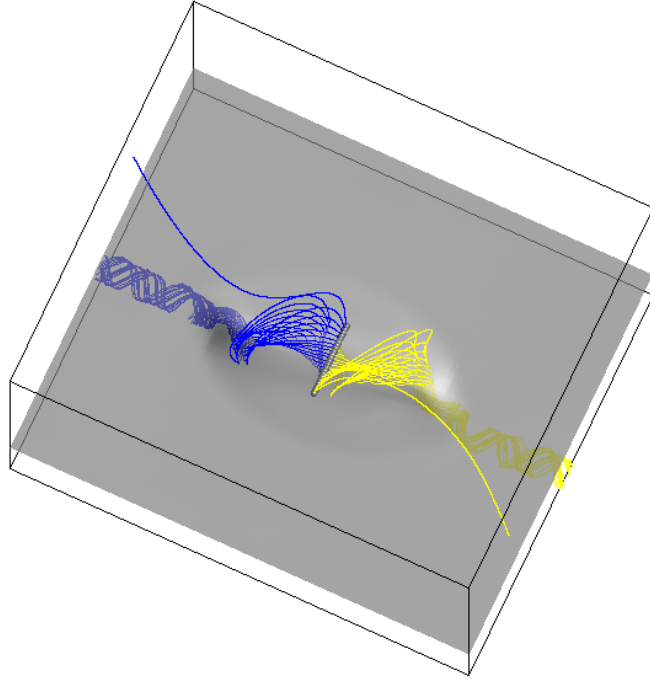


Figure 4.18: Field lines starting from the photosphere along  $y = 0$ . The blue and the yellow colour indicate the different direction from the starting points. The photospheric level is indicates by contour plot of the vertical component of the magnetic field at that level.

In Figure 4.18 we plot the field lines in snapshot 119 ( $t \simeq 50$ ) starting from the photosphere along the  $y = 0$  line which crosses the blue bone feature. The field lines are coloured according to where they move left (blue) or right (yellow) from the starting points. To calculate the  $Q$ -factor and the  $Q_{\perp}$ , we are interested only in the part of the field lines above the photospheric plane. Passing through the middle, the field lines become shorter on one side and longer in the other and vice versa in the other direction. This change gives rise to the central feature of the  $Q_{\perp}$ . Instead, the flank corresponds to where the field lines change from closed to open (in one side). This can be seen in Figure 4.18 where two field lines in the open field line zone are traced. We also investigate the behaviour of  $Q_{\perp}$  and current in two other horizontal cuts at the same three times (Figure 4.20 and Figure 4.21). Figure 4.20 shows the cuts at  $z = 30.06$  which is in the low corona. We can see the central long narrow structure of  $Q_{\perp}$  calculated from these heights is much fainter and more elongated along the flux tube axis compared to the  $z = 22.48$  cuts. In the current, we can see the north and south arc shaped features diverging while the central current tube reflects the flux rope structure emerging with time. In both  $Q_{\perp}$  and current we can also see the interaction with the ambient field indicated by the concentric feature around all these features. In snapshot 119, two additional current features appear at approximately  $x = \pm 20$  and  $y = \mp 10$ . These can be seen also in Figure 4.12, and are a result of the main current sheet in the corona developing east-west wings elongated, and aligned with the direction of the overlying magnetic field ( $\phi = 135$ ) around  $t = 40$  (see green isosurface in Figure 4.12 e).

The behaviour in the  $z = 40.16$  cuts is plotted in Figure 4.21, one can see a similar behaviour to that in Figure 4.20, but here the interaction with the overlying magnetic field is clear in both  $Q_{\perp}$  and current. This is visible through the presence of fragmented structures elongated along the direction of the coronal field ( $\phi = 135$ ).

Summarising our findings from these horizontal cuts of  $Q$  and current we find on the photospheric level two main features. The central one is associated with the axis of the flux tube and the side arcs are associated with the sides of the tube where it interacts with the preexisting coronal field. These side arcs are below the region where the null points occurs (see Figure 4.12). These features are present also in the  $Q_{\perp}$ , but here we also find the appearance of flanks that highlight the change between close field lines and open field lines in one side, while the change through open in both sides field lines is highlight by the blue oval structure in the  $Q_{\perp}$ . These structure evolve in time and height as described.

To better investigate the evolution of  $Q$ , the geometrical features, and to compare these with topological features,  $E_{\parallel}$  and the current during the emergence of the flux tube, we consider a different way of visualising these quantities. In particular we take vertical cuts of these quantities. Such that we can study what is occurring in more of the volume.

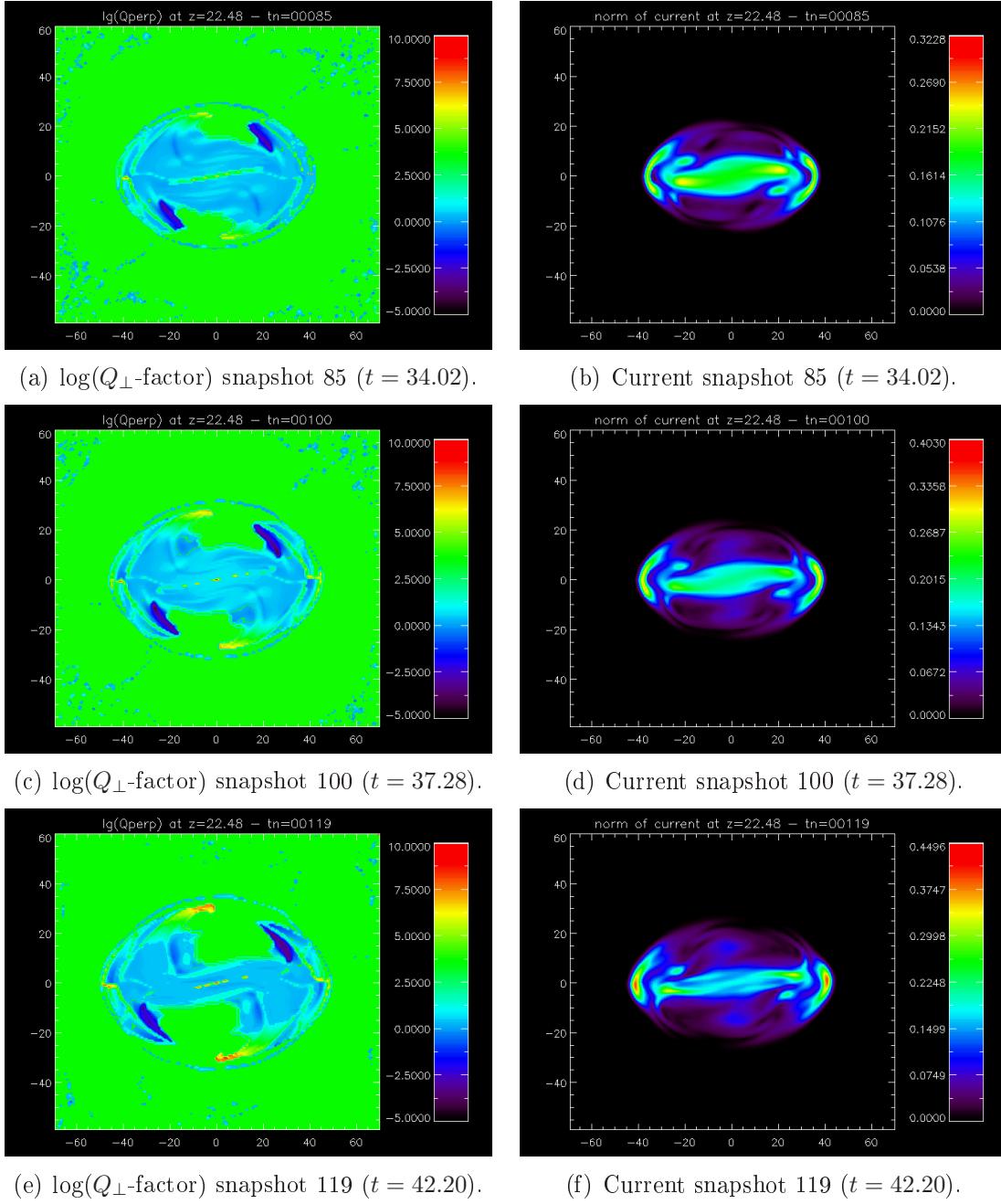


Figure 4.19: Values on the photosphere,  $z = 22.48$ , along the  $y - x$  axis.

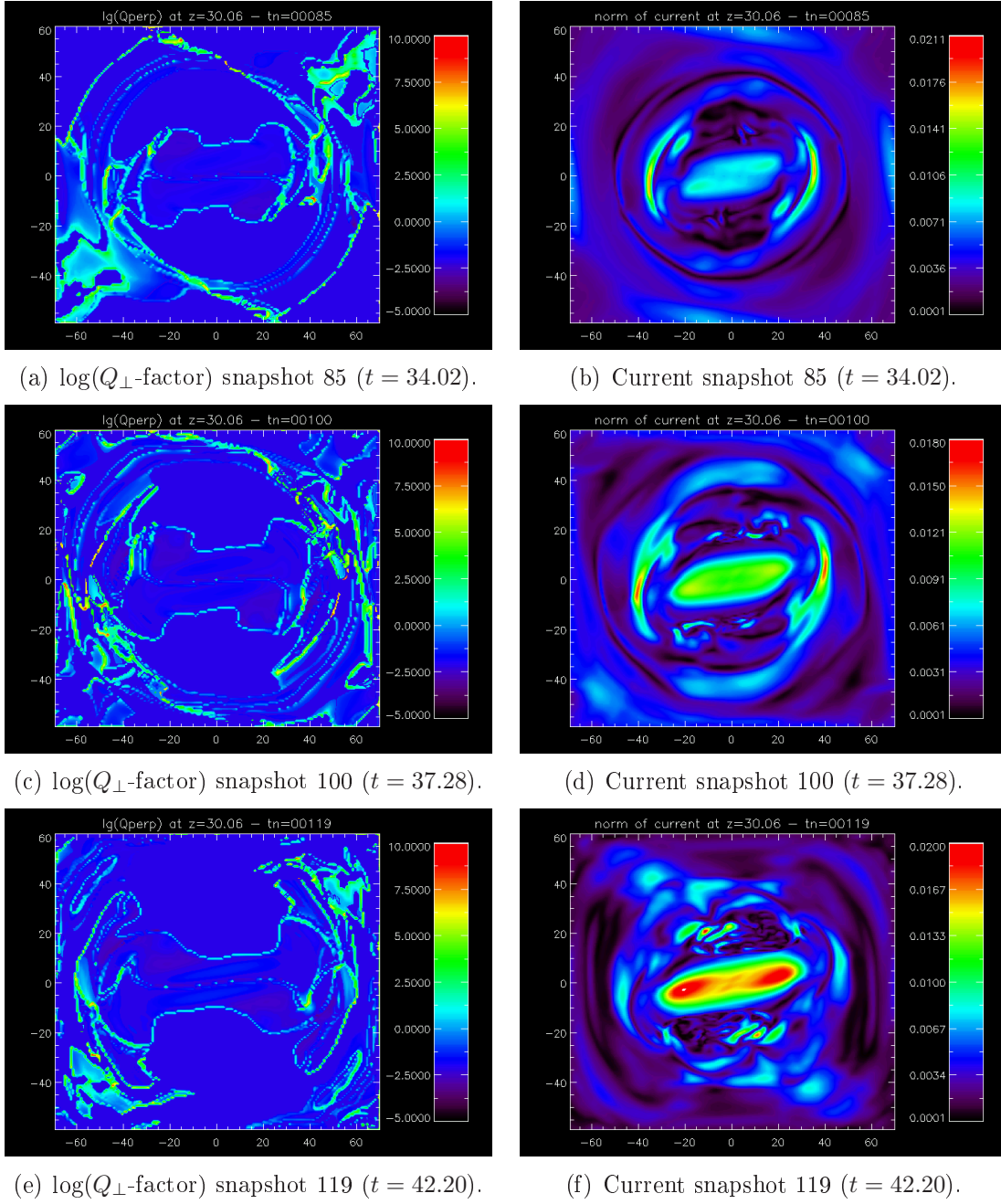


Figure 4.20: Values on  $z = 30.06$ , along the  $y - x$  axis.

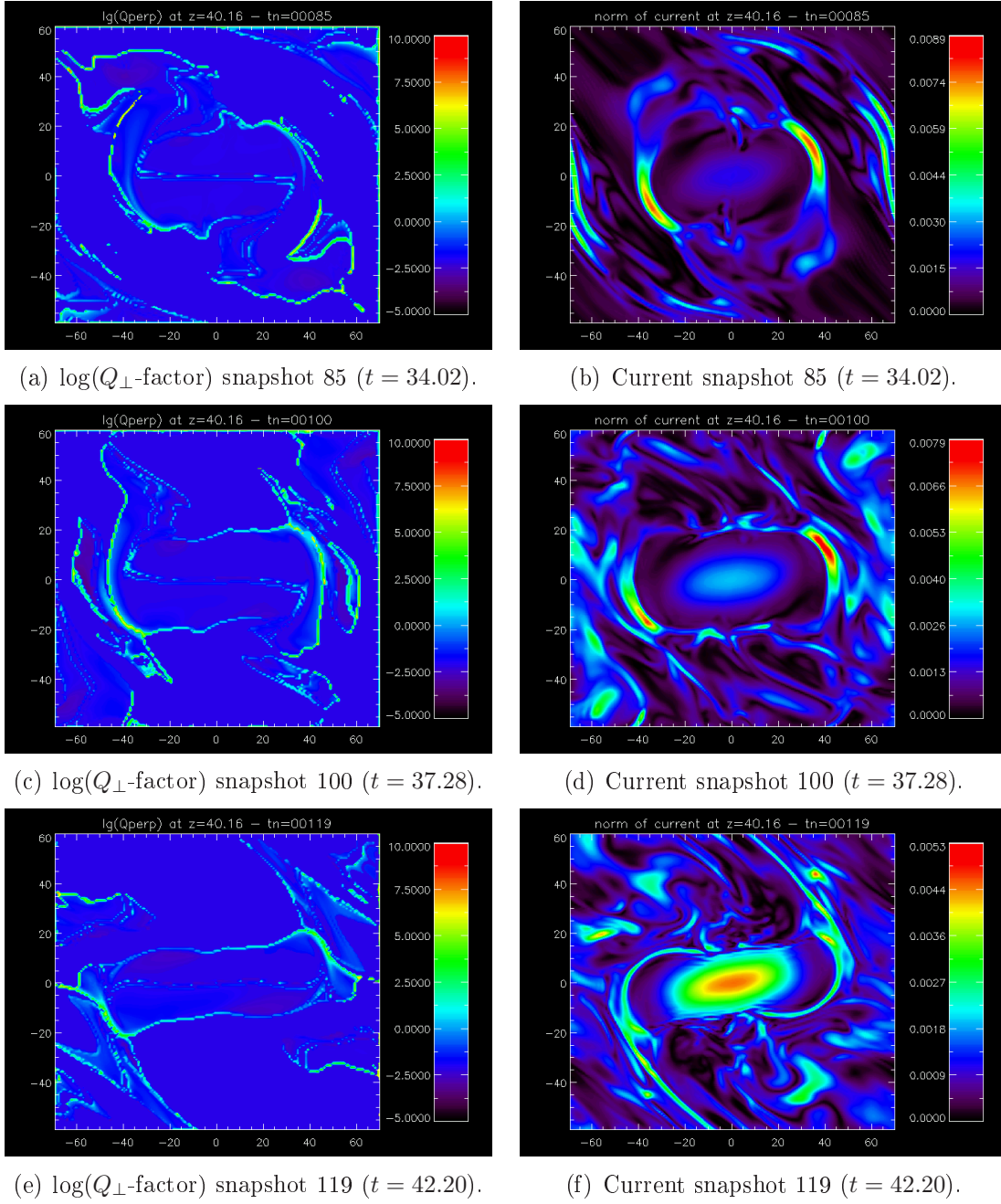


Figure 4.21: Values on  $z = 40.16$ , along the  $y - x$  axis.

### 4.2.1 Vertical cut

The vertical cut that we consider is along  $y = 0$  and extends up from the photosphere ( $z = 22.48$ ). This plot is chosen because it runs perpendicular to the axis of the flux tube and, due to the symmetry of the system, will slice through the main current sheet and reconnection sites of the experiment. We will consider the same snapshots as those considered in the previous section for comparison. Our first time step is snapshot 85. For which we plot the saturated  $Q$ -factor (min= 2, max= 1000), current strength, connectivity and  $\int E_{\parallel} dl$  in this vertical plane in Figure 4.22. Figure 4.22 a-b show the  $Q$ -factor in this plane calculated in two different ways. In the first case (resp. in the second) we considered the field lines passing through the vertical plane and traced forward (resp. backward) to the photosphere. Then we took their neighbour on the photosphere to calculate their  $Q$ -factor in the usual way (see the Introduction for more detail on this calculation). If we compare the  $Q$ -factor found from the two sides of the cut, Figure 4.22 a with Figure 4.22 b, we can see that the high  $Q$ -regions map an external/shell structure (labelled Sf in Figure 4.22 a-b) is the same in both figures, but the high  $Q$  structures internal to the expanding flux rope (labelled If in Figure 4.22 a-b-c) are different. In fact the forward traced field lines only see an internal (If) high  $Q$  structure on the right and not the one on the left, and vice versa for the backward traced field lines. The  $Q$ -factor, as defined by Titov et al. (2002), should be the same if calculated in one direction or the other. However the difference we find in the vertical plane can be explained basically because there is a different choice of neighbour used to find  $Q$  for the field lines traced forwards to those traced backwards from the vertical cut. To visualise these problems, let us go back to the toy model in Figure 3.7 on Chapter 3. When we take a couple of field lines starting on the left hand side of the loop with a fixed distance  $\delta$  from each other, e.g. the red field lines, we can see that these field lines start relatively close to each other and end relatively far away from one to the other. Now, if we consider instead a couple of field lines starting on the right side of the loop with a distance  $\delta$  (i.e. lying in between the ending points of the red field lines), we see that they will not spread out but will converge to practically the same point. Additionally, there may be also an other problem add to this one due to the numerical resolution (we use double resolution). In fact if they end up even closer then our resolution, the ending point (on the left hand side of the loop) will be exactly the same point for both field lines of the pair in our calculation of  $Q$ . Thus the  $Q$ -factor for the main field line that has these couple as neighbours, will have a different  $Q$  if we calculate it from the neighbours on one end or the other of the loop. Thus field lines in our vertical cut which show this behaviour will have different features in the two  $Q$ -factor plots. To bypass this problem, we consider the maximum of the two  $Q$ -factors calculated. Doing this for the cut in snapshot 85, we obtain Figure 4.22 c. Here we can see that the shell (labelled Sf) is the same and

that both of the internal features (labelled If) are visible.

In Figure 4.22 d we plot the current strength on the middle vertical cut. Regions of high current are seen in and just above the photosphere and also two main features in the corona. The photospheric features are due to field lines that are trapped at this level having not yet undergone the second instability and risen up to reconnect with the overlying field. The coronal currents form a pair of arches where the emerging field lines compress against the overlying magnetic field. The higher arch and the lower arch just below, surround the top of the shell seen in the  $Q$ -factor plot (Figure 4.22 c). In Figure 4.22 e we plot the connectivity of the field lines. The red regions indicate open coronal field lines, the yellow (resp. cyan) are field lines closed on one side and open from the other i.e. field lines that follow the flux tube in one side and not the other (resp. vice versa) and the blue indicate closed field lines. In Figure 4.22 f we plot the absolute  $E_{\parallel}$  integrated along the field lines. The non-zero regions of  $\int E_{\parallel} dl$  fill the region through which the flux tube thread as well as (with lower regions) wings of the open-closed and closed-open regions. However when we decompose  $\int E_{\parallel} dl$  and only consider the positive and negative contributions separately, we find two very different plots in the vertical cuts. In Figure 4.22 h we plot the negative contribution. This forms a large diffuse structure that is highest for the field lines at the centre of the flux tube, close to its axis located below the photosphere, and is produced by the current present from the beginning of the simulation. The initial flux tube is twisted and thus is associated with current through out its volume. The component of  $\int E_{\parallel} dl$  that gives us the location of the reconnection is the positive one which is plotted in Figure 4.22 g. The positive contribution to  $\int E_{\parallel} dl$  forms narrow thin structures and is highest at the top of the emerging flux tube, where the higher arched coronal current sheet in the vertical cut is located. This is also the region through which the separators which connect the clusters of null points on either sides of the emerging tube, thread this cut at this snapshot (Figure 4.16).

In order to consider the evolution of the emerging flux rope we have made vertical cuts in three other snapshots and plotted the same quantities. These snapshots are the same as those in which we studied the horizontal cuts (i.e. snapshot 100 ( $t = 37.28$ ) in Figure 4.23, and snapshot 119 ( $t = 42.20$ ) in Figure 4.24). In the max  $Q$ -factor plots, we see that the encompassing high- $Q$  shell, which lies at the boundary between field lines of different connectivity, becomes taller and thinner with time and that the double layer top seen in snapshot 85 reduced to only one line in snapshot 100. The two high  $Q$  double layer structures inside the shell in snapshot 85 overlap in snapshot 100 forming a bubble feature (labelled Bb in Figure 4.23 a) in the centre of the emerging structure and a fish tail structure below it (labelled ft in Figure 4.24 a). This bubble feature grows in time and rises merging with the top of the shell structure by frame 119. The number of separator decreases in our frames. In snapshot 85 and 100 there are various separators crossing the vertical cut in the

corona in the region where the high positive integrated  $E_{\parallel}$  highlights the top of the shell (Figure 4.22 e and Figure 4.23 e). When the number of separators threading vertical cuts reduces to one, as in snapshots 119 and 178, we have in the positive contribution of the  $\int E_{\parallel} dl$  (Figure 4.24 e and Figure 4.25 e), a collapsed X-shape feature (labelled X in Figure 4.25 e) as in the paper by Aulanier et al. (2005).

To understand the cause of all these  $Q$  features we look at the behaviour of the field lines relating to them, by drawing 3D plots. Starting with snapshot 85, in Figure 4.26, we plot two different sets of field lines: in the top panels (Figure 4.26 a-b) field lines starting from  $y = 0$  and  $z = 35$ , while in the bottom ones (Figure 4.26 c-d) there are field lines traced starting from  $x = 10$  and  $y = 0$  (as shown by horizontal and vertical yellow lines in Figure 4.22 c, respectively). We chose these different lines of starting points to highlight the changes in the field line geometry related to different high- $Q$  features. The horizontal line along  $z = 35$  plotted on the  $Q$ -factor plot (Figure 4.26 c) cuts through three different features: the two internal features on the sides and the inside of the flux tube in the middle. In the top panels of Figure 4.22, the field lines starting on this line which reside inside the flux tube are plotted in blue, while the others are coloured green in one direction and red in the other. We can see that the blue field lines have an arch shape and are parallel to each other following the original twisting of the rising flux tube and these are associated with a very low  $Q$ -factor. The other field lines (which the forward (resp. backward) direction is coloured in green (resp. red)), however are not so symmetric in their behaviour about this cut. They rise up above the height of the central line and are more twisted. The change from one kind of field line to the other is highlighted in the high- $Q$  internal features. In the bottom panels (Figure 4.26 c-d), we plot field lines traced starting from a line in the central vertical plane along  $x = 10$  as shown from the yellow vertical line in Figure 4.22. We choose this  $x$  value to explain the high  $Q$ -features it crosses. In blue and yellow we plot the field lines below the internal feature, in light blue and orange the field lines starting between the internal feature and the shell are plotted, in violet and dark orange the field lines inside the double layer of the top shell are plotted, and in red and blue the field lines above the shell are traced. We can see that passing through the internal feature the field lines change from having an arch shape to an  $\Omega$  one (Figure 4.26 d). This results in the lowest high- $Q$  feature we cross. The field lines inside the double layer change their orientation rapidly with height becoming perpendicular to the overlying magnetic field and eventually reconnecting with it. The changes in behaviour of the field lines is associated with another high- $Q$  feature. The top shell shape in the end, gives us the location of changing in connectivity from open to close field lines (Figure 4.26 e).

In Figure 4.27 we plot, at snapshot 100, field lines starting from the vertical line crossing the centre of the box ( $x = y = 0$ ). We again plot in different colours field lines starting from different regions bounded by different high- $Q$  features. In yellow we plot the field lines starting inside the fish tail feature (labelled ft in Figure 4.23 a),

in orange the ones starting from inside the bubble (labelled Bb in Figure 4.23 a), in red the field lines from the region between the bubble and the top of the shell, and in pink the field lines from the shell and above this. From the top view (Figure 4.27 d) we see that the field lines change their inclination with height. We see the yellow field line foot prints start parallel to the flux tube axis connecting two BPs. As the angle these line make with the axis of the flux tube increases, these lines change colour to orange field lines. It is important to note the appearances of the yellow field line at this stage. These field lines are similar to the ones described by Titov and Démoulin (1999) and plotted in Figure 4.5 and in blue in Figure 4.6. On snapshot 85 the field lines at this height followed the inclination of the twist of the flux tube, now however they change geometry connecting the newly formed BPs. The red field lines are different from the lower ones, because they change from arch shaped to  $\Omega$  shaped. In the end the pink field lines change from closed to open field lines. In particular, the lower pink field line is plotted exactly from the shell of the  $Q$ -factor. This field line changes its inclination drastically from the one below and in the step between the previous field lines and the open ones. This pink field line corresponds to the dark-orange/violet field lines starting from inside the bifurcation on snapshot 85 in Figure 4.26. Again the change between the different coloured field lines results in the high- $Q$  features we see in Figure 4.23.

At frame 119, shown in Figure 4.24, the bubble feature, present in the  $Q$ -factor at snapshot 100, merges with the shell. This gives, on the central axis, a change between only three different features. So in Figure 4.28 we have field lines plotted in three different colours (pink, blue, purple). The pink field lines are traced from inside the fish tail feature. Seen with a top view (Figure 4.28 d), these field lines have a steep slant passing from one foot point to the neighbouring one. This slope changes as we pass on to plotting the blue field lines which lie inside the bubble feature. It is important to notice that both of these kinds of field lines form a twisted arch shape. If we look at the orientation of each single field line from the top view (Figure 4.28 d), we can see that their inclination increases from one to the other with height starting from field lines parallel to the tube axis up to field lines perpendicular to the overlying magnetic field.

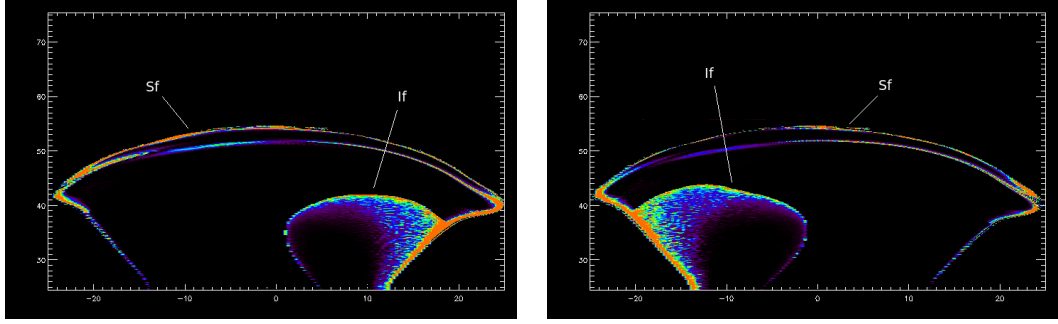
At snapshot 178, the fish tail feature and the bubble feature in Figure 4.25 a start to disconnect and diverge from each other. In Figure 4.29 a-b we plot field lines starting from a horizontal line at  $z = 35$  (traced in yellow in Figure 4.25 a). This cut passes through the disconnection point of these two features. In snapshot 100 we saw in the  $Q$ -factor plot the appearance of two pairs of internal side structures (labelled Is1 and Is2 in Figure 4.23). These started from the side shell in snapshot 100, increase in snapshot 119, and evolve to become two single features here in snapshot 178. Plotting field lines from this horizontal line, we can visualise the change of geometry across these features that before were too weak compared to the other high- $Q$  features to be seen. As before, we plot with different colours field

lines residing between different high- $Q$  features. In orange we plot the field lines starting from the centre and in light green and violet the field lines starting from the sides. Here we can see the change of geometry between them. In the centre the field lines are parallel to each other, while in the sides they start close to each other and diverge on the other side of the vertical cut and vice versa. The dark green field lines are open field lines plotted starting from points just outside the shell.

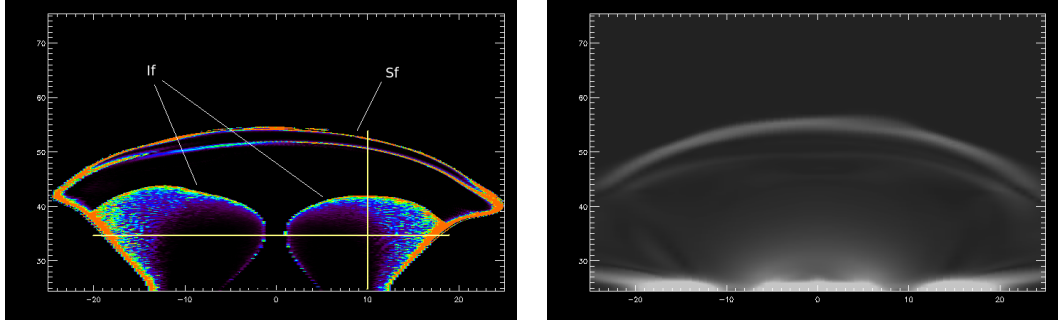
In Figure 4.29 c-d we plot field lines starting from a vertical line in the centre of the box ( $x = y = 0$ ). This line crosses three different high- $Q$  features. First of all, we plot in pink the field lines residing inside the fish tail  $Q$ -factor feature in Figure 4.25. These field lines are related with the so called “eruption flux rope” plotted as the blue field lines in Figure 4.11 by Archontis and Török (2008). They are equivalent to the yellow field lines in Figure 4.27 and the pink field lines in Figure 4.28. We see that these field lines create a second axis of the flux tube and here become surrounded by the blue field lines (which start from the region between the bubble feature and the fish tail one) becoming effectively a new “internal flux rope” as we can see also in the vertical cut plot of the magnetic field strength in Figure 4.14 h. Finally the purple field lines are plotted from the bubble feature up to outside the high- $Q$  shell region. We can see their slow twist with altitude and so that they lay at right angle to the open field lines above.

In general, when the current is compared with the  $Q$ -factor we see features in one of these plots that do not have any correspondence in the other and vice versa. For example the internal high- $Q$  features, that we have discussed in detail above, are not visible in any of the current plots at the different times. While the only structure that has a direct correspondence is the high- $Q$  shell feature. Similarly for the internal current photospheric features which have no high- $Q$  counter parts, except in snapshot 178 where the central photospheric current feature highlights the inside on the fish tail in the  $Q$ -factor plot (Figure 4.25 a-b). Also, if we consider for example the plot of the current from snapshot 119 in Figure 4.24 b we have some narrow wings on the bottom of the plot outside the border of the emerging flux tube structure. These features (present also in the other snapshots) are not visible in the  $Q$ -factor plots since they are related to field lines that are considered as open and thus have a  $Q = 2$ . This is particularly visible when we compare the current and  $Q$ -factor plots with the connectivity ones. Similar things occur between the  $Q$  and the  $\int E_{\parallel} dl$ , the  $Q$ -factor plots have more features than the  $\int E_{\parallel} dl$  ones, but there are features in the  $\int E_{\parallel} dl$  associated with open field lines which  $Q$  can not catch.

Summarising we investigate the geometry of field lines associated with high- $Q$  features in central vertical cut of the studied flux rope. We have shown the evolution of the  $Q$ -factor and looked for a correlation with other quantities such as the  $\int E_{\parallel} dl$ , the connectivity and the current. We found relations between them, but not a one to one correspondence.

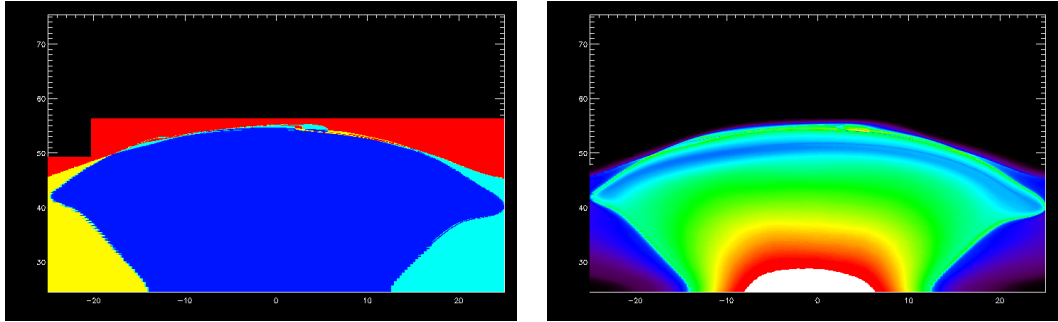


(a) Saturated  $Q$ -factor calculated from field lines traced forward. (b) Saturated  $Q$ -factor calculated from field lines traced backward.



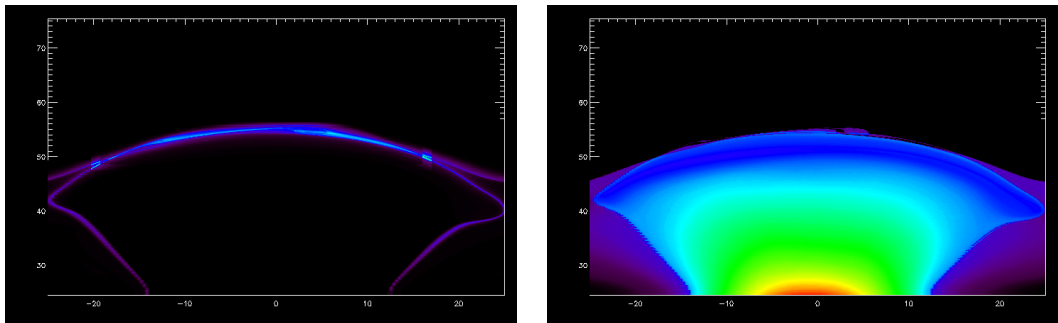
(c) Saturated  $Q$ -factor.

(d) Current.



(e) Connectivity.

(f)  $E_{\parallel}$  integrated along the field lines.



(g) Positive  $E_{\parallel}$  integrated along the field lines. (h) Negative  $E_{\parallel}$  integrated along the field lines.

Figure 4.22: Vertical cut at snapshot 85 ( $t = 34.02$ ).

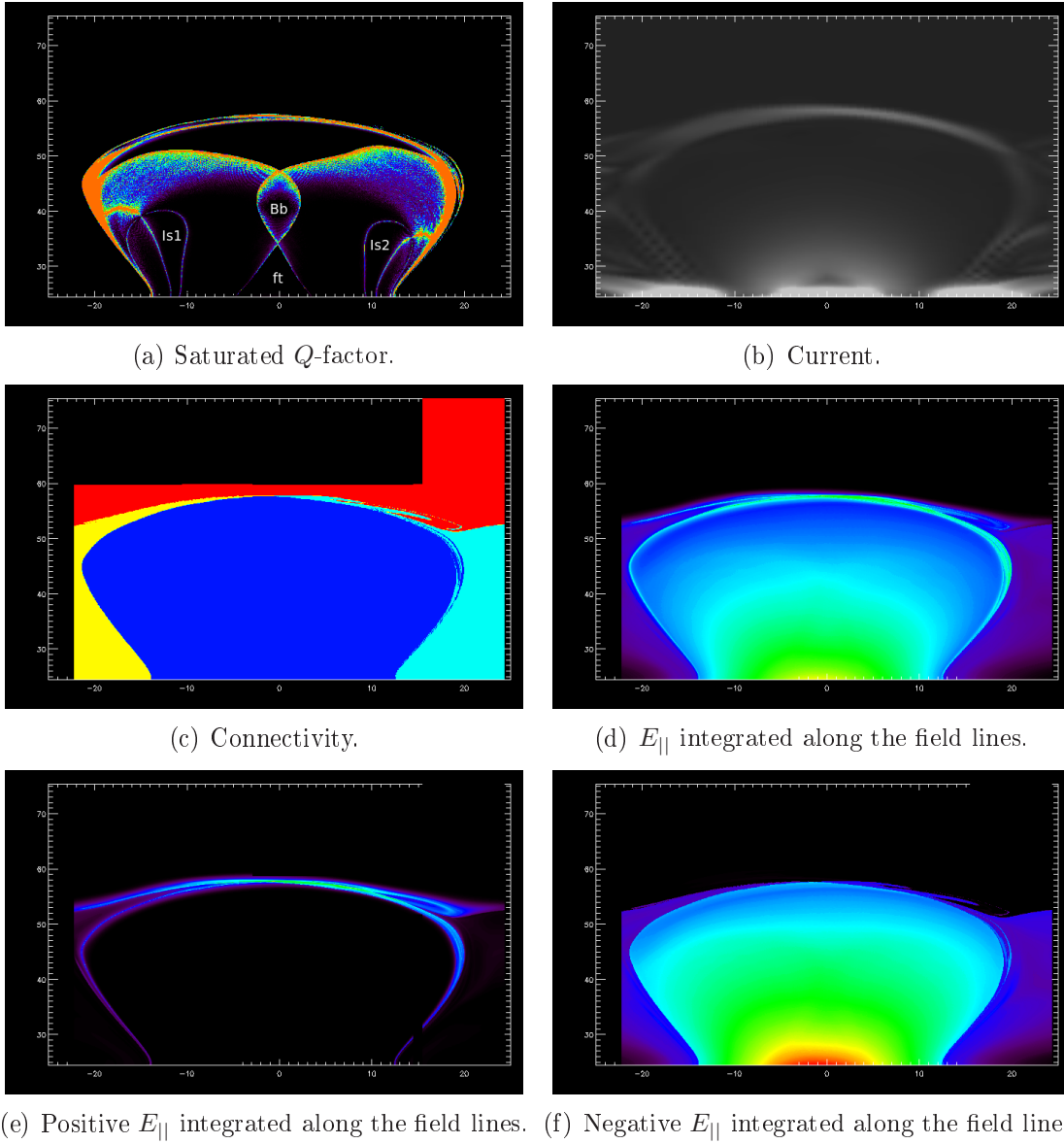


Figure 4.23: Vertical cut at snapshot 100 ( $t = 37.28$ ).

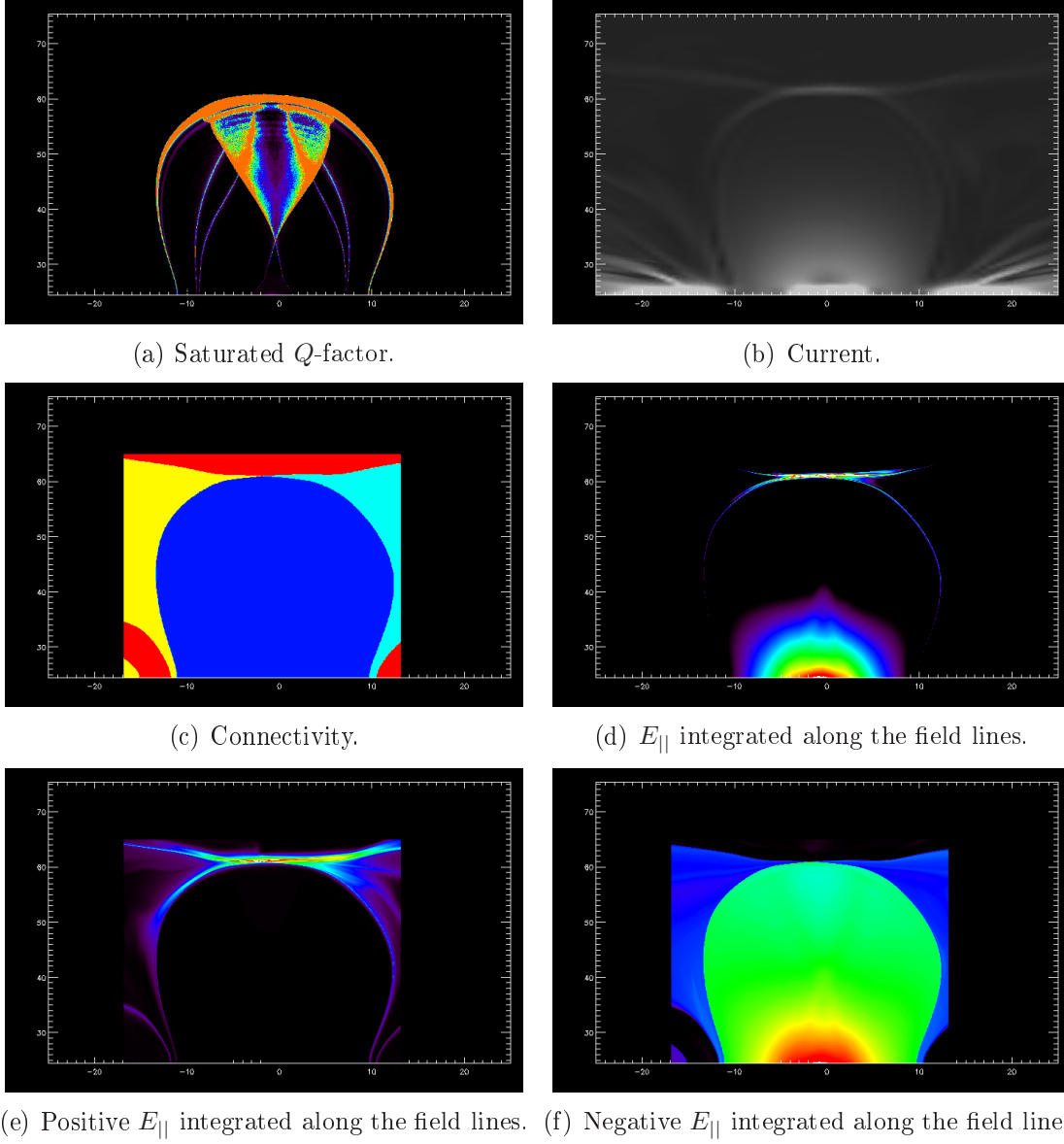


Figure 4.24: Vertical cut at snapshot 119 ( $t = 42.20$ ).

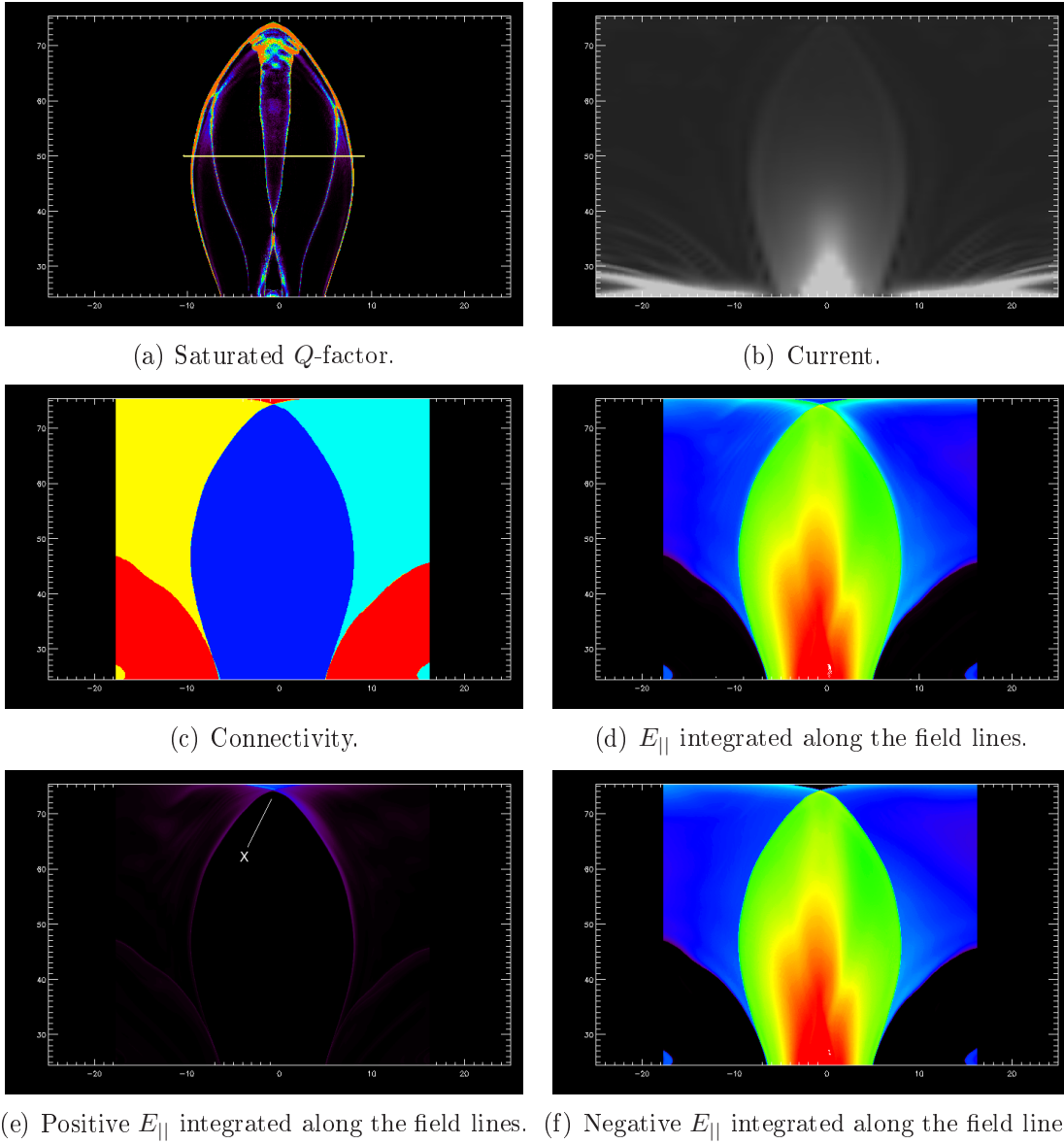


Figure 4.25: Vertical cut at snapshot 178 ( $t = 55.13$ ).

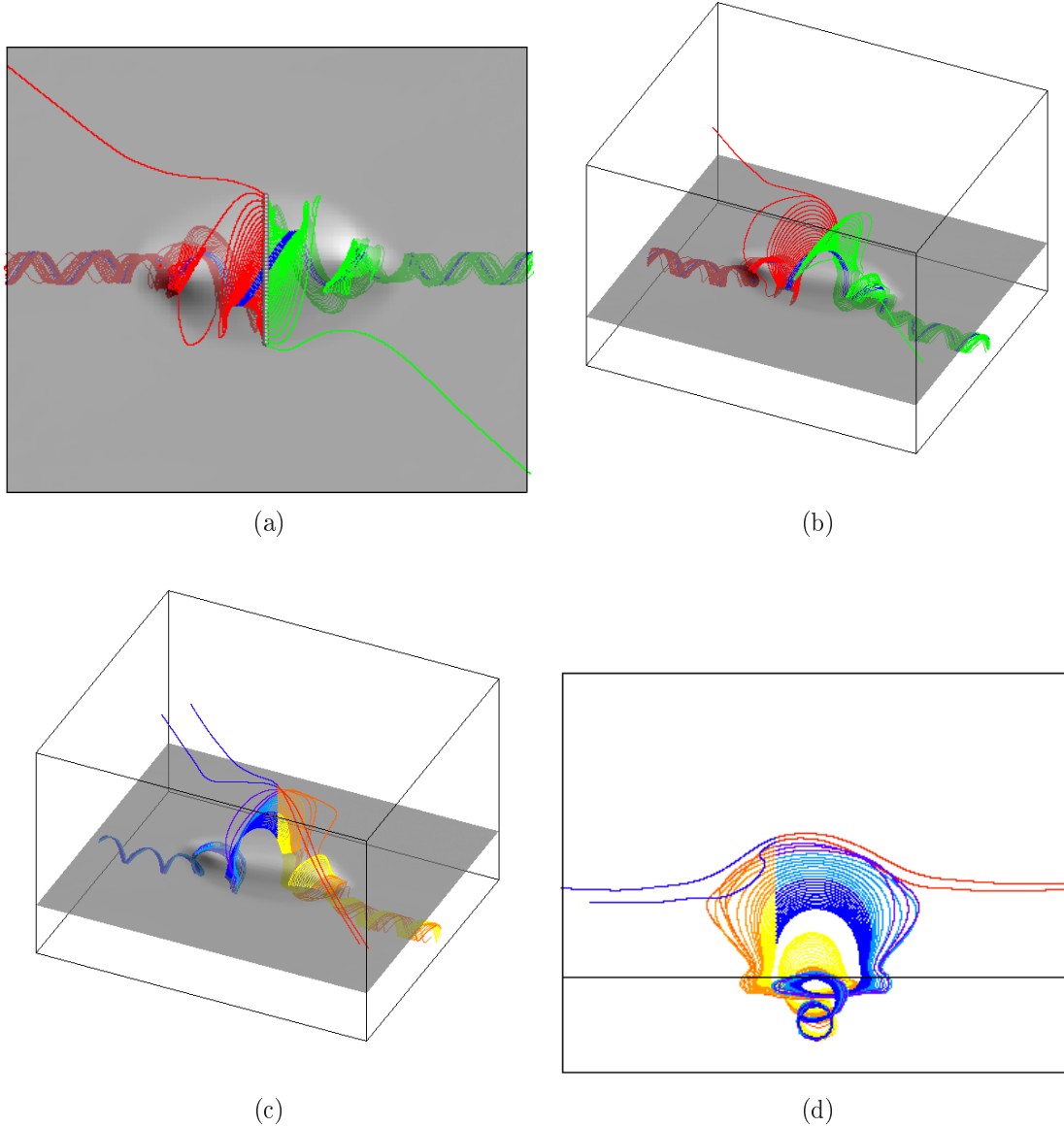


Figure 4.26: Plot of field lines at snapshot 85 overplotted with the vertical component of the magnetic field on the photospheric height. (a) and (b) are field lines starting from  $y = 0$  and  $z = 35$ . (c) and (d) are field lines traced starting from  $x = 10$  and  $y = 0$ . They correspond respectively to the horizontal and vertical lines in Figure 4.22.

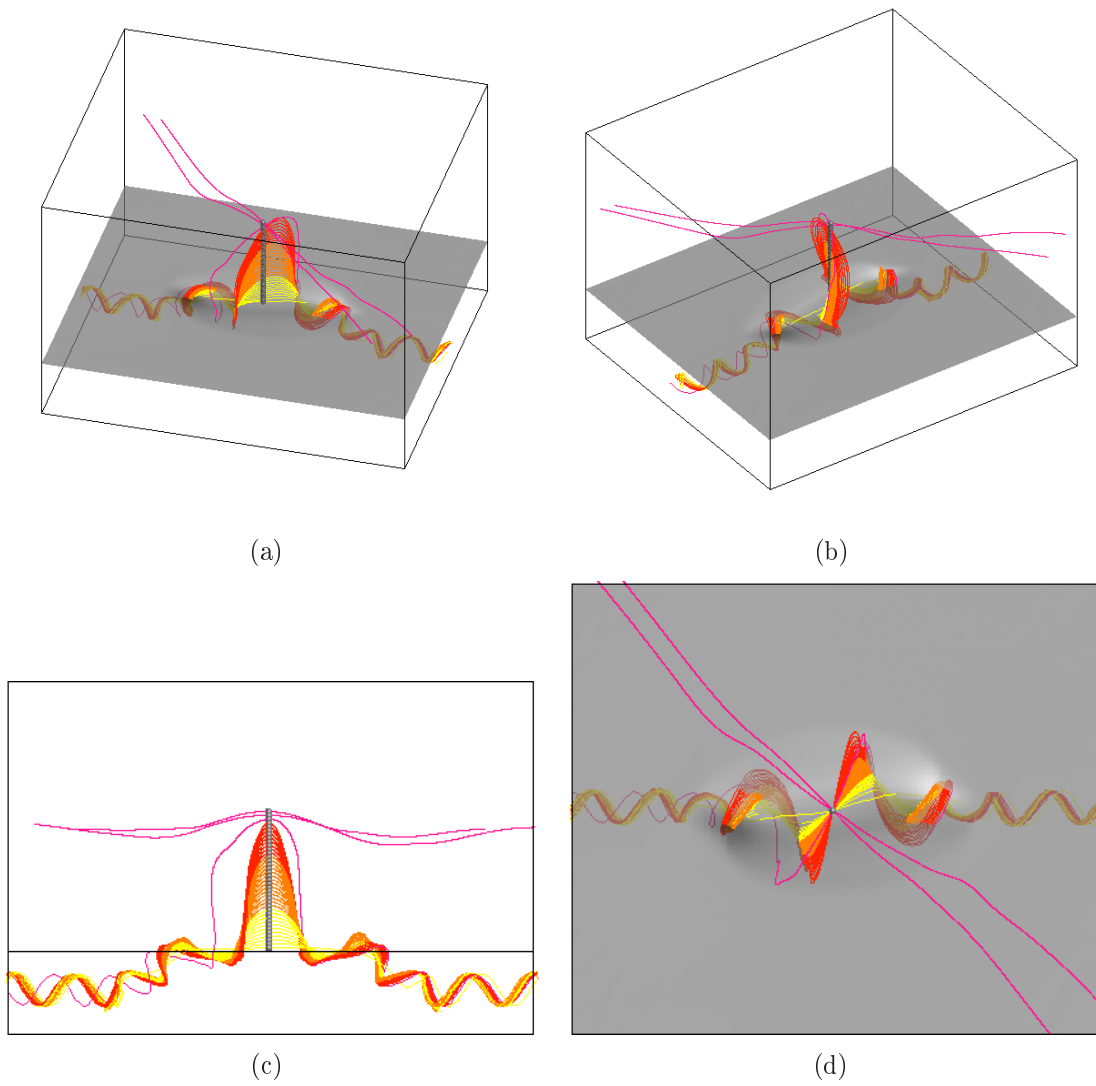


Figure 4.27: Plot of field lines at snapshot 100 traced starting from  $x = 0$  and  $y = 0$ , overlotted with the vertical component of the magnetic field on the photospheric height.

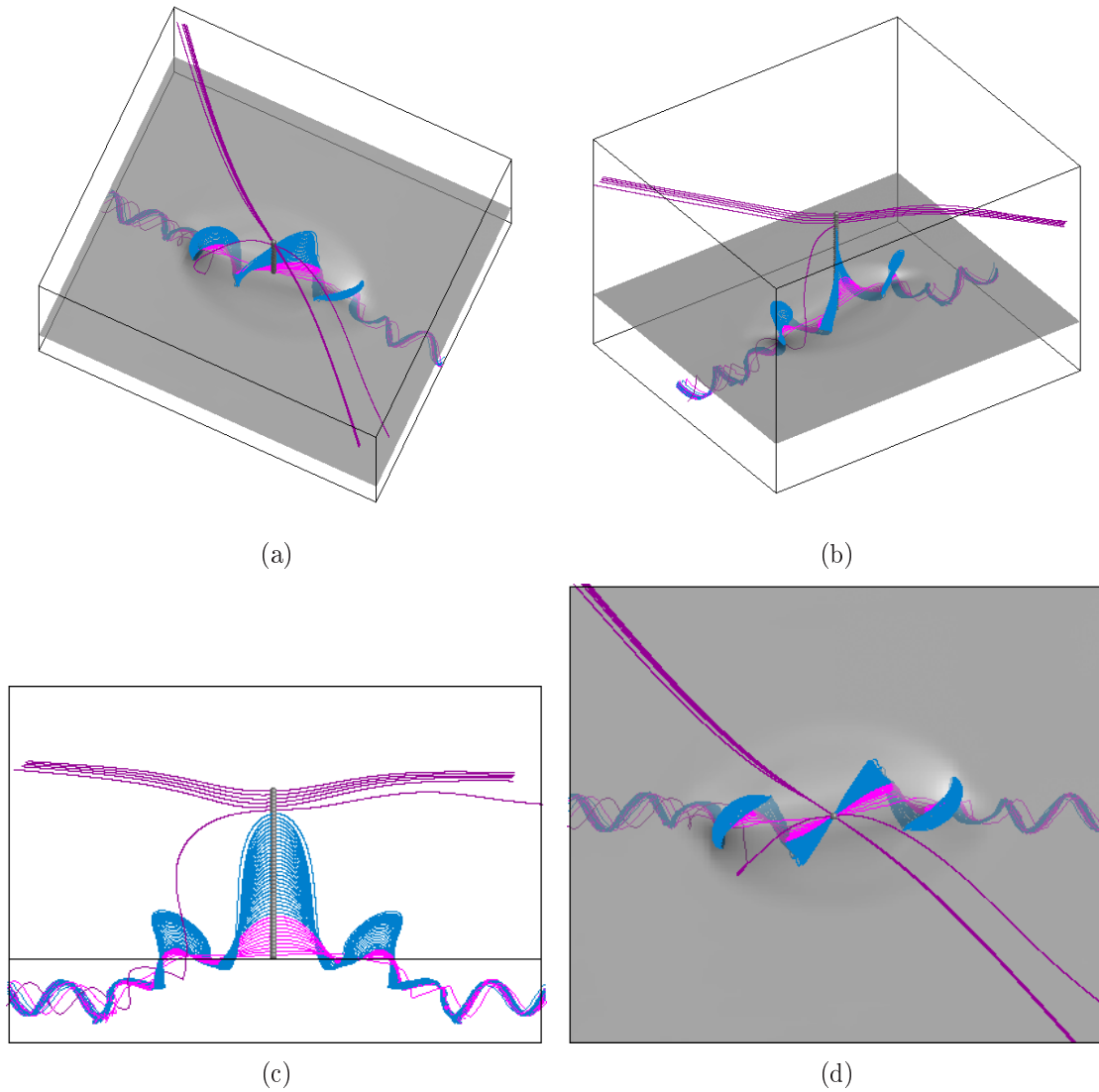


Figure 4.28: Plot of field lines at snapshot 119 traced starting from  $x = y = 0$  overlotted with the vertical component of the magnetic field on the photospheric height.

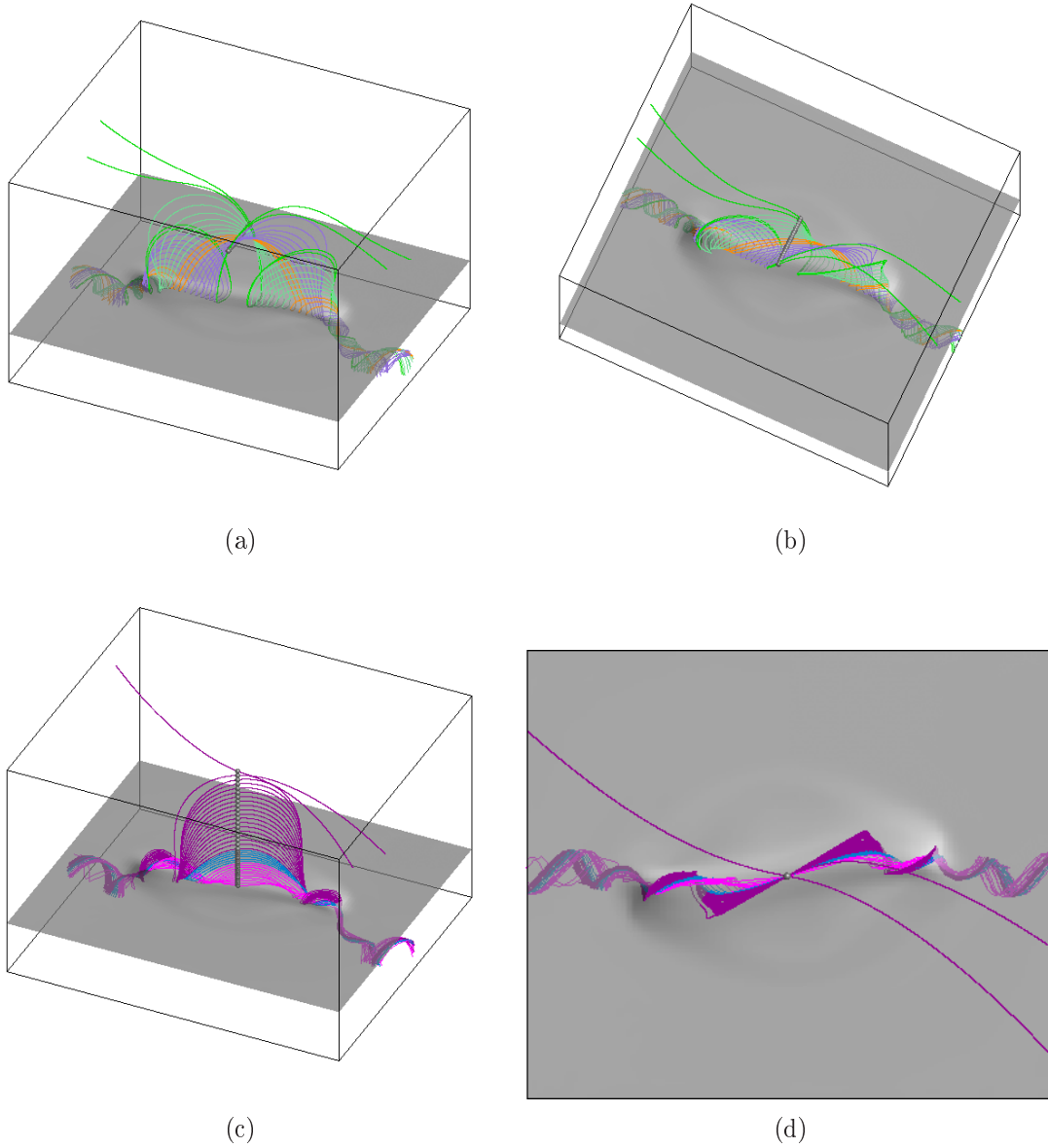


Figure 4.29: Plot of field lines at snapshot 178 overlotted with the vertical component of the magnetic field on the photospheric height. (a) and (b) are field lines starting from  $y = 0$  and  $z = 50$  (horizontal yellow line in Figure 4.25). (c) and (d) are field lines traced starting from  $x = 0$  and  $y = 0$ .

# Chapter 5

## Conclusion

The magnetic field structures of the solar atmosphere are very complex and highly dynamic. Over recent years a particular locator of interesting geometrical features, known as QSLs, has been used to identify likely sites of magnetic reconnection.

Our goal in this thesis is to find the relation between these geometrical features (QSLs), the magnetic skeleton and currents in the low solar corona. With this aim we have conducted three different kinds of studies. First of all we considered the magnetic field in the atmosphere derived directly from the observed field in the photosphere: a NLFF magnetic field extrapolation from observed magnetograms of a flare event. We studied the geometry of the field lines in the pre-erupting phase and saw how it evolved after the event. In the pre-erupting phase, we have found an Hyperbolic Flux Tube (HFT) related to some main QSL features that disappear after the flare event presumably due to its emergence. The field line geometry in the studied case before the event consists of a HFT overlaid by a flux rope. We hypothesise that the HFT was created by the combination of the shift and the spin rotation of the positive south polarity around the northern negative ones constituting our system. We also calculate the QSLs and the current at different fixed levels: the photosphere and a low corona ( $z = 5 \text{ pixel}$ ). At the photospheric level a comparison was difficult due to their chaotic shape, but we could see a match between their location on  $z = 5 \text{ pixel}$ . In fact, in this particular set of data, the main high- $Q$  features at a given horizontal level have effectively two different contributions: one due to the change between open and closed field lines and the other features surrounding the current at the same level. The second kind of high- $Q$  features is also related to the HFT and the overlying flux rope found from analysing the geometry of the field lines. In particular there are, in our case, three high- $Q$  features of this second kind. One related with the axis of the HFT and the other two associated with the foot prints of the overlying flux rope. Further studies need to be undertaken because this case is not sufficiently general and is too complex to provide a definitive conclusion to properly understand all these features, especially those associated with

the overlying flux rope. In this extrapolation the relation between the topological features and the flare was unclear. We found various null points, but only a few coronal ones which are the ones that are less affected by the extrapolation used and magnetogram resolution and thus are the most reliable. In particular we found three null points of this kind in the pre-eruptive extrapolation, but all were situated away from the location of the main QSL features, and no coronal nulls were found in the extrapolation of the field after the event.

Our next step was to investigate a simple magnetic field that represented a flare geometry: a double bipolar potential field. We consider two different geometries of this kind involving either magnetic sources residing on the same plane below the photosphere or magnetic sources at two varied heights below the photosphere. These geometries have a skeleton composed of nulls and spines lying below the photosphere on the same plane as the sources for the first case, and lying between the two planes of the sources in the second case. Both of the geometries have separatrix surfaces passing through the photospheric plane. From Démoulin et al. (1996), it was already known that QSLs are associated with the intersection of the separatrix surfaces with the photosphere. As the four sources are placed further and further below the photosphere, the QSLs cover less and less of the intersection between the separatrices and the photospheric plane. Considering also a more general magnetic field determined from a numerous random source distribution, we were able to determine a more complete relation between the topology and the quasi-topology for a potential case. We presented this relation in Restante et al. (2009) and we can summarise the results here:

- the maxima of the  $Q$ -factor in the photosphere are located near and above the position of the subphotospheric null points;
- the shape of the maximum values of the  $Q$ -factor tend to follow the spine shape (as first noted by Titov et al., 2002), but not all of it;
- the non-spine related QSL footprints (i.e. *branches*) match with the curves defined by the photospheric endpoints of all fan field lines that start from subphotospheric sources and their conjugate footprints are rooted in the related null-halo.

It is accepted now that flare-like phenomena are the result of reconnection of topologically complex magnetic fields. Observations show that such fields are often characterised by a twisted structure. This is what leads to our third project: investigating 3D MHD simulations of an emerging twisted flux tube. There are two general types of flux emergence simulations: without and with overlying magnetic field. We consider one of each kind. In the first model, the flux rope starts to emerge into the solar atmosphere via a mechanism first described by Titov and Démoulin

(1999) and involving a double-J shaped current feature in the photosphere as explained by Archontis et al. (2009). Later on the central part of the flux rope also started to emerge and is associated with the transformation of the double-J current feature to an S-shape. In this second phase, the current also begins to fragment and becomes more complicated. We concentrate our investigation on this later phase of the evolution. We described the geometry of the field lines and we compare various horizontal cuts in different snapshots of the current with the QSL footprints. Again there are similarities between them, but the correspondence is not one to one. In the second case involving overlying magnetic field, we conducted similar studies, but also investigated also vertical cuts during the evolution of the flux rope emergence. We correlate the geometry of the field lines with the vertical cut of the  $Q$ -factor, the current and the  $\int E_{\parallel} dl$ . When the current and the  $\int E_{\parallel} dl$  are compared with the  $Q$ -factor we see features in one of these plots that do not have any correspondence in the other and vice versa. The high- $Q$  regions that coincide with the topological features (e.g. separators) are those that also coincide with the high  $\int E_{\parallel} dl$  and current regions. The high- $Q$  regions that are not associated with topological features can be explained by geometrical changes of the field. Furthermore, when the current and the  $\int E_{\parallel} dl$  have features residing within open magnetic field regions, the QSLs are plotted with the defined lowest value ( $Q = 2$ ), and thus they do not have any correspondence high- $Q$  feature.

Summarising our studies for the correlation between the current and the QSL footprints, we have, at first glance, a match, but when we look carefully there is not a one to one match. This is predictable since they are given by slightly different quantities. The  $Q$ -factor is given by the contribution of the magnetic field and the footprints of the field lines on the chosen level, while the current is given by a contribution of the velocity and the magnetic field. Moreover the change in time of QSLs is instantaneous since it is given only by the geometry of the field lines, while the current needs time to develop.

## 5.1 Future work

This study could be extended by investigating the evolution of 3D MHD flux emergence simulations in more detail, in particular studying more time frames to have a complete view of the magnetic evolution in order to properly understand the creation and importance of the QSLs and topological features. Also, it is important to consider further MHD simulations of flux emergence to have a more general view so that the key generic features and behaviour can be identified. It would also be nice to extend our vertical cut investigation to the case without overlying magnetic field to see if we find similar features. Furthermore, it would be useful to determine the full evolution of  $Q$ , topological features, current and  $\int E_{\parallel}$  in both types of flux

emergence experiments: with and without overlying magnetic field. In particular, it is important to identify which features are the general ones occurring in both of these simulations and to determine their relation with any likely ejecta.

This analysis could also be extended in the magnetic field extrapolation study, making vertical cuts along the HFTs observed; either in the December 2006 event or in other cases. We could also consider more dynamic MHD models of other events, such as simulations of magnetic carpet evolution, prominences or active regions, etc, to better understand what drives these events and to establish which topological and geometrical features play a key role in these phenomena.

# Bibliography

- Alfvén H. (1943)**, “On the Effect of a Vertical Magnetic Field in a Conducting Atmosphere”, *Arkiv for Astronomi*, vol. 29, pp. 1.
- alienworlds.glam.ac.uk (2010), “Animated explanation of the chromosphere (and transition region)”, URL <http://alienworlds.glam.ac.uk/sunStructure.html>.
- Aly J.J. (1990)**, “Do current sheets necessarily form in 3D sheared magnetic force-free fields?”, *Publ. Debrecen Heliophys. Obs.*, vol. 7, pp. 176.
- Aly J.J. and Amari T. (1997)**, “Current sheets in two-dimensional potential magnetic fields. III. Formation in complex topology configurations and application to coronal heating.”, *Astron. Astrophys.p*, vol. 319, pp. 699.
- Amari T., Aly J.J., Luciani J.F., Boulmezaoud T.Z. and Mikic Z. (1997)**, “Reconstructing the Solar Coronal Magnetic Field as a Force-Free Magnetic Field”, *Solar Phys.*, vol. 174, pp. 129.
- Amari T., Boulmezaoud T.Z. and Aly J.J. (2006)**, “Well posed reconstruction of the solar coronal magnetic field”, *Astron. Astrophys.p*, vol. 446, pp. 691.
- Amari T., Boulmezaoud T.Z. and Mikic Z. (1999)**, “An iterative method for the reconstructionbreak of the solar coronal magnetic field. I. Method for regular solutions”, *Astron. Astrophys.p*, vol. 350, pp. 1051.
- Amari T., Luciani J.F., Aly J.J., Mikic Z. and Linker J. (2003a)**, “Coronal Mass Ejection: Initiation, Magnetic Helicity, and Flux Ropes. I. Boundary Motion-driven Evolution”, *Astrophys. J.*, vol. 585, pp. 1073.
- Amari T., Luciani J.F., Aly J.J., Mikic Z. and Linker J. (2003b)**, “Coronal Mass Ejection: Initiation, Magnetic Helicity, and Flux Ropes. II. Turbulent Diffusion-driven Evolution”, *Astrophys. J.*, vol. 595, pp. 1231.
- Antiochos S.K. (1998)**, “The Magnetic Topology of Solar Eruptions”, *Astrophys. J. letts.*, vol. 502, pp. L181+.
- Archontis V., Hood A.W., Savcheva A., Golub L. and Deluca E. (2009)**, “On the Structure and Evolution of Complexity in Sigmoids: A Flux Emergence Model”, *Astrophys. J.*, vol. 691, pp. 1276.
- Archontis V., Moreno-Insertis F., Galsgaard K. and Hood A. (2004a)**, “3D MHD Simulations on Magnetic Flux Emergence”, vol. 575, pp. 342.

- Archontis V., Moreno-Insertis F., Galsgaard K., Hood A. and O'Shea E. (2004b)**, "Emergence of magnetic flux from the convection zone into the corona", *Astron. Astrophys.*, vol. 426, pp. 1047.
- Archontis V., Moreno-Insertis F., Galsgaard K. and Hood A.W. (2005)**, "The Three-dimensional Interaction between Emerging Magnetic Flux and a Large-Scale Coronal Field: Reconnection, Current Sheets, and Jets", *Astrophys. J.*, vol. 635, pp. 1299.
- Archontis V. and Török T. (2008)**, "Eruption of magnetic flux ropes during flux emergence", *Astron. Astrophys.p.*, vol. 492, pp. L35.
- Aschwanden M. (2004)**, *Physics of the Solar Corona*, Berlin, Germany; New York, U.S.A.: Springer.
- Asimov I. (1977)**, *The collapsing universe*, London: Hutchinson.
- Aulanier G., DeLuca E.E., Antiochos S.K., McMullen R.A. and Golub L. (2000)**, "The Topology and Evolution of the Bastille Day Flare", *Astrophys. J.*, vol. 540, pp. 1126.
- Aulanier G., Démoulin P., Schmieder B., Fang C. and Tang Y.H. (1998)**, "Magnetohydrostatic Model of a Bald-Patch Flare", *Solar Phys.*, vol. 183, pp. 369.
- Aulanier G., Pariat E. and Démoulin P. (2005)**, "Current sheet formation in quasi-separatrix layers and hyperbolic flux tubes", *Astron. Astrophys.*, vol. 444, pp. 961.
- Aulanier G., Pariat E., Démoulin P. and Devore C.R. (2006)**, "Slip-Running Reconnection in Quasi-Separatrix Layers", *Solar Phys.*, vol. 238, pp. 347.
- Aulanier G., Török T., Démoulin P. and DeLuca E.E. (2010)**, "Formation of Torus-Unstable Flux Ropes and Electric Currents in Erupting Sigmoids", *Astrophys. J.*, vol. 708, pp. 314.
- Bagalá L.G., Mandrini C.H., Rovira M.G. and Démoulin P. (2000)**, "Magnetic reconnection: a common origin for flares and AR interconnecting arcs", *Astron. Astrophys.*, vol. 363, pp. 779.
- Barnes G., Longcope D.W. and Leka K.D. (2005)**, "Implementing a Magnetic Charge Topology Model for Solar Active Regions", *Astrophys. J.*, vol. 629, pp. 561.
- Beveridge C., Priest E.R. and Brown D.S. (2002)**, "Magnetic topologies due to two bipolar regions", *Solar Phys.*, vol. 209, pp. 333.
- Biskamp D. (1986)**, "Magnetic reconnection via current sheets", *Phys. Fluids*, vol. 29, pp. 1520.
- Bobra M.G., van Ballegooijen A.A. and DeLuca E.E. (2008)**, "Modeling Non-potential Magnetic Fields in Solar Active Regions", *Astrophys. J.*, vol. 672, pp. 1209.
- Braginskii S.I. (1965)**, "Transport Processes in a Plasma", *Reviews of Plasma Physics*, vol. 1, pp. 205.

- Brown D.S. and Priest E.R. (2001)**, “The topological behaviour of 3D null points in the Sun’s corona”, *Astron. Astrophys.*, vol. 367, pp. 339.
- Büchner J. (2006)**, “Locating Current Sheets in the Solar Corona”, *βr*, vol. 122, pp. 149.
- Bungey T., Titov V. and Priest E. (1996)**, “Basic topological elements of coronal magnetic fields”, *Astron. Astrophys.*, vol. 308, pp. 233.
- Carcedo L., Brown D.S., Hood A.W., Neukirch T. and Wiegmann T. (2003)**, “A Quantitative Method to Optimise Magnetic Field Line Fitting of Observed Coronal Loops”, *Solar Phys.*, vol. 218, pp. 29.
- Chapman S. and Zirin H. (1957)**, “Notes on the solar corona and the terrestrial ionosphere”, *Smithsonian Contribution to Astrophysics*, vol. 2.
- Close R.M., Parnell C.E. and Priest E.R. (2004)**, “Separators in 3D Quiet-Sun Magnetic Fields”, *Solar Phys.*, vol. 225, pp. 21.
- Close R.M., Parnell C.E. and Priest E.R. (2005)**, “Domain structures in complex 3D magnetic fields”, *Geophys. Astrophys. Fluid Dyn.*, vol. 99, pp. 513.
- Cowley S.W.H. (1973)**, “A qualitative study of the reconnection between the Earth’s magnetic field and an interplanetary field of arbitrary orientation”, *Radio Science*, vol. 8, pp. 903.
- Craig I.J.D. and Henton S.M. (1995)**, “Exact solutions for steady state incompressible magnetic reconnection”, *Astrophys. J.*, vol. 450, p. 280.
- Cranmer S.R. (2002)**, “Coronal holes and the high-speed solar wind”, *Space Science Reviews*, vol. 101, pp. 229.
- Démoulin P. (2007)**, “Where will efficient energy release occur in 3-D magnetic configurations?”, *Advances in Space Research*, vol. 39, pp. 1367.
- Démoulin P., Bagala L.G., Mandrini C.H., Henoux J.C. and Rovira M.G. (1997)**, “Quasi-separatrix layers in solar flares. II. Observed magnetic configurations.”, *Astron. Astrophys.*, vol. 325, pp. 305.
- Démoulin P., Cuperman S. and Semel M. (1992a)**, “Determination of force-free magnetic fields above the photosphere using three-component boundary conditions. II - Analysis and minimization of scale-related growing modes and of computational induced singularities”, *Astron. Astrophys.p*, vol. 263, pp. 351.
- Démoulin P., Henoux J., Priest E. and Mandrini C. (1996)**, “Quasi-separatrix layers in solar flares. I. method”, *Astron. Astrophys.*, vol. 308, pp. 643.
- Démoulin P., Henoux J.C. and Mandrini C.H. (1992b)**, “Development of a topological model for solar flares”, *Solar Phys.*, vol. 139, pp. 105.
- Démoulin P., Henoux J.C. and Mandrini C.H. (1994a)**, “Are magnetic null points important in solar flares ?”, *Astron. Astrophys.*, vol. 285, pp. 1023.
- Démoulin P., Mandrini C.H., Rovira M.G., Henoux J.C. and Machado M.E. (1994b)**, “Interpretation of multiwavelength observations of November 5, 1980 solar flares by the magnetic topology of AR 2766”, *Solar Phys.*, vol. 150, pp. 221.

- Démoulin P., Priest E.R. and Lonie D.P. (1996)**, “Three-dimensional magnetic reconnection without null points 2. Application to twisted flux tubes”, *J. Geophys. Res.*, vol. 101, pp. 7631.
- DeRosa M.L., Schrijver C.J., Barnes G., Leka K.D., Lites B.W., Aschwanden M.J., Amari T., Canou A., McTiernan J.M., Régnier S., Thalmann J.K., Valori G., Wheatland M.S., Wiegmann T., Cheung M.C.M., Conlon P.A., Fuhrmann M., Inhester B. and Tadesse T. (2009)**, “A Critical Assessment of Nonlinear Force-Free Field Modeling of the Solar Corona for Active Region 10953”, *Astrophys. J.*, vol. 696, pp. 1780.
- Des Jardins A., Canfield R., Longcope D., Fordyce C. and Waitukaitis S. (2009)**, “Reconnection in Three Dimensions: The Role of Spines in Three Eruptive Flares”, *Solar Phys.*.
- DeVore C.R. and Antiochos S.K. (2000)**, “Formation and Stability of Helical Prominence Magnetic Fields”, in “Bulletin of the American Astronomical Society”, vol. 32 of *Bulletin of the American Astronomical Society*, pp. 846–+.
- Dhillon V. (2009)**, URL <http://www.vikdhillon.staff.shef.ac.uk>.
- Fan Y. (2001)**, “The Emergence of a Twisted  $\Omega$ -Tube into the Solar Atmosphere”, *Astrophys. J. letts.*, vol. 554, pp. L111.
- Fan Y. and Gibson S.E. (2004)**, “Numerical Simulations of Three-dimensional Coronal Magnetic Fields Resulting from the Emergence of Twisted Magnetic Flux Tubes”, *Astrophys. J.*, vol. 609, pp. 1123.
- Fletcher L. and Hudson H.S. (2002)**, “Spectral and Spatial Variations of Flare Hard X-ray Footpoints”, *Solar Phys.*, vol. 210, pp. 307.
- Forbes T.G. (2000)**, “A review on the genesis of coronal mass ejections”, *J. Geophys. Res.*, vol. 105, pp. 23153.
- Fukao S., Ugai M. and Tsuda T. (1975)**, “Topological study of magnetic field near a neutral point”, *Report Ionosphere Space Research Japan*, vol. 29, pp. 133.
- Galsgaard K., Archontis V., Moreno-Insertis F. and Hood A.W. (2007)**, “The Effect of the Relative Orientation between the Coronal Field and New Emerging Flux. I. Global Properties”, *Astrophys. J.*, vol. 666, pp. 516.
- Galsgaard K., Moreno-Insertis F., Archontis V. and Hood A. (2005)**, “A Three-dimensional Study of Reconnection, Current Sheets, and Jets Resulting from Magnetic Flux Emergence in the Sun”, *Astrophys. J. letts.*, vol. 618, pp. L153.
- Galsgaard K. and Nordlund Å. (1997)**, “Heating and activity of the solar corona. 3. Dynamics of a low beta plasma with three-dimensional null points”, *J. Geophys. Res.*, vol. 102, pp. 231.
- Galsgaard K., Priest E.R. and Nordlund Å. (2000)**, “Three-dimensional Separator Reconnection - How Does It Occur?”, *Solar Phys.*, vol. 193, pp. 1.
- Galsgaard K., Titov V.S. and Neukirch T. (2003)**, “Magnetic Pinching of Hyperbolic Flux Tubes. II. Dynamic Numerical Model”, *Astrophys. J.*, vol. 595, pp. 506.

- Gary G.A. (1989)**, “Linear force-free magnetic fields for solar extrapolation and interpretation”, *Astrophys. J. Suppl.*, vol. 69, pp. 323.
- Giacconi R. (1922)**, “G.s. vaiana memorial lecture”, pp. 3–19.
- Gold T. and Hoyle F. (1960)**, “On the origin of solar flares”, *mnras*, vol. 120, pp. 89.
- Gorbachev V.S. and Somov B.V. (1988)**, “Photospheric vortex flows as a cause for two-ribbon flares - A topological model”, *Solar Phys.*, vol. 117, pp. 77.
- Gorbachev V.S. and Somov B.V. (1989)**, “Solar Flares of 1980NOV5 as the Result of Magnetic Reconnection at a Separator”, *Soviet Astronomy*, vol. 33, pp. 57.
- Greene J. (1988)**, “Geometrical properties of three-dimensional reconnecting magnetic fields with nulls”, *J. Geophys. Res.*, vol. 93(A8), pp. 8583.
- Hagenaar H.J. (2001)**, “Ephemeral Regions on a Sequence of Full-Disk Michelson Doppler Imager Magnetograms”, *Astrophys. J.*, vol. 555, pp. 448.
- Hagyard M.J. (1988)**, “Observed nonpotential magnetic fields and the inferred flow of electric currents at a location of repeated flaring”, *Solar Phys.*, vol. 115, pp. 107.
- Hale G.E. (1908)**, “On the Probable Existence of a Magnetic Field in Sun-Spots”, *Astrophys. J.*, vol. 28, pp. 315.
- Hale G.E. (1922)**, “Invisible sun-spots”, *Mon. Not. Roy. Astron.Soc.*, vol. 82, pp. 168.
- Hannakam L., Gary G.A. and Teuber D.L. (1984)**, “Computation of solar magnetic fields from photospheric observations”, *Solar Phys.*, vol. 94, pp. 219.
- Hart A.B. (1954)**, “Motions in the Sun at the photospheric level. IV. The equatorial rotation and possible velocity fields in the photosphere”, *Mon. Not. Roy. Astron.Soc.*, vol. 114, pp. 17.
- Hart A.B. (1956)**, “Motions in the Sun at the photospheric level. VI. Large-scale motions in the equatorial region”, *Mon. Not. Roy. Astron.Soc.*, vol. 116, pp. 38.
- Haynes A.L., Parnell C.E., Galsgaard K. and Priest E.R. (2007)**, “Magnetohydrodynamic evolution of magnetic skeletons”, *Royal Society of London Proceedings Series A*, vol. 463, pp. 1097.
- Herschel W. (1801)**, “Observations Tending to Investigate the Nature of the Sun, in Order to Find the Causes or Symptoms of Its Variable Emission of Light and Heat; With Remarks on the Use That May Possibly be Drawn from Solar Observations”, *Royal Society of London Philosophical Transactions Series I*, vol. 91, pp. 265.
- Hesse M. (1988)**, “Untersuchungen zur magnetischen rekonnexion in dreidimensionalen systemen”, *Dr. rer. nat. Dissertation*.
- Hesse M. (1995)**, “Three-Dimensional Magnetic Reconnection in Space- and Astrophysical Plasmas and its Consequences for Particle Acceleration.”, in G. Klare, ed., “Reviews in Modern Astronomy”, vol. 8 of *Reviews in Modern Astronomy*, pp. 323–348.
- Hesse M. and Birn J. (1993)**, “Three-dimensional magnetotail equilibria by numerical relaxation techniques”, *J. Geophys. Res.*, vol. 98, pp. 3973.

- Hesse M. and Schindler K. (1988)**, “A theoretical foundation of general magnetic reconnection”, *J. Geophys. Res.*, vol. 93, pp. 5559.
- Hofmann A. and Kalman B. (1991)**, “Electric currents and free energy in a flaring twisted field configuration (NOAA 4263)”, *Astron. Astrophys.p*, vol. 241, pp. 203.
- Hornig G. (2003)**, “Chaos and Order in Three-Dimensional Magnetic Reconnection”, *Astronomische Nachrichten Supplement*, vol. 324, pp. 70.
- Inhester B. and Wiegmann T. (2006)**, “Nonlinear Force-Free Magnetic Field Extrapolations: Comparison of the Grad Rubin and Wheatland Sturrock Roumeliotis Algorithm”, *Solar Phys.*, vol. 235, pp. 201.
- Isobe H., Miyagosh T., Shibata K., Yokoyama T. and Matsumoto R. (2007)**, “Magnetohydrodynamic Simulation of Emerging Flux Region of the Sun”, *Journal of the Earth Simulator*, vol. 7(3-8).
- Isobe H., Miyagoshi T., Shibata K. and Yokoyama T. (2005)**, “Filamentary structure on the Sun from the magnetic Rayleigh-Taylor instability”, *Nature*, vol. 434, pp. 478.
- Keller C.U., Schüssler M., Vögler A. and Zakharov V. (2004)**, “On the origin of solar faculae”, *Astrophys. J. letts.*, vol. 607, pp. L59.
- Kennewell J. and McDonald A. (2010)**, “The solar photosphere”, URL <http://www.ips.gov.au>.
- Khan J.I., Hudson H.S. and Mouradian Z. (2004)**, “Soft X-ray analysis of a loop flare on the Sun”, *Astron. Astrophys.p*, vol. 416, pp. 323.
- Krall J., Chen J., Santoro R., Spicer D.S., Zalesak S.T. and Cargill P.J. (1998)**, “Simulation of Buoyant Flux Ropes in a Magnetized Solar Atmosphere”, *Astrophys. J.*, vol. 500, pp. 992.
- Kress R. (1989)**, *Methoden und Verfahren der Mathematischen Physik, Problems of Applied Analysis*, New York: P. Lang.
- Kueveler G. (1983)**, “Velocity fields of individual supergranules”, *Solar Phys.*, vol. 88, pp. 13.
- Lakhina G.S. (2000)**, “Magnetic reconnection”, *Bulletin of the Astronomical Society of India*, vol. 28, pp. 593.
- Lau Y.T. and Finn J. (1990)**, “Three-dimensional kinematic reconnection in the presence of field nulls and closed field lines”, *Astrophys. J.*, vol. 350, pp. 672.
- Lau Y.T. and Finn J.M. (1993)**, “Fast dynamos with finite resistivity in steady flows with stagnation points”, *Physics of Fluids B*, vol. 5, pp. 365.
- Leka K.D., Fan Y. and Barnes G. (2005)**, “On the Availability of Sufficient Twist in Solar Active Regions to Trigger the Kink Instability”, *Astrophys. J.*, vol. 626, pp. 1091.
- Leka K.D. and Skumanich A. (1999)**, “On the value of ‘ $\alpha$ AR’ from vector magnetograph data - I. Methods and Caveats”, *Solar Phys.*, vol. 188, pp. 3.
- Longcope D. (2001)**, “Separator current sheets: Generic features in minimum-energy magnetic fields subject to flux constraints”, *Phys. Plasmas*, vol. 8, pp. 5277.

- Longcope D. and Klapper I. (2002)**, “A general theory of connectivity and current sheets in coronal magnetic fields”, *Astrophys. J.*, vol. 579, pp. 468.
- Longcope D.W. (1996)**, “Topology and Current Ribbons: A Model for Current, Reconnection and Flaring in a Complex, Evolving Corona”, *Solar Phys.*, vol. 169, pp. 91.
- Longcope D.W. (2004)**, *MPOLE 2.4*, URL [http://solar.physics.montana.edu/dana/mpole/mpole\\_doc.html](http://solar.physics.montana.edu/dana/mpole/mpole_doc.html).
- Longcope D.W. and Beveridge C. (2007)**, “A Quantitative, Topological Model of Reconnection and Flux Rope Formation in a Two-Ribbon Flare”, *Astrophys. J.*, vol. 669, pp. 621.
- Longcope D.W., Beveridge C., Qiu J., Ravindra B., Barnes G. and Dasso S. (2007)**, “Modeling and Measuring the Flux Reconnected and Ejected by the Two-Ribbon Flare/CME Event on 7 November 2004”, *Solar Phys.*, vol. 244, pp. 45.
- Longcope D.W. and Cowley S.C. (1996)**, “Current sheet formation along three-dimensional magnetic separators”, *Phys. Plasmas*, vol. 3, pp. 2885.
- Longcope D.W., McKenzie D.E., Cirtain J. and Scott J. (2005)**, “Observations of Separator Reconnection to an Emerging Active Region”, *Astrophys. J.*, vol. 630, pp. 596.
- Longcope D.W. and Parnell C.E. (2009)**, “The Number of Magnetic Null Points in the Quiet Sun Corona”, *Solar Phys.*, vol. 254, pp. 51.
- Longcope D.W. and Silva A.V.R. (1998)**, “A current ribbon model for energy storage and release with application to the flare of 7 January 1992”, *Solar Phys.*, vol. 179, pp. 349.
- Low B. and Wolfson R. (1988)**, “Spontaneous formation of electric current sheets and the origin of solar flares”, *Astrophys. J.*, vol. 324, pp. 574.
- Low B.C. (1996)**, “Solar Activity and the Corona”, *Solar Phys.*, vol. 167, pp. 217.
- Maclean R., Buchner J. and Priest E.R. (2008)**, “Relationship between the topological skeleton, current concentrations, and 3D magnetic reconnection sites in the solar atmosphere.”, *Astron. Astrophys.*
- Magara T. (2001)**, “Dynamics of Emerging Flux Tubes in the Sun”, *Astrophys. J.*, vol. 549, pp. 608.
- Magara T. and Longcope D.W. (2001)**, “Sigmoid Structure of an Emerging Flux Tube”, *Astrophys. J. letts.*, vol. 559, pp. L55.
- Magara T. and Longcope D.W. (2003)**, “Injection of Magnetic Energy and Magnetic Helicity into the Solar Atmosphere by an Emerging Magnetic Flux Tube”, *Astrophys. J.*, vol. 586, pp. 630.
- Manchester I.W., Gombosi T., DeZeeuw D. and Fan Y. (2004)**, “Eruption of a Buoyantly Emerging Magnetic Flux Rope”, *Astrophys. J.*, vol. 610, pp. 588.
- Mandrini C.H., Demoulin P., Schmieder B., Deluca E.E., Pariat E. and Uddin W. (2006)**, “Companion Event and Precursor of the X17 Flare on 28 October 2003”, *Solar Phys.*, vol. 238, pp. 293.

- Mandrini C.H., Démoulin P., van Driel-Gesztelyi L., Schmieder B., Cauzzi G. and Hofmann A. (1996)**, “3D Magnetic Reconnection at an X-Ray Bright Point”, *Solar Phys.*, vol. 168, pp. 115.
- Mariska J.T. (1986)**, “The quiet solar transition region”, *Ann. Rev. Astron. Astrophys.*, vol. 24, pp. 23.
- Masson S., Pariat E., Aulanier G. and Schrijver C.J. (2009)**, “The Nature of Flare Ribbons in Coronal Null-Point Topology”, *Astrophys. J.*, vol. 700, pp. 559.
- Matsumoto R. and Shibata K. (1992)**, “Three-dimensional MHD simulation of the Parker instability in galactic gas disks and the solar atmosphere”, *Publ. Astron. Soc. Japan*, vol. 44, pp. 167.
- Matsumoto R., Tajima T., Chou W., Okubo A. and Shibata K. (1998)**, “Formation of a Kinked Alignment of Solar Active Regions”, *Astrophys. J. Letts.*, vol. 493, pp. L43+.
- McClymont A.N., Jiao L. and Mikic Z. (1997)**, “Problems and Progress in Computing Three-Dimensional Coronal Active Region Magnetic Fields from Boundary Data”, *Solar Phys.*, vol. 174, pp. 191.
- McClymont A.N. and Mikic Z. (1994)**, “Thickness variations along coronal loops inferred from vector magnetograph data”, *Astrophys. J.*, vol. 422, pp. 899.
- Mikic Z. (1997)**, “Determination of Coronal Magnetic Fields from Vector Magnetograms”, Tech. rep.
- Molodenskii M.M. and Syrovatskii S.I. (1977)**, “Magnetic fields of active regions and their zero points”, *Soviet Astronomy*, vol. 21, pp. 734.
- Moreno-Insertis F. and Emonet T. (1996)**, “The Rise of Twisted Magnetic Tubes in a Stratified Medium”, *Astrophys. J. Letts.*, vol. 472, pp. L53+.
- Murray M.J., Hood A.W., Moreno-Insertis F., Galsgaard K. and Archontis V. (2006)**, “3D simulations identifying the effects of varying the twist and field strength of an emerging flux tube”, *Astron. Astrophys.*, vol. 460, pp. 909.
- Pariat E., Antiochos S.K. and DeVore C.R. (2009)**, “A Model for Solar Polar Jets”, *Astrophys. J.*, vol. 691, pp. 61.
- Parker E.N. (1957)**, “Sweet’s Mechanism for Merging Magnetic Fields in Conducting Fluids”, *J. Geophys. Res.*, vol. 62, pp. 509.
- Parker E.N. (1958)**, “Dynamics of the interplanetary gas and magnetic fields.”, *Astrophys. J.*, vol. 128, pp. 664.
- Parker E.N. (1979)**, “Sunspots and the physics of magnetic flux tubes. I - The general nature of the sunspot. II - Aerodynamic drag”, *Astrophys. J.*, vol. 230, pp. 905.
- Parnell C., Smith J., Neukirch T. and Priest E. (1996)**, “The structure of three-dimensional magnetic neutral points”, *Phys. Plasmas*, vol. 3, pp. 759.
- Parnell C.E. (2007)**, “Multiply Connected Source and Null Pairs”, *Solar Phys.*, vol. 242, pp. 21.
- Parnell C.E., Haynes A.L. and Galsgaard K. (2008)**, “Recursive Reconnection and Magnetic Skeletons”, *Astrophys. J.*, vol. 675, pp. 1656.

- Parnell C.E., Haynes A.L. and Galsgaard K. (2010)**, “Structure of magnetic separators and separator reconnection”, *Journal of Geophysical Research (Space Physics)*, vol. 115, pp. 2102.
- Parnell C.E., Priest E.R. and Golub L. (1994)**, “The three-dimensional structures of X-ray bright points”, *Solar Phys.*, vol. 151, pp. 57.
- Petschek H.E. (1964)**, “Magnetic Field Annihilation”, *NASA Special Publication*, vol. 50, pp. 425.
- Pontin D.I. and Galsgaard K. (2007)**, “Current amplification and magnetic reconnection at a three-dimensional null point: Physical characteristics”, *Journal of Geophysical Research (Space Physics)*, vol. 112, pp. 3103.
- Pontin D.I., Hornig G. and Priest E.R. (2004)**, “Kinematic Magnetic Reconnection at 3d Null Points”, in R. W. Walsh, J. Ireland, D. Danesy, & B. Fleck, ed., “SOHO 15 Coronal Heating”, vol. 575 of *ESA Special Publication*, pp. 507–+.
- Priest E. (1982)**, *Solar Magnetohydrodynamics*, vol. 21 of *Geophysics and Astrophysics Monographs*, Dordrecht, Netherlands; Boston, U.S.A.: D. Reidel.
- Priest E. (2010)**, “Mhd reconnection”, URL <http://www.scholarpedia.org>.
- Priest E., Bungey T. and Titov V. (1997)**, “The 3d topology and interaction of complex magnetic flux systems”, *Geophys. Astrophys. Fluid Dyn.*, vol. 84, pp. 127.
- Priest E. and Démoulin P. (1995)**, “Three-dimensional magnetic reconnection without null points 1. basic theory of magnetic flipping”, *J. Geophys. Res.*, vol. 100(23), pp. 443 .
- Priest E. and Forbes T. (2000)**, *Magnetic Reconnection*, UK: Chambridge University Press.
- Priest E. and Titov V. (1996)**, “Magnetic reconnection at three-dimensional null points”, *Philos. Trans. R. Soc. London, Ser. A*, vol. 354, pp. 2951.
- Priest E.R. and Forbes T.G. (1986)**, “New models for fast steady state magnetic reconnection”, *J. Geophys. Res.*, vol. 91, pp. 5579.
- Priest E.R., Heyvaerts J.F. and Title A.M. (2002)**, “A Flux-Tube Tectonics Model for Solar Coronal Heating Driven by the Magnetic Carpet”, *Astrophys. J.*, vol. 576, pp. 533.
- Priest E.R., Longcope D.W. and Heyvaerts J. (2005a)**, “Coronal Heating at Separators and Separatrices”, *Astrophys. J.*, vol. 624, pp. 1057.
- Priest E.R., Longcope D.W. and Heyvaerts J. (2005b)**, “Coronal Heating at Separators and Separatrices”, *Astrophys. J.*, vol. 624, pp. 1057.
- Priest E.R. and Pontin D.I. (2009)**, “Three-dimensional null point reconnection regimes”, *Phys. Plasmas*, vol. 16(12), pp. 122101.
- Qui H., Zhao G., Takada-Hidai M., Chen Y., Takeda Y., Noguchi K., Sadakane K. and Aoki W. (2002)**, “ $\alpha$  Element Abundances in Mildly Metal-Poor Stars”, *Publ. Astron. Soc. Japan*, vol. 54, pp. 103.
- Régnier S. (2007)**, “Nonlinear force-free field extrapolation: numerical methods and applications”, *Memorie della Societa Astronomica Italiana*, vol. 78, pp. 126.

- Restante A.L., Aulanier G. and Parnell C.E. (2009)**, “How skeletons turn into quasi-separatrix layers in source models”, *Astron. Astrophys.p*, vol. 508, pp. 433.
- Riley P., Linker J.A., Mikić Z., Lionello R., Ledvina S.A. and Luhmann J.G. (2006)**, “A Comparison between Global Solar Magnetohydrodynamic and Potential Field Source Surface Model Results”, *Astrophys. J.*, vol. 653, pp. 1510.
- Rogers L. (2007)**, “The history of trigonometry - part 1”, URL <http://nrich.maths.org>.
- Roumeliotis G. (1996)**, “The “Stress-and-Relax” Method for Reconstructing the Coronal Magnetic Field from Vector Magnetograph Data”, *Astrophys. J.*, vol. 473, pp. 1095.
- Sakurai T. (1989)**, “Computational modeling of magnetic fields in solar active regions”, *Space Science Reviews*, vol. 51, pp. 11.
- Schmidt H. (1964)**, “On the observable effects of magnetic energy storage and release connected with solar flares”, in W. Hess, ed., “The Physics of Solar Flares”, vol. SP-50 of *NASA Special Publication*, p. 107, Washington, DC: NASA.
- Schmieder B., Aulanier G., Demoulin P., van Driel-Gesztelyi L., Roudier T., Nitta N. and Cauzzi G. (1997)**, “Magnetic reconnection driven by emergence of sheared magnetic field.”, *Astron. Astrophys.*, vol. 325, pp. 1213.
- Schrijver C. and Title A. (2002)**, “The topology of mixed-polarity potential field, and inferences for heating of the quiet solar corona”, *Solar Phys.*, vol. 207, pp. 223.
- Schrijver C.J., DeRosa M.L., Metcalf T., Barnes G., Lites B., Tarbell T., McTiernan J., Valori G., Wiegmann T., Wheatland M.S., Amari T., Aulanier G., Démoulin P., Fuhrmann M., Kusano K., Régnier S. and Thalmann J.K. (2008)**, “Nonlinear Force-free Field Modeling of a Solar Active Region around the Time of a Major Flare and Coronal Mass Ejection”, *Astrophys. J.*, vol. 675, pp. 1637.
- Schrijver C.J., DeRosa M.L., Metcalf T.R., Liu Y., McTiernan J., Régnier S., Valori G., Wheatland M.S. and Wiegmann T. (2006)**, “Nonlinear Force-Free Modeling of Coronal Magnetic Fields Part I: A Quantitative Comparison of Methods”, *Solar Phys.*, vol. 235, pp. 161.
- Schwabe M. (1843)**, “Die sonne. von herrn hofrath schwabe”, *Astronomische Nachrichten*, vol. 20, p. 283.
- Seehafer N. (1986)**, “On the magnetic field line topology in solar active regions”, *Solar Phys.*, vol. 105, pp. 223.
- Shibata K., Nozawa S. and Matsumoto R. (1992)**, “Magnetic reconnection associated with emerging magnetic flux”, *Publ. Astron. Soc. Japan*, vol. 44, pp. 265.
- Shibata K., Tajima T., Matsumoto R., Horiuchi T., Hanawa T., Rosner R. and Uchida Y. (1989a)**, “Nonlinear Parker instability of isolated magnetic flux in a plasma”, *Astrophys. J.*, vol. 338, pp. 471.

- Shibata K., Tajima T., Steinolfson R.S. and Matsumoto R. (1989b)**, “Two-dimensional magnetohydrodynamic model of emerging magnetic flux in the solar atmosphere”, *Astrophys. J.*, vol. 345, pp. 584.
- solarscience.msfc.nasa.gov (2010), “Solar physics”, URL <http://solarscience.msfc.nasa.gov/>.
- solarsystem.nasa.gov (2010), “Student handout”, URL <http://solarsystem.nasa.gov/docs>.
- Song M.T., Fang C., Tang Y.H., Wu S.T. and Zhang Y.A. (2006)**, “A New and Fast Way to Reconstruct a Nonlinear Force-free Field in the Solar Corona”, *Astrophys. J.*, vol. 649, pp. 1084.
- Sonnerup B.U.Ö. (1979)**, “Magnetic Field Reconnection”, in “Space Plasma Physics: The Study of Solar-System Plasmas”, vol. Volume 2, p. 879.
- Sonnerup B.U.O. and Priest E.R. (1975)**, “Resistive mhd stagnation-point flows at a current sheet”, *J. Plasma Phys.*, vol. 14, pp. 283.
- Spitzer L. (1962)**, *Physics of Fully Ionized Gases*, New York: Interscience (2nd edition).
- Spruit H.C. and Roberts B. (1983)**, “Magnetic flux tubes on the sun”, *Nature*, vol. 304, pp. 401.
- Sweet P.A. (1958)**, “The topology of force-free magnetic fields”, *The Observatory*, vol. 78, pp. 30.
- Titov V., Hornig G. and Démoulin P. (2002)**, “Theory of magnetic connectivity in the solar corona”, *J. Geophys. Res.*, vol. 107(A8), pp. 3.
- Titov V.S. (2007)**, “Generalized Squashing Factors for Covariant Description of Magnetic Connectivity in the Solar Corona”, *Astrophys. J.*, vol. 660, pp. 863.
- Titov V.S. and Démoulin P. (1999)**, “Basic topology of twisted magnetic configurations in solar flares”, *Astron. Astrophys.*, vol. 351, pp. 707.
- Titov V.S., Galsgaard K. and Neukirch T. (2003)**, “Magnetic Pinching of Hyperbolic Flux Tubes. I. Basic Estimations”, *Astrophys. J.*, vol. 582, pp. 1172.
- Titov V.S. and Hornig G. (2002)**, “Magnetic connectivity of coronal fields: geometrical versus topological description”, *Advances in Space Research*, vol. 29, pp. 1087.
- Titov V.S., Priest E.R. and Demoulin P. (1993)**, “Conditions for the appearance of “bald patches” at the solar surface”, *Astron. Astrophys.*, vol. 276, pp. 564.
- Toriumi S. and Yokoyama T. (2010)**, “Two-step Emergence of the Magnetic Flux Sheet from the Solar Convection Zone”, *Astrophys. J.*, vol. 714, pp. 505.
- Valori G., Kliem B. and Keppens R. (2005)**, “Extrapolation of a nonlinear force-free field containing a highly twisted magnetic loop”, *Astron. Astrophys.p*, vol. 433, pp. 335.
- Valori G., Kliem B., Török T. and Titov V.S. (2010)**, “Testing magnetofrictional extrapolation with the Titov-Démoulin model of solar active regions”, *Astron. Astrophys.p*, vol. 519, p. A44.

- van Ballegooijen A.A. (2004)**, “Observations and Modeling of a Filament on the Sun”, *Astrophys. J.*, vol. 612, pp. 519.
- van Ballegooijen A.A., Deluca E.E., Squires K. and Mackay D.H. (2007)**, “Modeling magnetic flux ropes in the solar atmosphere”, *Journal of Atmospheric and Solar-Terrestrial Physics*, vol. 69, pp. 24.
- Vekstein G., Priest E.R. and Amari T. (1991)**, “Formation of current sheets in force-free magnetic fields”, *Astron. Astrophys.*, vol. 243, pp. 492.
- Vrnak B., Bein B., Kienreich I., Muhr N. and Stoiser S. (2007)**, *Solar Physics: Flares and CMEs (lecture notes)*.
- Watson P.G. and Craig I.J.D. (1998)**, “Magnetic Annihilation and Reconnection in Two Dimensions”, *Astrophys. J.*, vol. 505, pp. 363.
- Webb D.F. (2000)**, “Coronal mass ejections: origins, evolution, and role in space weather”, *IEEE Transactions on Plasma Science*, vol. 28, pp. 1795.
- Wheatland M.S. (2004)**, “Parallel Construction of Nonlinear Force-Free Fields”, *Solar Phys.*, vol. 222, pp. 247.
- Wheatland M.S. (2006)**, “A Fast Current-Field Iteration Method for Calculating Nonlinear Force-Free Fields”, *Solar Phys.*, vol. 238, pp. 29.
- Wheatland M.S., Sturrock P.A. and Roumeliotis G. (2000)**, “An Optimization Approach to Reconstructing Force-free Fields”, *Astrophys. J.*, vol. 540, pp. 1150.
- Wiegelmann T. (2004)**, “Optimization code with weighting function for the reconstruction of coronal magnetic fields”, *Solar Phys.*, vol. 219, pp. 87.
- Wiegelmann T. and Neukirch T. (2002)**, “Including stereoscopic information in the reconstruction of coronal magnetic fields”, *Solar Phys.*, vol. 208, pp. 233.
- Wilmot-Smith A.L., Hornig G. and Pontin D.I. (2009)**, “Magnetic Braiding and Quasi-Separatrix Layers”, *Astrophys. J.*, vol. 704, pp. 1288.
- Woltjer L. (1958)**, “A Theorem on Force-Free Magnetic Fields”, *Proceedings of the National Academy of Science*, vol. 44, pp. 489.
- Wu S.T., Sun M.T., Chang H.M., Hagyard M.J. and Gary G.A. (1990)**, “On the numerical computation of nonlinear force-free magnetic fields”, *Astrophys. J.*, vol. 362, pp. 698.
- www.nasa.gov (2011)**, URL <http://www.nasa.gov/>.
- www.nasaimages.org (2004)**, “Halloween 2003 solar storms”, URL <http://www.nasaimages.org/>.
- www.oup.co.uk (2010)**, “Oxford illustrated science encyclopedia”, URL <http://www.oup.co.uk/oxed/children/oise/pictures/space/sun/>.
- Yan Y. and Li Z. (2006)**, “Direct Boundary Integral Formulation for Solar Non-constant- $\alpha$  Force-free Magnetic Fields”, *Astrophys. J.*, vol. 638, pp. 1162.
- Yan Y. and Sakurai T. (1997)**, “Analysis of it YOHKOH SXT Coronal Loops and Calculated Force-Free Magnetic Field Lines from Vector Magnetograms”, *Solar Phys.*, vol. 174, pp. 65.

- Yan Y.** and **Sakurai T.** (2000), “New Boundary Integral Equation Representation for Finite Energy Force-Free Magnetic Fields in Open Space above the Sun”, *Solar Phys.*, vol. 195, pp. 89.
- Yang W.H.**, **Sturrock P.A.** and **Antiochos S.K.** (1986), “Force-free magnetic fields - The magneto-frictional method”, *Astrophys. J.*, vol. 309, pp. 383.
- Yokoyama T.** and **Shibata K.** (1995), “Magnetic reconnection as the origin of X-ray jets and H $\alpha$  surges on the Sun”, *Nature*, vol. 375, pp. 42.
- Yokoyama T.** and **Shibata K.** (1996), “Numerical Simulation of Solar Coronal X-Ray Jets Based on the Magnetic Reconnection Model”, *Publ. Astron. Soc. Japan*, vol. 48, pp. 353.
- Zirker J.B.** (2002), *Journey from the center of the sun*, Princeton University Press.